A thesis for the partial fulfillment of the Masters of Science degree

The aqueous synthesis and characterization of bimetallic gold-copper nanoparticle catalysts for CO oxidation

Bsc. Marianne Bijl

Debye Institute for Nanomaterials Science, Utrecht University

February, 2023

This work was conducted in the Materials Chemistry and Catalysis group under the supervision of MSc. Marta Perxés i Perich, Dr. Jessi E. S. van der Hoeven and Prof. Dr. Petra E. de Jongh

ABSTRACT

Bimetallic nanoparticles have attracted significant interest in the field of heterogeneous catalysis due to their unique and tunable properties, arising from synergistic effects. Of particular interest are gold-copper nanoparticles, which demonstrate potential in catalyzing the oxidation of carbon monoxide (CO). While gold can act as an active site for CO, copper can facilitate the dissociation of oxygen, thereby enabling an efficient conversion of CO. This is important for reducing the negative impact of CO on human health and the environment.

The conventional synthesis of gold-copper nanoparticles has primarily been limited to organic synthesis due to the instability of copper towards oxidation. Nonetheless, an aqueous synthesis of gold-copper nanoparticles would offer a more sustainable, non-toxic and inexpensive alternative. Therefore, the synthesis of gold-copper nanoparticles in aqueous solvents has been investigated in this work. The synthesis was based on colloidal strategies to gain a high degree of control over the morphology. The nanoparticles were characterized with state-of-the-art electron microscopy techniques, ultraviolet-visible spectroscopy, x-ray diffraction, Fourier transform-infrared spectroscopy, thermal gravimetric analysis and inductively coupled plasma atomic emission spectroscopy.

This thesis presented three colloidal, aqueous synthesis routes to obtain gold-copper nanoparticles. The routes were based on a novel approach of growing oxidized copper on gold nanoparticles in an aqueous solution, followed by thermal reduction. The first synthesis route utilized gold nanoparticles coated with a mesoporous silica shell. Although the silica shell provided stability, it restricted the copper content (<30%) in the obtained gold-copper nanoparticles. The second synthesis route eliminated the silica shell, thereby obtaining Au@Cu_2O nanoparticles with higher copper contents up to approximately 87%. However, the nanoparticles clustered upon deposition on a silica support, leading to aggregation when subjected to thermal treatment. The synthesis third route, in which Cu_2O was grown on supported gold nanoparticles, resulted in well-dispersed gold-copper

nanoparticles, but also the formation of monometallic Cu_2O particles on the support. Although further optimization would be beneficial, the third method showed promise for synthesizing gold-copper nanoparticles in aqueous solution.

The catalytic potential of supported gold-copper nanoparticles, synthesized via the third method, was evaluated for CO oxidation. The supported bimetallic gold-copper nanoparticles exhibited higher turnover frequency values compared to their monometallic gold counterparts. Furthermore, gold-copper nanoparticles with a higher copper content were found to be more active. Additionally, core-shell $Au@Cu_xO$ nanoparticles were found to be significantly less active. Further research is necessary to obtain a more in-depth understanding of the catalytic performance of AuCu NPs in CO oxidation.

Keywords: aqueous solution, bimetallic nanoparticles, CO oxidation, colloidal synthesis, gold-copper, heterogeneous catalysis

ABBREVIATIONS

Abbreviation	**Meaning**
NP	nanoparticle
LSPR	localized surface plasmon resonance
EM	electron microscopy
BF-TEM	bright-field transmission electron microscopy
HAADF	high-angle annular dark-field
STEM	scanning transmission electron microscopy
EDX	energy-dispersive X-ray diffraction
SAED	selected area electron diffraction
XRD	X-ray diffraction
UV-VIS	ultraviolet-visible
FT-IR	Fourier transform-infrared
ICP-AES	inductively coupled plasma - atomic emission spectroscopy
TGA	thermal gravimetric analysis
MS	mass spectrometry
TOF	turnover frequency

TABLE OF CONTENTS

1 Introduction

Heterogeneous catalysts play a crucial role in industrial chemical processes by enabling acceleration of chemical conversions. Metal nanoparticles (NPs), in particular, have emerged as important heterogeneous catalysts due to their unique properties [1]. Their small size provides a high surface-to-volume ratio, which leads to a relatively high surface area available for catalytic reactions. Additionally, the limited dimensions of NPs can affect their optical and electronic properties with respect to their the bulk counterpart, making metal NPs even more useful in certain (catalytic) applications.

Particularly interesting metal NPs are those composed of gold (Au). Au was once considered to be inert due to its lack of reactivity towards many chemical reactions. However, this perception changed when Haruta demonstrated the effectiveness of Au NPs as a catalyst for CO oxidation [2]. Since Haruta's discovery in 1989, numerous studies involving the utilization of Au NPs as catalysts have been published. Nowadays, Au-based catalysts have found to be useful in selective oxidation and hydrogenation reactions, the water gas shift reaction and several other chemical reactions [3, 4].

The incorporation of a second metal to monometallic NPs can result in improvement of their catalytic properties. These NPs, referred to as bimetallic NPs, offer a promising strategy to design new catalyst materials with unique properties. The interaction between the two metals can change the electronic and geometric structures, which can lead to enhanced catalytic activity and selectivity [5]. The extent of this synergistic effect is highly influenced by the metal composition and distribution of bimetallic NPs [6].

An interesting Au-based bimetallic NP is obtained with the combination of copper (Cu). Cu is an earth-abundant and inexpensive metal, which was also found to be active as a catalyst for oxidation and hydrogenation reactions [7]. As a result, gold-copper (AuCu) bimetallic NPs have shown promising catalytic activity for oxidation reactions, such as

the oxidation of CO [8]. They have also been demonstrated to be a suitable catalyst for various hydrogenation reactions [9, 10] and electrochemical CO_2 reduction [11].

Another interesting feature of AuCu bimetallic systems is its ability to form chemically ordered structures with stoichiometry Au_3Cu, AuCu, and $AuCu_3$. The uniform surface geometry and well-defined composition of these ordered compounds are beneficial for catalysis and fundamental research. Additionally, the incorporation of relatively inexpensive Cu offers AuCu catalysts a commercial advantage over pure Au catalysts.

A straightforward method for the synthesis of AuCu NPs in high weight loadings is via a co-impregnation, in which a Cu and Au precursor are simultaneously reduced under elevated temperatures on a support [8]. Alternatively, colloidal methods are also attractive for catalyst preparation due to their versatility in property tailoring. They provide a high degree of control over the size and shape of the metal NPs [12]. In addition, colloidal synthesis allows for variation in the metal distribution by enabling the synthesis of bimetallic NPs with diverse structures, such as core-shell and alloys. This versatility enables easier optimization into the desired catalyst.

The co-reduction of Au and Cu precursors in solution is the most common colloidal method for synthesizing AuCu NPs. In literature, the colloidal synthesis of AuCu NPs is mainly limited to organic solutions due to the instability of Cu towards oxidation [13, 14, 15]. The lack of research into the aqueous synthesis of AuCu NPs is unfortunate, as it offers several advantages over organic synthesis. For instance, an aqueous synthesis would be more sustainable, non-toxic and inexpensive. Besides, less strongly binding ligands are required, making ligand removal prior to catalysis more facile.

In this thesis, three aqueous synthesis routes are demonstrated to obtain AuCu NPs via colloidal strategies. We aimed for different metal compositions with particular focus on the ordered phases that could be formed. Furthermore, the potential of AuCu NP catalysts for the oxidation of CO is investigated.

Scope of the thesis

This thesis can be divided into two research questions with several sub-questions. The main research question is based on the synthesis of AuCu NPs, while the second research question studies the potential of AuCu NPs as a catalysts:

1. How can AuCu NPs be synthesized via aqueous colloidal synthesis?
    (a) Can we control the metal composition of AuCu NPs with an aqueous synthesis method?
    (b) How does the metal distribution of the NPs change upon thermal treatment?
    (c) To what extent are the NPs stable upon thermal treatment?
2. What is the catalytic performance of AuCu NPs for CO oxidation?
    (a) What is the effect of the metal compositions of AuCu NPs on their catalytic performance
    (b) What is the effect of the metal distribution of AuCu NPs on their catalytic performance

The theoretical background required to understand the thesis is provided in chapter 2. Chapter 3 outlines the methods used to synthesize and characterize AuCu NPs. The results are discussed in chapter 4 of which a conclusion is provided in chapter 5. Finally, chapter 6 presents the outlook in which further research opportunities are discussed.

2 Theoretical background

The following chapter provides a concise overview of the relevant theoretical concepts required to understand the results presented in this thesis.

2.1 Basic principles of colloids

Colloidal NPs can be described as inorganic particles with a size range between 1 and 1000 nm that are dispersed within a liquid medium [16]. An important characteristic of colloids is their Brownian motion, which refers to a random motion caused by collision with the surrounding solvent molecules [17]. As a result, colloidal NPs tend to spread themselves homogeneously throughout the medium. The extent of this homogeneity is dependent on the interparticle interaction. The balance of attractive and repulsive interactions determines the stability of a colloidal system. The DLVO theory, developed by Derjaguin, Landau, Verwey, and Overbeek, is often used to understand the stability of colloids by analysing the energy of the system as the sum of attractive van der Waals forces and repulsive electrostatic forces [18, 19]. If the attractive forces are stronger than the repulsive forces, the colloidal NPs start to combine into larger aggregates.

Aggregation of colloidal NPs can be prevented by using ligands for stability. Ligands are molecules that can adsorb on the surface of the NPs, thereby altering the interparticle interactions. Polymers are commonly used as ligands because of their large chains to provide sterically hindrance [20]. When two NPs approach each other, the polymer chains will overlap each other. As a result, strong repulsion steric forces arise that counterbalance the attractive forces, preventing the NPs from coming closer (figure 2.1). Another form of stabilization is through electrostatic (coulombic) repulsion, which can be provided with ionic compounds [21]. In addition to ligands, the stability of colloids can also be influenced by the presence of electrolytes, pH, and temperature.

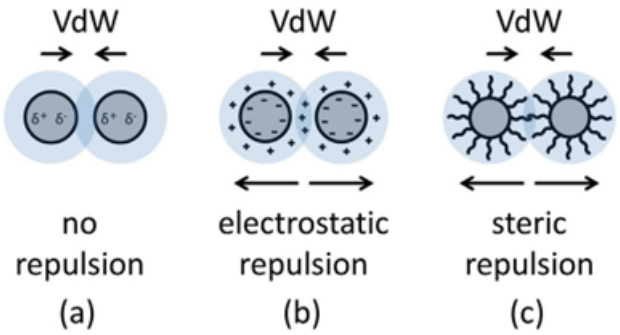

Figure 2.1: Simplified schematic illustration on how colloidal stability can be achieved by b) electrostatic repulsion or c) steric repulsion to balance the attractive van der Waals forces. Reprinted from [22].

2.2 Colloidal synthesis of Au NPs

A common technique for synthesizing colloidal Au NPs involves the reduction of Au precursor, $HAuCl_4$, with citrate in water. This method was pioneered by Turkevich in 1951 and later adapted by Frens to adjust the particle size by the amount of reducing agent/stabilizing agent, sodium citrate [23, 24]. Further modifications to the Turkevich-Frens method have been made over time. A particular important one is the separation of the nucleation and growth stage, leading to high level of structural control (figure 2.2). During the nucleation stage, small clusters of atoms, known as nuclei, are formed. Once the nuclei reach a critical size, where the rate of growth equals the rate of dissolution, they enter the growth stage where they continue to grow into a colloidal NP [25].

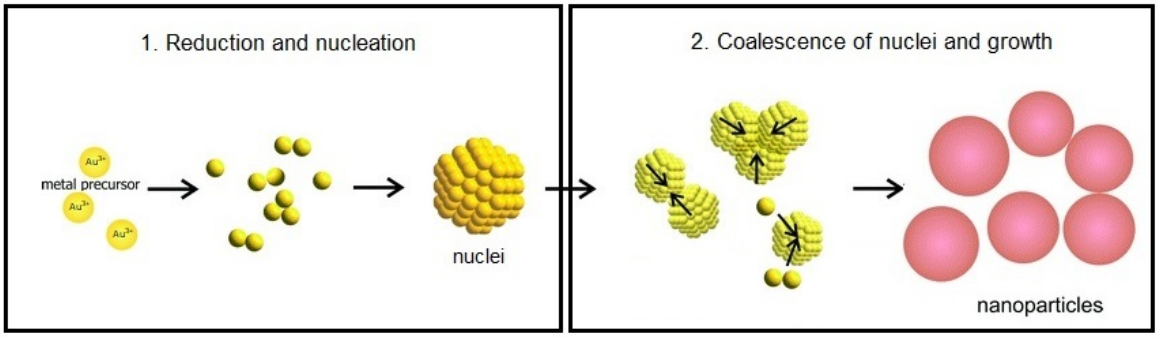

Figure 2.2: Simplified schematic illustration of the nucleation and growth stage in the colloidal synthesis of Au NPs. Modified from [26, 27].

A strategy for separating the nucleation and growth stage is through utilization of two reducing agents. The approach is used in a protocol for synthesizing monodisperse Au NPs, reported by Piella et al. [28]. It is based on the Turkevich-Frens method and involves

the reduction of tetrachloroauric acid ($HAuCl_4$) with tannic acid (TA) and sodium citrate (SC). The nucleation is promoted by the stronger reducer agent TA. Once TA is consumed, the nucleation stage is ended and the growth stage is promoted by SC. The reducing power of SC is too weak to promote homogeneous nucleation, but can induce growth on existing nuclei. Hence, the nucleation of small Au NPs (seeds) is separated from the growth solution. This so-called seed-mediated growth leads to the formation of monodisperse, spherical Au NPs with tunable particle size. In addition, the weak interaction between the Au surface and the citrate molecules results in a relatively accessible surface.

2.3 Mesoporous silica shell growth

Stability is one of the main criteria for metal NPs to be a well-designed catalyst. Metal NPs, despite being surrounded with stabilizing ligands, tend to become unstable at elevated temperatures. A surface coating is considered to be an effective way of providing thermal stability [29]. The coating is preferred to be porous, as this allows access to the metal surface, which is crucial for catalysis. It has been demonstrated that a mesoporous silica shell around Au NPs can effectively inhibit their aggregation, while remaining active as a catalyst [30, 31].

Mesoporous silica is typically synthesized by the sol-gel process in the presence of a templating surfactant. This process involves the hydrolysis and condensation of a silicate precursor (figure 2.3). The most common precursor is tetraethylorthosilicate (TEOS). The ethoxy groups of TEOS are converted to hydroxyl groups upon contact with water. This initiates the condensation process where Si−O−Si linkages are made to form silica oligomers. The hydrolysis and condensation rate are both dependent on the pH of the solution. The hydrolysis occurs through a bimolecular nucleophilic substitution reaction (Sn2 mechanism), which can be catalysed by a base or acid. At pH values above 7, silicates are easily deprotonated and silica is highly soluble, providing more species for growth.

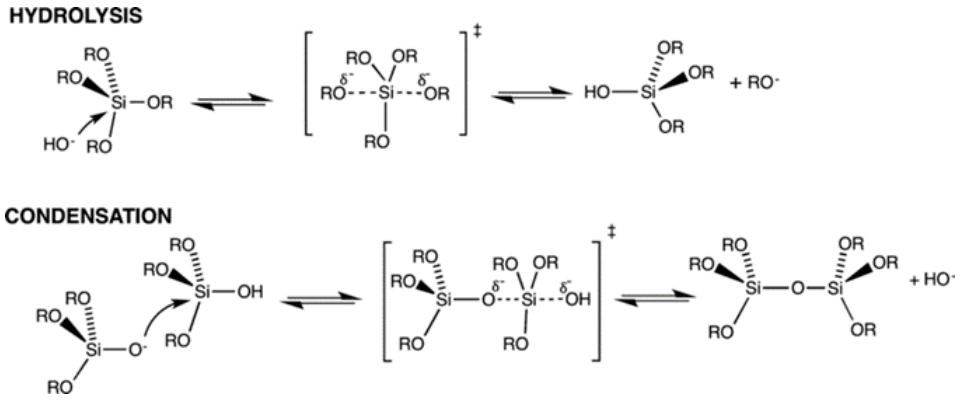

Figure 2.3: Base-catalysed hydrolysis and condensation of silica precursors. The R-group for the most common precursor, TEOS, is an ethyl group ($-C_2H_5$). Reprinted from [32].

Porosity in silica can be generated by surfactants, serving as structure-directing agents. These surfactants can self-assemble into micelles to form a framework for silica to grow in an ordered mesoporous manner. The pore size and structure of the silica is, therefore, determined by the type of surfactant used. A commonly used surfactant for synthesizing mesoporous silica is cetyltrimethylammonium bromide (CTAB) [33]. CTAB has a positively charged, hydrophilic head group connected to a hydrophobic carbohydrate tail. This amphipathic structure allows CTAB molecules to form micelles in aqueous solutions above the critical micelle concentration. A mechanism for mesoporous silica growth, proposed by Nooney and coworkers, suggests that silica oligomers form primary particles with CTAB through a strong interaction with the positive ammonium group and the negatively charged siloxide ions (figure 2.4) [34]. Subsequently, these primary particles aggregate around the CTAB framework, leading to mesoporous growth. After removal of the template, mesoporous silica is yielded. This procedure for mesoporous silica can also be used for CTAB-stabilized Au NPs in such a manner that a mesoporous silica shell is grown on Au NPs [33].

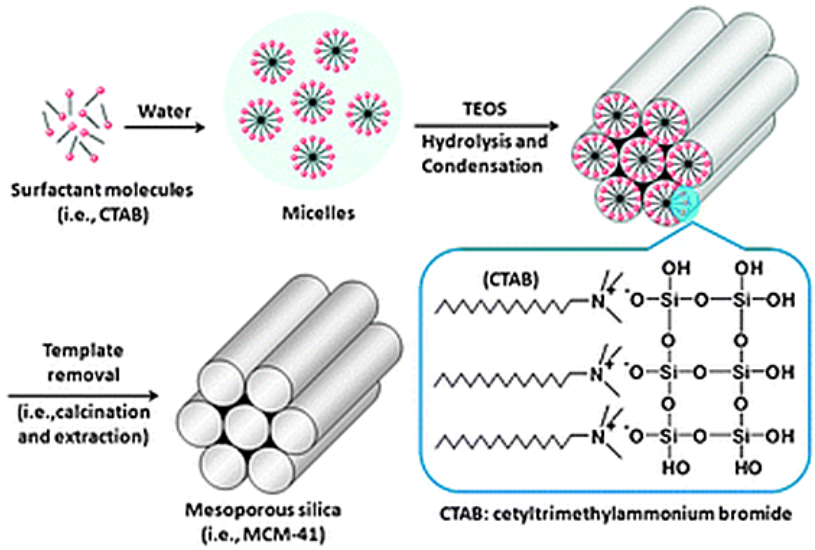

Figure 2.4: A schematic drawing of the formation of a mesoporous silica with CTAB as a template surfactant. The CTAB molecules self-assembly in rod micelles and form primary particles with silica oligomers, which can grow further around the micelles. After removal of the CTAB template, mesoporous silica is obtained. Reprinted from [35].

2.4 The overgrowth of Cu_xO

The synthesis of AuCu NPs in an aqueous solution is a promising area of research, but limited studies have been conducted on the topic. Current methods rely on co-reduction of Au and Cu precursors, resulting in alloyed AuCu NPs. Mixing Cu directly with Au can decrease the instability of Cu towards oxidation, which may account for its popularity. While co-reduction can result in uniform metal distributions, it can also lead to a wider size distribution. For example, Andoline et al. reported a co-reduction using sodium borohydride ($NaBH_4$) as reducing agent. Their AuCu NPs exhibited average diameters of 1.9–3.0 nm, but were relatively polydisperse [36]. Also, thiol ligands (PEG-SH) were used as ligands, as they adsorb strongly on Au NPs. However, thiol ligands tend to be unstable at elevated temperatures and can be sensitive to oxidation [37], which makes this procedure unsuitable. Another study by R. He et al. used glucose as reducing agent in the presence of hexadecylamine ligands and obtained more monodisperse AuCu NPs [38]. However, non-spherical shapes were obtained due to strong ligand binding to certain facets. The size could be tuned from 45 to 200 nm, which is relatively large for catalytic purposes. These examples illustrate that the synthesis of monodisperse, spherical AuCu

NPs through co-reduction in aqueous solution is challenging. Consequently, a sequential reduction could be considered more suitable.

In this strategy, a Cu precursor can be reduced in the presences of pre-synthesized Au NPs, which can act as a nucleation site. As a result, a Cu-based layer can be grown around the Au NPs, resulting in a core-shell structure. It is probable that Cu oxidizes when a sequential reduction is performed in an aqueous solution. Procedures for the aqueous synthesis of core-shell Au@Cu_2O NPs have been reported in literature, which involve the reduction of $CuSO_4$ with ascorbic acid [39, 40]. Ascorbic acid, also known as vitamin C, is a mild, non-toxic reducing agent. The redox half reactions involved in the reduction of Cu^{2+} ions with ascorbic acid ($C_6H_8O_6$) are shown in equation 2.1 and 2.2.

$$C_6H_8O_6 \longrightarrow C_6H_6O_6 + 2\,H^+ + 2\,e^- \tag{2.1}$$

$$Cu^{2+} + 2\,e^- \longrightarrow Cu \tag{2.2}$$

In this reaction, ascorbic acid donates two electrons to reduce Cu^{2+} to metallic Cu and forms dehydroascorbic acid. The reducing potential, and thereby the reducing rate, can be adjusted by the pH value of the solvent. The reduction potential of a chemical compound shows its tendency to gain or lose electrons and be reduced or oxidized, respectively. For instance, the more negative the reduction potential, the higher the tendency to donate electrons. This property can be used to predict whether a redox reaction will occur, as the difference in reduction potentials between two species describes the amount of energy required or generated from the reaction. The Nernst equations, simplified for the reduction of $CuSO_4$ with ascorbic acid, is displayed in equation 2.3 where E is reduction potential (V) and E_0 is the standard reduction potential (V). This equation shows that the reduction potential of ascorbic acid decreases with increasing pH, thereby increasing the reduction power [41]. As a result, the reduction of Cu^{2+} with ascorbic acid will be accelerated when the pH value is increased.

$$E = E^0 - 0.059pH \quad ; \quad E^0 = 0.08V \tag{2.3}$$

The pH of a solution can be increased by the addition of sodium hydroxide (NaOH). This can also promotes the formation of $Cu(OH)_2$, which can subsequently be reduced to Cu by ascorbic acid (equation 2.4 and 2.5).

$$Cu^{2+} + 2\,OH^{-} \longrightarrow Cu(OH)_2 \tag{2.4}$$

$$Cu(OH)_2 + C_6H_8O_6\text{-} \longrightarrow Cu + C_6H_6O_6 + 2\,H_2O \tag{2.5}$$

2.5 AuCu phase diagram

The phase diagram of a binary system is a graphical representation of the phases present in the system as a function of temperature and composition. It provides information about the relative stability of different phases and the conditions under which they transform into one another. The phase diagram of the bimetallic AuCu is particularly interesting due to the variety of disordered and ordered structures that can be formed upon alloying.

A phase diagram of AuCu systems has been presented in a study by Fedorov and Volkov (figure 2.5) [42]. This diagram shows the presence of both solid and liquid phases. The boundary between the solid and liquid phases is presented by the liquidus line, indicating the minimum temperature of 910°C at which a solid mixture of Au and Cu begins to melt. At temperatures below the liquidus line, intermediate compositions, represented between the two endpoints Au and Cu in the phase diagram, form a solid solution of Au and Cu. Upon cooling below 410°C, the AuCu alloys can undergo a transformation from disordered to ordered structures with stoichiometry of Au_3Cu, AuCu, and $AuCu_3$. Their corresponding structural symmetries are displayed in figure 2.5. However, it should be noted that this phase diagram was designed for AuCu systems in bulk form. The phase diagram for NPs would differ. For instance, theoretical calculations have shown that the phase transitions occur at lower temperatures with decreasing particle sizes [43].

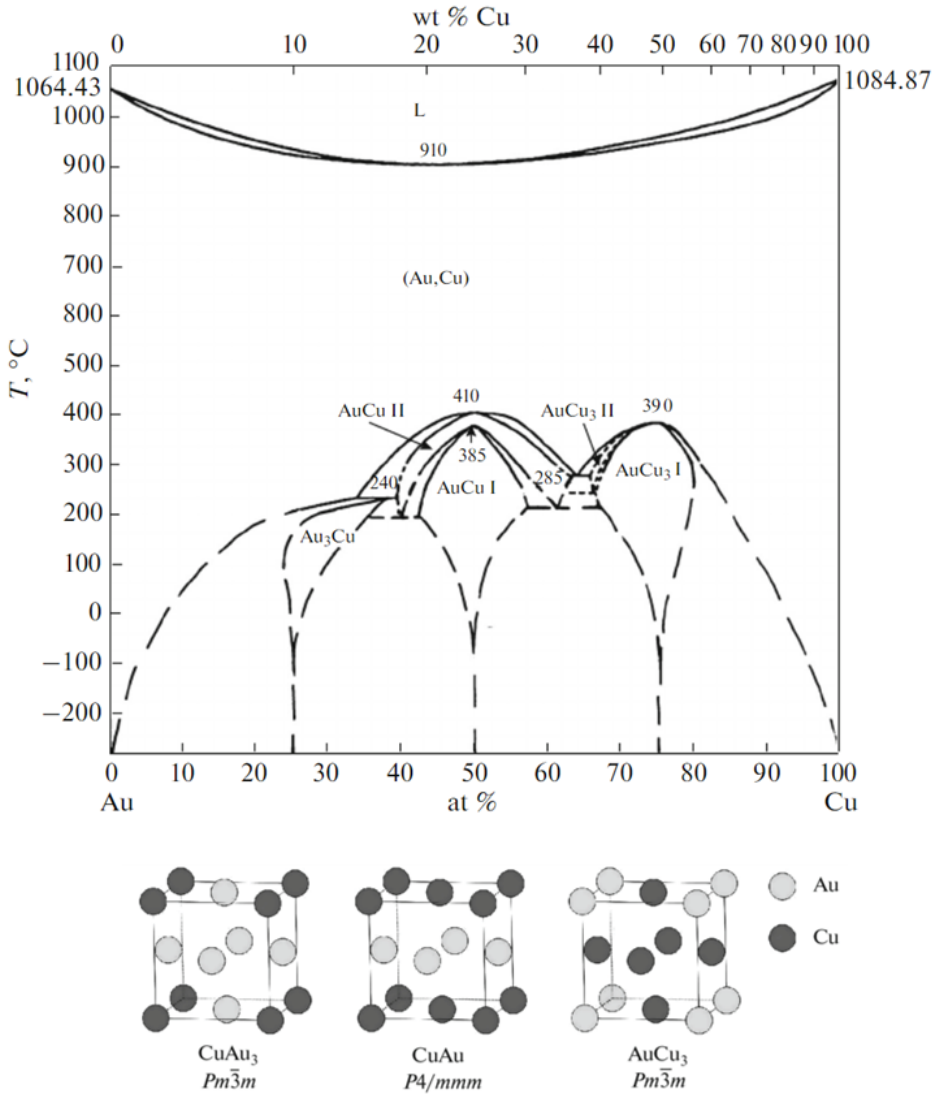

Figure 2.5: The phase diagram of AuCu systems with the crystal structures of ordered phase. Reprinted from [42].

2.6 Plasmon resonance

Colloidal metal NPs have been employed for their intense colors since ancient times. An extraordinary example is the Lycurgus cup, dated to the fourth century AD. The optical properties of the cup depend on the location of illumination. The colors arise from the Au and Ag NPs, which are incorporated in the glass [44]. The strong interaction between light and the metal NPs is attributed to plasmon resonance.

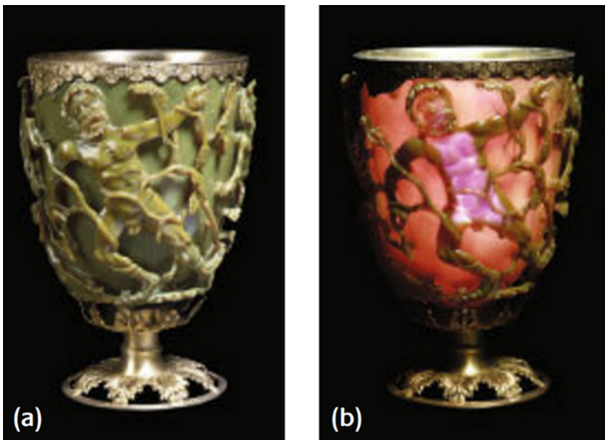

Figure 2.6: The Lycurgus cup exhibits different colors, depending on the position of illumination. It appears a) green when light is reflected off the surface of the cup and b) red when light is transmitted through the cup. This effect is caused by colloidal metal NPs in the glass. Reprinted from [44].

Plasmon resonance is an important optical property of metal NPs, since it allows for easy characterization and enables multiple applications. When the electromagnetic field of a light wave passes through a metal NPs, a collective oscillation of conduction electrons, known as plasmon, can be induced [45]. For NPs smaller than the wavelength of the incoming light, the electrons become spatially confined, restricting rapid dephasing of the oscillating electrons. Hence, the surface plasmon resonance is no longer delocalized, resulting in a strong interaction between metal NPs and light. This is referred to as localized surface plasmon resonance (LSPR). Au, Ag and Cu NPs have a strong plasmon resonance in the visible spectral region [46]. Most other transition metals have a weak plasmon resonance in the ultraviolet region.

Surface plasmon resonance can be detected with a ultraviolet-visible (UV-VIS) spectrometer. Strong extinction of light is measured when the frequency of the incident light corresponds to the frequency of the resonating electrons. This causes a peak in the UV-VIS spectrum. The wavelength at the maximum extinction of this peak is referred to as λ_{LSPR}. This resonance frequency is dependent on the size, shape, composition and medium of the metal NPs. It also defines the color of a colloidal suspension of metal NPs. The effect of particle size on the exhibiting color of colloidal dispersions of Au NPs is demonstrated in figure 2.7. As the particle size decreases, the extinction shifts towards shorter wavelengths, thereby yielding deep red colors for Au NPs smaller than 30 nm, and

purple-blue colors of larger Au NPs. As a result, the color of the colloidal dispersion can be used as an indication of size and aggregation.

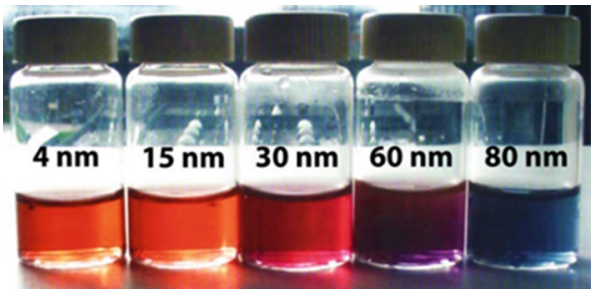

Figure 2.7: A colloidal dispersion of Au NPs in water with particle sizes ranging from 4 nm up to 80 nm. Reprinted from [25].

This size effect, described by Mie's theory, only holds for NPs larger than 20 nm [46]. Otherwise, the dielectric function of the metal NPs becomes size-dependent, such that intrinsic size effects dominate. The amount of electrons in NPs smaller than 20 nm is significantly low. Since the plasmon resonance is caused by a collective oscillation of electrons, the intensity of the plasmon resonance peak dampens instead of shifting its position [46]. This intrinsic size effect can also be observed in figure 2.7, as the color of the Au NPs dispersion does not significantly change between 4 nm and 15 nm.

Altogether, UV-VIS spectroscopy is a valuable technique for characterization of metal NP dispersions. It can be used to monitor the diameter and concentration of the NPs. In this thesis, UV-VIS spectroscopy has also been applied for characterizing the Cu_xO overgrowth on Au NPs. A successful overgrowth can be indicated by a shift of the LSPR band towards longer wavelengths, as shown in figure 2.8 [39]. This red-shift is attributed to the significant change in dielectric media. The Au atoms are no longer surrounded by water molecules when Cu_xO is grown on the surface, resulting in a change of dielectric constant from 78 to 7.5 [47]. The extinction of the LSPR peak also increases after the Cu_xO overgrowth due to the expanding particle size. The increase of extinction at short wavelengths arises by interband transitions (e.g. charge transfer) of the Cu_xO shell [48].

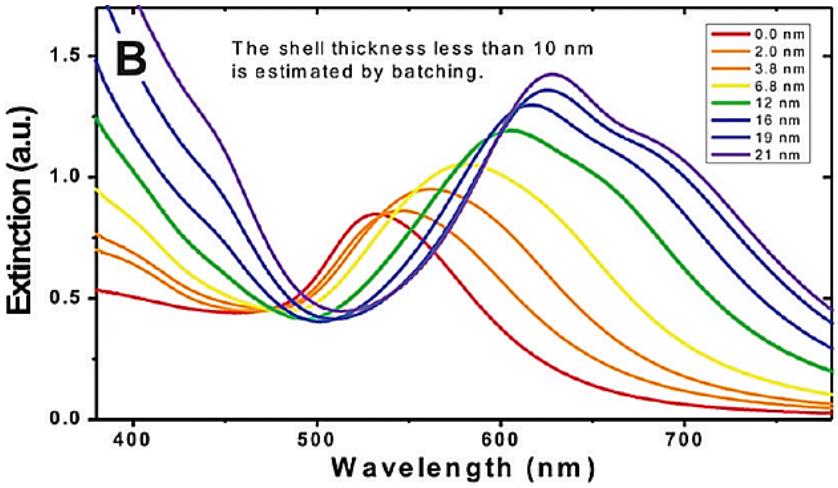

Figure 2.8: An UV-VIS spectrum of core-shell Au@Cu_2O NPs with a varying thickness of the Cu_2O shell. The thicker the Cu_2O shell on the Au NPs, the more the LSPR band is shifted towards longer wavelengths. Reprinted from [39].

2.7 CO oxidation

Carbon monoxide (CO) is a dangerous gas. Exposure can be fatal to humans, as CO can strongly bind to hemoglobin in blood cells, thereby hindering oxygen from being transported. Due to its lack of colour, taste and odour, CO is often referred to as the 'Silent Killer' [49]. CO is mainly emitted by incomplete combustion of fossil fuels [50]. As these fuels are used in daily life, CO emission poses a serious threat for human health and the environment. Catalytic CO oxidation is regarded as one of the most effective methods to remove CO pollution from the air [50]. CO oxidation is the chemical reaction between oxygen and CO leading to the formation of carbon dioxide (CO_2):

$$2\,CO + O_2 \longrightarrow 2\,CO_2 \tag{2.6}$$

In addition to its practical significance, catalytic CO oxidation is also extensively investigated for fundamental purposes [51]. Owing to its simple molecules, CO oxidation is a valuable probe reaction to fundamentally study catalytic properties and reaction mechanisms.

Many noble metal catalysts have been of interest for the oxidation of CO. For instance, platinum (Pt) and palladium (Pd) are widely used in automotive catalytic converters

to eliminate CO from exhaust gases. Au-based catalysts have also found promise for CO oxidation. On the contrary to Pt and Pd, Au NPs catalysts have shown to provide excellent activity at low temperatures [50, 2]. Due to the high cost and scarcity of noble metals, transition metal NPs also gained attention as catalysts for CO oxidation. Among these metals, Cu-based catalysts are considered as a plausible replacement for noble metal catalysts [52]. Cu mainly exist in the form of metallic Cu, and oxides CuO and Cu_2O. In the past decades, it has been demonstrated that CO oxidation can be catalysed by all three Cu species [53]. However, it is still unclear which oxidation state exhibits the best catalytic performance, as the preparation and composition of catalysts material differ throughout reports [54]. Additionally, the oxidation state of the Cu species can change in the course of the reaction, which makes the identification of the most active state challenging. It is even probable that CuO, Cu_2O and Cu coexist, depending on the reaction temperature and CO/O_2 ratio.

The reaction mechanism of CO oxidation has been studied extensively. Although, it has been classified as a simple reaction, different reaction mechanism were found to prevail for different catalysts materials. The traditional Langmuir-Hinshelwood (LH) and Eley-Rideal (ER) mechanism have been linked to CO oxidation on Pt-based catalysts [51, 55]. When CO oxidation follows the LH mechanism, O_2 is dissociated on the metal surface to react with adsorbed CO and desorb as CO_2 [56]. The ER mechanism involves the direct reaction of gas molecule CO with pre-adsorbed and activated O_2. On the other hand, the Mars van Krevelen mechanism has been reported for catalysts with O-vacancies [50]. The initial step in the MvK mechanism is the oxidation of adsorbed CO by a lattice oxygen atom. Subsequently, molecular oxygen replenishes the surface vacancy. This activates O_2 to react with another adsorbed CO molecule and restore the catalytic surface.

Jernigan and Somorjai proposed the LH mechanism for reactions over a Cu surface [53]. However, the MvK mechanism is mainly reported for Cu-based catalytic CO oxidation, since Cu undergoes oxidation during the reaction, forming catalysts with O-vacancies [52, 57].

Regarding Au catalysts in CO oxidation, it has been established that CO adsorbs on its metal surface. However, Au does not oxidize due to its extreme nobility. DFT calculations showed that the energy required for O_2 dissociation on Au surfaces is too high at the conventional reaction temperatures, prohibiting activation of O_2 on the Au surface [58, 59]. Consequently, it is more probable that O_2 is activated by an active oxide support, such as TiO_2. This could proceed via a LH and/or MvK mechanism. However, CO oxidation can also occur on Au NPs dispersed on an inactive support, such as SiO_2. It has been suggested that CO oxidation could be initiated via an interaction between O_2 and adsorbed CO to form an O−OCO complex, thereby activating O_2 (figure 2.9) [59]. This would explain why CO oxidation is slower on Au supported on inert materials.

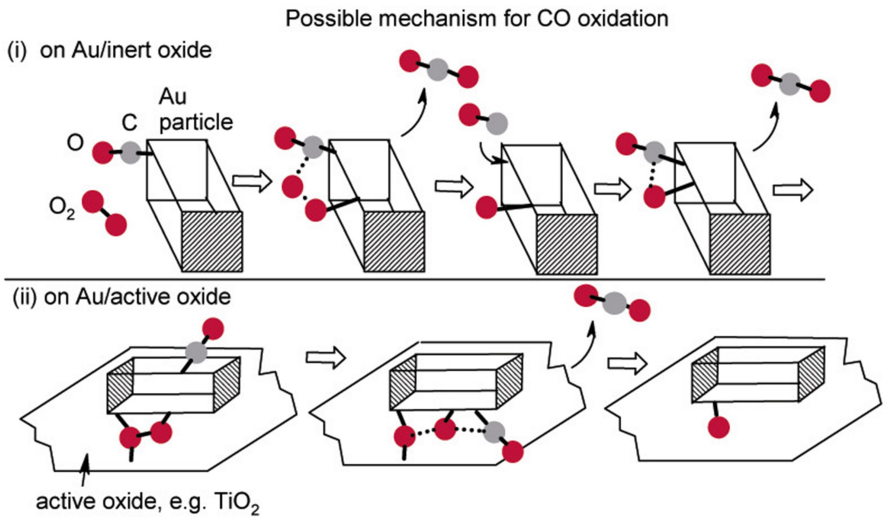

Figure 2.9: Possible mechanism for CO oxidation on Au catalysts dispersed on an inert oxide or active oxide. Reprinted from [59].

To promote the catalytic performance of these Au catalysts, Cu can be introduced. While Au can act as the active site for CO, Cu can play a significant role in activating O_2 [14]. The catalytic performance of AuCu NPs on supports, such as SiO_2, TiO_2 and SBA-15 for CO oxidation has already been studied [60, 61, 62]. It has been observed that a phase separation into Au–Cu_xO or AuCu−Cu_xO structures is crucial for high catalytic activity [14]. However, the optimal metal composition has yet to be determined as a thick layer of Cu_xO might block the Au-active sites for CO adsorption.

3 Experimental methods

The following chapter describes experimental details regarding synthesis and characterization methods used throughout this thesis. This thesis covers three different routes for synthesizing AuCu NPs in aqueous solution. Generally, the methods involve the growth of oxidized Cu on Au NPs, followed by a thermal treatment under reducing atmosphere in order to obtain AuCu NPs. The routes are further elaborated in chapter 4.

3.1 Chemicals

The chemicals were purchased from Sigma-Aldrich, unless indicated otherwise.

L–ascorbic acid (AA, $\geq$ 99%), copper(II)sulphate pentahydrate ($CuSO_4 \cdot 5\,H_2O$), hydrochloric acid (HCl, 37 wt.%), hydrogen peroxide (H_2O_2, 30 wt.%), methanol (MeOH), polyvinylpyrrolidone (PVP, MW 55000), potassium carbonate (K_2CO_3, $\geq$ 99%), sodium borohydride (BH), sodium hydroxide (NaOH, pellets, $\geq$ 98%), tannic acid (TA), tetrachloroauric (III) acid ($HAuCl_4$, 99.9%), tetraethyl orthosilicate (TEOS, 98%), toluene and trisodium citrate dihydrate (SC, $\geq$ 99%). Aerosil (OX50 and 300) was purchased from Degussa, cetyltrimethylammonium bromide (CTAB, $\geq$ 98%) from TCI America and ethanol (EtOH, 99.5%) and ethylene glycol ($\geq$ 99%) from Acros Organics. Ultrapure water was used with a resistivity of 18.2 MΩ cm (Millipore Milli-Q grade).

The chemicals were used as received without further purification. The glassware used for synthesis was cleaned with aqua regia (HCl / HNO_3) in a 3:1 ratio by volume.

3.2 Au NPs synthesis

The Au NPs were synthesized following a seed-mediated growth method based on the work of Piella et al. [28].

Au seeds The Au seeds were prepared by adding 450 mL 2.2 mM sodium citrate (SC), 0.3 mL 2.5 mM tannic acid and 3 mL 0.15 M K_2CO_3 to a 1 L round bottom flask placed in a 70°C oil bath. While stirring at 700 rpm (revolutions per minute), 3 mL 25 mM $HAuCl_4$ was added. The reaction mixture immediately turned black-purple. After several minutes, the color changed to red-orange, which indicates the formation of tiny Au NPs.

seeded-growth For growing the Au seeds, the reaction mixture was diluted by adding 165 mL 2.2 mM SC solution and extracting 165 mL seed solution (referred to as batch 1). Next, 1.5 mL 25 mM $HAuCl_4$ was added twice with a 10 min time interval. Subsequently, 165 mL of the reaction mixture was extracted (batch 2). The dilution with SC solution and addition of $HAuCl_4$ can be repeated until the desired particle size is reached. Typically, the steps were repeated four times, so that six batches of citrate-stabilized Au NPs were obtained.

3.2.1 PVP functionalization

The citrate ligands surrounding the Au NPs were exchanged for PVP ligands by adding 4.8 mL of PVP (1g/10mL H_2O) to 200 mL of as-synthesized Au NPs solution ($\lambda_{LSPR} = 400, Ext = 0.33$). The solution was stirred overnight at 500 rpm . Thereafter, the mixture was centrifuged at 15 000 rcf (relative centrifugal force) for an hour (Rotina 380R Hettich centrifuge). The supernatant was discarded and the PVP-functionalized NPs (Au@PVP) were redispersed in 200 mL water.

Extinction spectra of the Au NPs were recorded before and after performing the ligand exchange.

3.3 Synthesis route 1

The following experimental details are applicable for the first synthesis route.

3.3.1 Mesoporous silica coating

The Au NPs were coated with a mesoporous silica shell according to the method of Gorelikov et al [33], typically yielding a 13-15 nm coating.

First, the PVP ligands on the Au NPs were exchanged with CTAB ligands. 100 mL of the stored Au@PVP solution ($\lambda_{LSPR} = 400, Ext = 0.33$) was transferred to a 250 mL round bottom flask, placed in a 40°C water bath. Then, 1.0 mL 0.15M aqueous CTAB solution was added, while magnetically stirring at 750 rpm. After cooling down to 30°C, 1.0 mL of 0.1M NaOH was added to the reaction mixture, while stirring at 400 rpm. Next, 0.33 mL of TEOS in EtOH (20 vol%) was added three times with 45 minutes time intervals. After 48h, the silica-coated Au NPs (Au@SiO_2) were washed with water and EtOH by centrifugation (15 000 rcf, 30 min), and redispersed in 100 mL EtOH for storage.

3.3.2 Removal of CTAB ligands

The mesopores of the silica coated Au NPs were opened by removal of the CTAB ligands with an acid treatment. 5 mL dispersion of Au@SiO_2 in EtOH was centrifuged at 10 000 rcf for 15 minutes, and redispersed in 5 mL EtOH with 41 μl of concentrated HCl (12.1 M) was added. After several minutes, the NPs were washed twice with EtOH (15 000 rcf, 30 min) and stored at 4°C.

3.3.3 Oxidative etching

The Au@SiO_2 NPs can be etched with H_2O_2 as oxidizing agent to create more space between the Au core and silica shell to accommodate the metal overgrowth. The oxidative etching was carried out on untreated Au@SiO_2 NPs, according to the procedure of Van der Hoeven et al. [68]. Etching of the Au core can be tuned by varying the amount of H_2O_2 solution, the temperature and the etching time.

First, 2.4 mL stored Au@SiO_2 ($\lambda_{LSPR} = 525, Ext = 0.53$) were centrifuged at 10 000 rcf for 30 minutes, and redispersed in 2.4 mL MeOH. The Au@SiO_2 NPs in MeOH were added to a 20 ml vial and placed in a 60°C oil bath, while stirring at 400 rpm. 41 μl HCl (12.1 M) and 41 μl of H_2O_2 (0.5 vol%) in MeOH were added to initiate the etching. After 4 minutes, the reaction mixture was removed from the oil bath and quenched with 2.4 mL ice cold MeOH. The etched Au@SiO_2 NPs were washed with MeOH and water by centrifugation (15 000 rcf, 1h), and redispersed in 2.4 mL EtOH for storage. The NPs were redispersed in 5.0 mL ethylene glycol if the etched Au@SiO_2 NPs were directly used

for the Cu_xO overgrowth.

3.3.4 Cu_xO overgrowth on $Au@SiO_2$ NPs

The procedure for the Cu_xO overgrowth is based on the aqueous synthesis of Cu NPs, reported by Khan et al. [70]. The following procedure is described for non-etched $Au@SiO_2$ NPs, but can also be performed on etched NPs.

First, 5.0 mL $Au@SiO_2$ in ethylene glycol ($\lambda_{LSPR} = 525, Ext = 0.25$) and 0.25 mL 10 mM $CuSO_4$ were added to a 50 mL three neck flask. The flask was then attached to a Schlenk line, and degassed by flushing 10 times with nitrogen. Next, the flask was placed in an 80°C oil bath, followed by addition of 0.25 mL 80 mM ascorbic acid (AA) solution under a nitrogen flow. The flask was degassed again to remove residual air. After 5 minutes, the color of the reaction mixture slowly changed from pink to dark red, indicating the formation of individual Cu-based particles. After approximately an hour, the color changed to slightly darker pink than the initial color. Subsequently, the NPs were washed with water and EtOH (20 000 rcf, 1h), and redispersed in 5.0 mL EtOH. The NPs were stored at 4°C to slow down the dissolution of Cu_xO.

3.4 Synthesis route 2

The following experimental details are applicable for the second synthesis method.

3.4.1 Cu_2O overgrowth on Au NPs

The Cu_2O overgrowth on Au NPs synthesis was performed according to the procedure of Liu et al. [39]. The following description is for the synthesis of $Au@Cu_2O$ NPs with an atomic fraction of approximately 90% Cu. The metal composition can be tuned by varying the concentration of Au NPs, which is discussed in section 4.3.1.

First, 120 μl PVP (1g/10mL) and 125 μl 20mM CuSO4 were added to 5.0 mL Au@PVP in water ($\lambda_{LSPR} = 522, Ext = 0.2$), while stirring at 400 rpm. The reaction mixture was cooled down to $10°C$ with an ice-water bath. Next, 5.0 mL 0.1M AA and 5.0 mL 0.4 NaOH were added with a 5 minutes time interval. As the Cu content on the Au cores

increased, the color of the reaction mixture changed from red/pink to purple, blue, and green. After 15 minutes, an extinction spectrum was recorded. Thereafter, the Au@Cu_2O NPs were washed with water and EtOH, and redispersed in 5.0 mL EtOH (10000 rcf, 45 min). The Au@Cu_2O NPs were stored at 4°C.

The immobilization of Au@Cu_2O NPs on silica was carried out using the method for colloidal deposition, which is described in section 3.5.1.

3.5 Synthesis route 3

The following experimental details are applicable for the third synthesis method.

3.5.1 Colloidal deposition on a silica support

The NPs were stabilized on a mesoporous silica support (Aerosil OX50) with a reported surface area of 35 - 65 m^2/g. The following procedure describes the deposition of Au NPs, but this procedure can also be performed with Au@Cu_2O NPs.

First, 10 mL EtOH was added to 0.5 g of the silica support in a 20 mL vial, and sonicated for 10 minutes. Then, 50 mL Au@PVP in EtOH ($\lambda_{LSPR} = 522, Ext = 1.0$) was added, while stirring 400 rpm. The resulting turbid reaction mixture was equally divided in two 50 ml centrifuge tubes and sonicated for an hour. Next, 15 mL toluene was added to each centrifuge tube to promote the deposition on the silica support, followed by sonication for 5 minutes. The mixture was centrifuged at 2000 rcf for 15 minutes. The colorless supernatant, indicating the immobilization of Au NPs, was discarded. The pink colored support (Au@aerosil) was dried under a nitrogen flow for several minutes, and dried further at 60°C overnight in an oil bath.

3.5.2 Cu_2O overgrowth on supported Au NPs

This procedure is based on the procedure for Cu_2O growth on the Au NPs, described in section 3.4.1. The following description is for the synthesis of supported Au@Cu_2O NPs with approximately 0.87 wt.% Cu. The amount of $CuSO_4$ can be modified to obtain a different Cu content, which is further discussed in section 4.4.1.

First, 0.5 g of Au@aerosil is redispersed in 20 mL water in a 20 mL vial, followed by sonication for 10 minutes. The turbid mixture was further diluted by adding 50 mL water in a 100 mL round bottom flask. Then, 3.0 mL 20mM $CuSO_4$ solution was added to the reaction mixture, while stirring 400 rpm. The reaction mixture was cooled down in a 10°C water bath, followed by the addition of 4.0 mL 0.1M AA solution and 3.0 mL 0.4M NaOH with a 5 minute time interval. This resulted in a color change from dark pink to dark purple to blue in 10 minutes. Next, 20 mL EtOH was added and the reaction mixture was washed with a EtOH:water mixture (3:1) after centrifugation (2000 rcf, 15 min). After drying at 60°C overnight, the powder was sieved in a fraction of 75-150 μm.

3.6 Alloying via thermal reduction

After the metal overgrowth, a thermal treatment under a reducing atmosphere was applied to the NPs to reduce the oxidized Cu to its metallic form, resulting in mixing of Cu and Au atoms.

3.6.1 Ex-situ

On TEM grid The thermal treatment of non-supported NPs was carried out in a tubular oven (Thermolyne 79300 tube furnace) under a constant 10% H_2/Ar flow (∼100 mL/min). The NPs were first dropcasted onto a grid and then heated in a the tubular oven. After removing air with an Ar flow for 30 minutes, the NPs were heated to 300°C for an hour with a heating rate of 2°C/min. The NPs were cooled down under 10% H_2/Ar to room temperature before taking them out of the oven.

On SiO_2 support The supported NPs were heated in a tubular fixed bed reactor with a diameter of 2.4 cm. A flow of 10% H_2/N_2 flow was used with a rate of 300 mL/(min · gcat). The NPs were heated to 500°C for an hour with a heating rate of 5°C/min. The NPs were cooled down under 10% H_2/N_2 to room temperature before removal from the oven.

3.6.2 In-situ

An in-situ alloying experiment was conducted, using a FEI Talos F200X operating at 200 kV. A solution of non-supported Au@Cu_2O NPs in EtOH was dropcasted on a silicon nitride chip, which was placed in a gas cell holder from Protochips. The chip was first heated to 150°C with a heating rate of 25°C/min and kept constant for 45 minutes. Then, the temperature was raised in increments of 50°C, starting at 150°C and reaching a final temperature of 400°C. The temperature was kept constant for 10 minutes. The measurements were performed under a 10% H_2/Ar flow. The exposure of the NPs to the electron beam was limited to HAADF-STEM imaging. The imaging was performed twice at each temperature, first when reaching the desired temperature and then after 10 minutes.

3.7 Catalytic testing

For testing the catalytic performance of the supported NPs in CO oxidation, a glass plug-flow reactor was used with a diameter of 4 mm and bed length of approximately 2.5 cm. The samples Au@aerosil, AuCu_1 and AuCu_2 on silica (AerosilOX50) were used, which are discussed in section 4.5.3. Since the particle size of the samples varied, their total metal surface area was corrected by adjusting the catalyst loading. The catalysts were mixed with silicon carbide (1:9) to avoid heat transfer limitations. Due to exposure of the catalysts to air, the NPs were pretreated in-situ at 300°C for an hour with a heating rate of 5°C/min. This pretreatment was performed under a flow of 10% H_2/He and a total flow rate of 40 mL/min, which was kept constant throughout the entire catalytic test. The reactor was cooled down to 30°C under 10% H_2/He. This pretreatment was not performed on calcined AuCu_2. After removal of H_2 through a He flow for 15 minutes, the reactor was exposed to 1% CO and 10% O_2, balanced with He. The temperature of the reactor was raised with 5°C/min from 150°C to 300°C in increments of 50°C. The temperature was kept constant for an hour. Subsequently, the reaction was stepwise cooled down with the same temperature profile. A gas chromatograph was recorded every 10 minutes to monitor the gas composition.

Table 3.1: The amount of loaded catalyst material based on the metal surface area.

catalyst material	average particle size (nm)	metal surface area (nm^2)*	loaded to reactor (mg)
Au@aerosil	12.3 ± 0.9	492 ± 52	16.4
AuCu_1	14.7 ± 1.6	685 ± 135	11.6
AuCu_2	15.8 ± 2.4	802 ± 253	10.1

**The metal surface area was calculated with the average particle size, determined from BF-TEM images.*

3.8 Characterization

The NPs were characterized with bright field-transmission electron microscopy (BF-TEM), energy dispersive x-ray (EDX) measurements obtained in scanning transmission electron microscopy (STEM) mode, selected area electron diffraction (SAED), Ultraviolet-visible (UV-VIS) spectroscopy, Fourier-transform infrared spectroscopy (FTIR) and X-ray diffraction (XRD). Details of the measurements are presented below.

Electron Microscopy BF-TEM images and electron diffractograms were obtained with a Technai20 microscope operating with an acceleration voltage of 200 kV. Prior to imaging, the samples in EtOH were dropcasted onto a Cu grid (200 mesh, Ted Pella) coated with a formvar/carbon film. HAADF-STEM images and EDX spectra were recorded using a Talos F200X microscope (acceleration voltage of 200 kV). The samples were prepared by casting few droplets of the sample on a 200 mesh molybdenum (Ted Pella) or aluminum (Van Loenen Instruments) grid, coated with a formvar film.

UV-VIS spectroscopy UV-VIS spectra were recorded with a Cary 60 UV/Vis spectrophotometer in a range of 400 nm to 800 nm. The samples were measured in a disposable plastic cuvette with a path length of 1 cm. Before recording the spectra, the cuvette was cleaned with EtOH on the outside.

ATR-FTIR spectroscopy ATR-FTIR measurements were recorded with a Nicolet iS5 FTIR spectrophotometer in the range of 4000 cm^{-1} to 400 cm^{-1}. 32 scans were accumulated for each spectrum with a peak resolution of 4 cm^{-1}. Prior to the measurement, the ATR crystal was cleaned with EtOH and a background spectrum was recorded.

XRD The X-ray diffractograms were obtained with a D2Phaser X-ray generator, equipped with a cobalt source ($\lambda = 1.79026$ Å). A voltage of 30 kV and a current of 10 mA was used. The diffractograms were recorded overnight in a 2θ range of 20° to 90° with a increment of 0.03° and a rotational speed of 15°/min. 2 seconds were spent on each step. Both liquid and solid phase samples were measured with XRD. A liquid sample was prepared by dropcasting a few droplets onto a low background silicon wafer sample holder, such that the entire surface was covered. The solvent was left to evaporate, resulting in a layer of NPs. The dropcasting was repeated 10-12 times. A solid sample was prepared by placing the sample in a powder sample holder. Care was taken that the sample did not stick out of the surface of the XRD holder.

4 Results and discussion

This chapter presents and discusses the results of synthesizing AuCu NPs via three different methods, which are explained in section 4.2, 4.3 and 4.4. In general, the three synthesis methods follow a similar approach:

1. Synthesis of Au NPs
2. Cu_xO overgrowth on Au NPs
3. Alloying via thermal reduction

The characterization of Au NPs is discussed in section 4.1. The results for the metal overgrowth on Au NPs is discussed for each synthesis route in section 4.2, 4.3 and 4.4. In section 4.5, the results on thermal reduction to obtain AuCu NPs are discussed. The catalytic performance of AuCu NPs in CO oxidation is discussed in section 4.6. Some samples are abbreviated with a sample ID. A description of the sample ID with corresponding synthesis route are listed in Appendix A (table A.1).

4.1 Characterization of Au NPs

The procedure from Piella et al. was used to synthesize Au NPs [28], as described in section 3.2. This protocol is well-established in literature and offers a high level of control over the size of the NPs. Hence, the synthesis of colloidal Au NPs is the starting point for all three methods for synthesizing AuCu NPs. Control over the particle size was achieved by separating the nucleation and growth steps (section 2.2). As a result, multiple growth cycles can be performed until the desired particle size is reached, resulting in multiple batches of Au NPs with different particle sizes.

The desired size range for this research was between 10 nm and 13 nm, which required four to six growth cycles. This range of particle size was of interest due to its relatively high surface area and ease of purification. Small particles have a relatively high surface area,

which is suitable for catalytic applications, because the catalytic reaction takes place on the surface of the metal NPs. However, particles smaller than 10 nm can be difficult to isolate from the reaction mixture by centrifugation, which makes the purification time-consuming.

Extinction spectra of six batches of Au NPs were recorded, as shown in figure 4.9a. These spectra exhibit a peak that corresponds to the collective oscillations of free electrons in the Au NPs when excited by electromagnetic radiation, known as localized surface plasmon resonance (LSPR). As explained in section 2.6, the LSPR peak is dependent on the size, shape, and composition of the NPs. Figure 4.9a demonstrates that the LSPR peak shifted from 502 nm to 519 nm, and the extinction increased after each growth cycle, as indicated by the arrow. This is attributed to the increasing particle size and corresponds well with previous research [28]. The particle size of the last three growth cycles (batch 4, 5 and 6) were determined with BF-TEM. A representative TEM image of batch 6 Au NPs is shown in figure 4.9b. The average particle size of batch 4, 5 and 6 Au NPs with their corresponding LSPR peak position is presented in table 4.1.

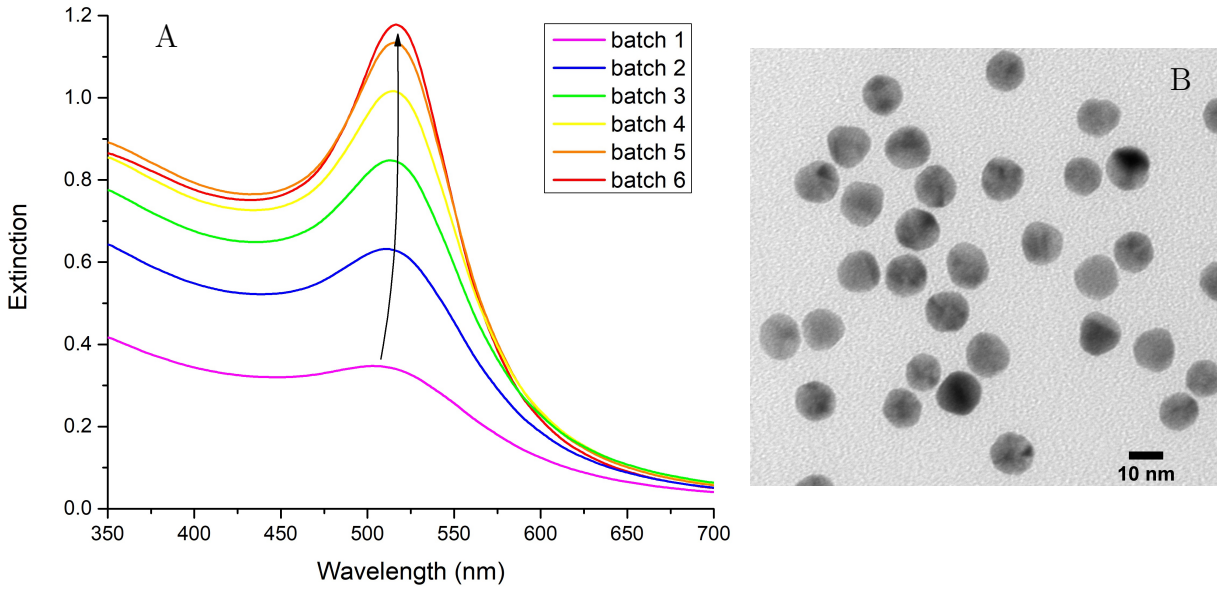

Figure 4.1: a) An UV-VIS spectrum of Au NPs after each growth cycle. The evolution of the LSPR peak maximum is indicated with an arrow. b) A representative BF-TEM image of batch 6 Au NPs with an average particle size of 12.3 ± 0.9 nm.

After the Au NPs synthesis, the citrate-stabilizing ligands were substituted for polyvinyl-pyrrolidone (PVP) ligands. This amphiphilic, bulky polymer is widely used as a stabilizing

Table 4.1: The LSPR peak position and average particle size of the last three growth cycles of Au NPs. The average particle size is determined from BF-TEM images.

batch	LSPR peak position (nm)	average particle size (nm)
4	516.9	10.1 ± 1.1
5	517.8	11.3 ± 1.0
6	518.5	12.3 ± 0.9

agent for metal NPs in aqueous and many non-aqueous solvents. For instance, PVP has been used as a stabilizing agent for the growth of a silica shell on Au NPs [63, 64] and for the aqueous synthesis of Cu NPs [65]. Additionally, it has been reported that PVP can form a complex with Cu^{2+}-ions by donation of its lone-pair electron, which could facilitate the Cu_xO overgrowth on NPs [66]. Hence, PVP is often employed for the Cu_xO overgrowth on Au NPs [39, 67]. PVP is also a non-ionic compound, which enables ligand exchange with charged ligands, such as CTAB. This ligand exchange is essential for the growth of a mesoporous silica shell on Au NPs, as explained in section 2.3

Batch 6 Au NPs were also analyzed with XRD (figure 4.2). The diffraction peaks at 2θ of 44°, 52°, and 77° correspond to Au(111), Au(200) and Au(220), respectively. The broadening near 77° corresponds to the background of the silicon wafer sample holder.

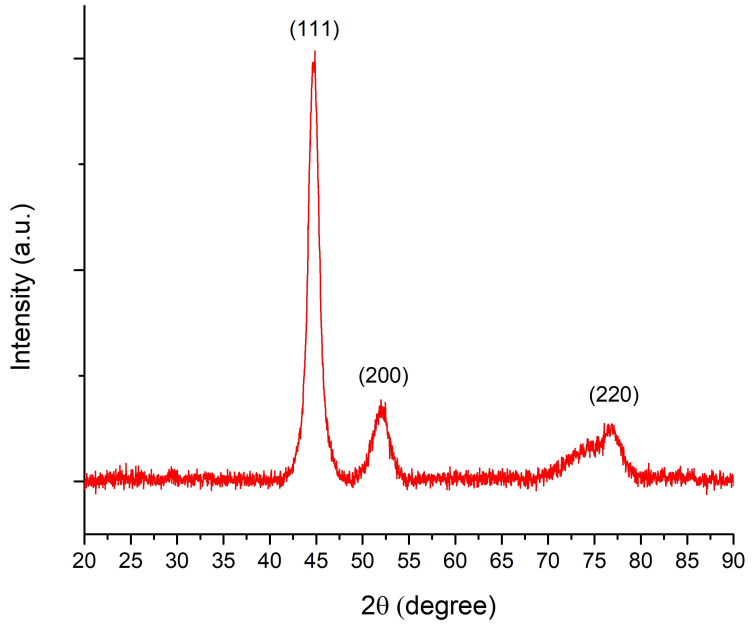

Figure 4.2: A XRD pattern of batch 6 Au NPs, stabilized with PVP ligands. The diffraction peaks are labeled with the miller indices of the corresponding lattices.

From the XRD pattern, the crystallize size of the Au NPs can be approached with the Scherrer equation:

$$L = \frac{K\lambda}{\beta \cos\theta} \tag{4.1}$$

where L is the average crystallize size, K is a shape factor, λ is the wavelength of the X-rays, β is the peak full width at half maximum (FWHM) and θ is the Bragg angle.

The Scherrer equation relates the broadening of a peak in a diffraction pattern with the crystalline size. Since the particles are spherical, a shape factor of 0.9 was used. By applying the Scherrer equation to the diffraction peak at 44°, corresponding to Au(111), the calculated crystalline particle size was found to be approximately 11 nm. This crystallize size is similar to the average particle size of 12.3 ± 0.89 nm, determined with BF-TEM. As the crystalline size represents the size of the individual crystals within a material, while the particle size refers to the size of the entire particle, including any non-crystalline regions, this result shows that the Au NPs are highly crystalline and have low degree of aggregation.

4.2 Synthesis route 1: Cu_xO overgrowth on silica coated Au NPs

The first route for synthesizing AuCu NPs is based on the synthesis of AuPd nanorods with a mesoporous silica shell, reported by Van der Hoeven et al. [30]. This route was used due to the high level of stability provided by the mesoporous silica shell, which can effectively prevent aggregation, thereby reducing loss of activity during catalysis. The protective silica shell also facilitates deposition on a support.

This route for synthesizing AuCu NPs involves the overgrowth of Cu_xO on Au NPs coated with a protective mesoporous silica shell, resulting in a core-shell structure (figure 4.3). The Cu content was modified through oxidative etching of the Au core [68]. The results on the silica shell growth and metal overgrowth are discussed in the following sections.

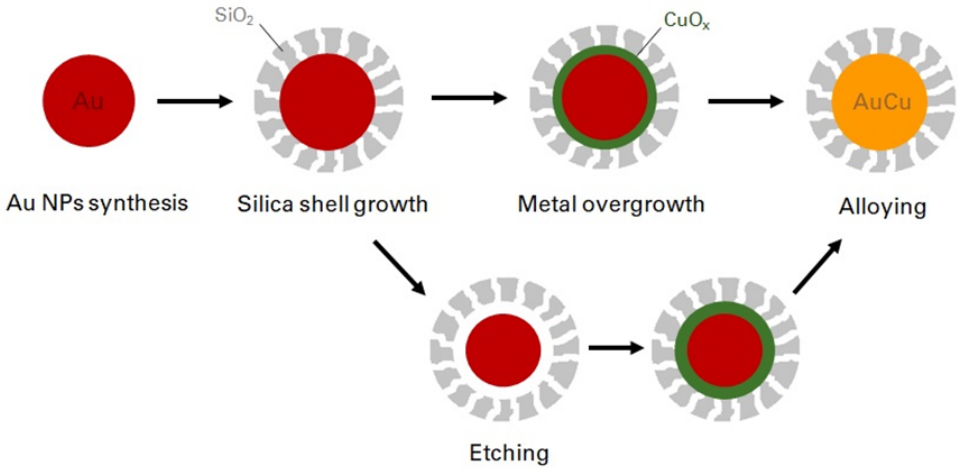

Figure 4.3: A schematic illustration of the first synthesis method for AuCu NPs. The procedure involves the sequential steps of (1) the growth of a mesoporous silica shell on Au NPs, (2) overgrowth of Cu_xO on the $Au@SiO_2$ NPs, and (3) thermal treatment under reducing conditions to promote mixing of the metals.

4.2.1 Characterization of $Au@SiO_2$ NPs

Prior to growing a silica shell on Au NPs, the PVP ligands were replaced by CTAB ligands, because the CTAB ligands serve as a template for the mesoporous structure. After the silica coating, the CTAB ligands were removed with an acid treatment (section 3.3.1), aiming for a more accessible metal surface. This did not have a significant effect on the

particle size, which was determined from BF-TEM images (figure B.1). A representative BF-TEM image of the Au NPs coated with a mesoporous silica shell (Au@SiO_2) is shown in figure 4.6. An average shell thickness of 13.9 ± 1.00 nm was measured from BF-TEM images.

The optical properties of Au NPs can be affected by a change in chemical environment, resulting in a shift in the LSPR peak. For instance, binding of different ligands on the Au core often changes the local refractive index. This was also observed for the ligand exchange from citrate to PVP. Figure 4.4 demonstrates the red-shift of several (2-3) nm was observed, as an indication of a successful ligand exchange. The effect of the mesoporous silica shell on the optical properties of Au NPs is also demonstrated in figure 4.4 in which a small peak shift of 3-4 nm towards longer wavelength can be observed. This red-shift is also caused by an increase in refractive index near the Au surface, as the refractive index of silica (1.45) is larger than water (1.33) [69].

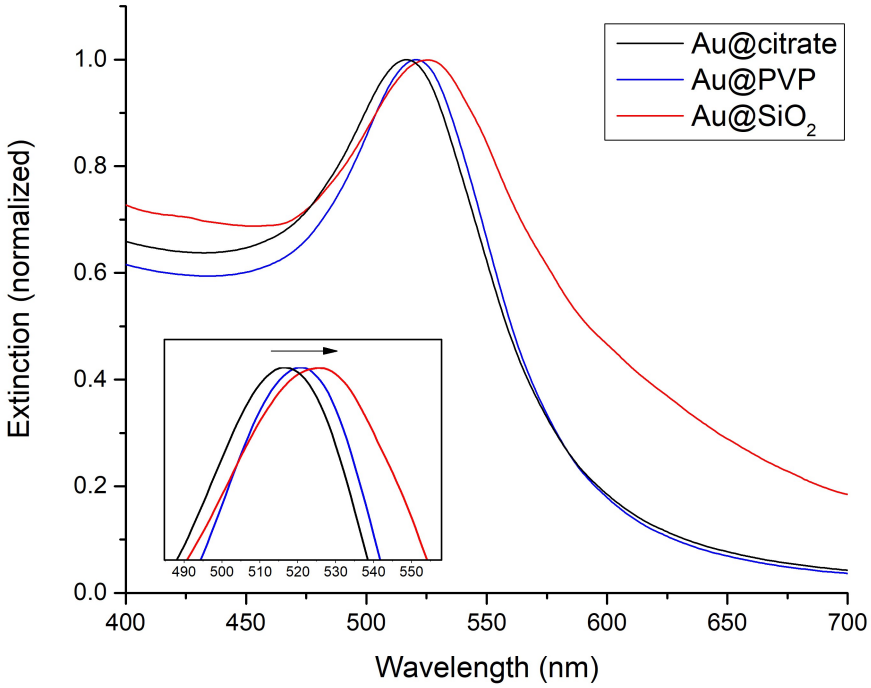

Figure 4.4: UV-VIS spectra of Au NPs stabilized by citrate (black), PVP (blue) and a mesoporous silica shell (red), normalized by peak height.

4.2.2 Cu_xO overgrowth on $Au@SiO_2$ NPs

After the silica shell growth and subsequent acid treatment, the Au core was overgrown with a Cu_xO shell by the reduction of $CuSO_4$ with ascorbic acid at 80°C [70]. This procedure was performed in ethylene glycol instead of water due to its reducing properties [66]. When using water as a solvent, it was necessary to increase the reducing power of ascorbic acid by lowering the pH in order to reduce the Cu^{2+} ions, as explained in section 2.4. However, by using ethylene glycol as solvent, the amount of ascorbic acid could be reduced and the silica shell was found to be more stable, because no basic condition were required to facilitate the reduction process.

Variation in $CuSO_4$ quantity

The procedure for the Cu_xO overgrowth on $Au@SiO_2$ NPs was performed, as described in section 3.3.4. The overgrowth was repeated with different quantities of Cu precursor with the objective of obtaining NPs with different Cu fractions. The results are presented in table 4.2. The samples are denoted by a sample ID, indicating the composition and the amount of Cu precursor utilized during synthesis.

Table 4.2: The peak position and average particle size of the NPs after the Cu_xO overgrowth on non-etched $Au@SiO_2$ NPs with various quantities of Cu precursor.

sample ID	amount of $CuSO_4$ (µl)	LSPR peak position (nm)	average particle size (nm)
$Au@SiO_2$	0	525	10.1 ± 1.3
$AuCu_xO@SiO_2$_100	100	528	10.6 ± 1.4
$AuCu_xO@SiO_2$_250	250	529	10.8 ± 1.8
$AuCu_xO@SiO_2$_1000	1000	580	not specified

Extinction spectra of the samples were recorded an hour after the addition of ascorbic acid (figure 4.5). The LSPR peak position of sample $AuCu_xO@SiO_2$_100 and $AuCu_xO@SiO_2$_250 shifted to longer wavelengths compared to $Au@SiO_2$, indicating the presence of Cu_xO on the Au core. The size distributions, determined with BF-TEM images, also shifted towards larger particles sizes with increasing Cu precursor (figure 4.6). The average size of $Au@SiO_2$ NPs prior to the metal overgrowth was 10.1 ± 1.3 nm, while the particle size of $AuCu_xO@SiO_2$_100 and $AuCu_xO@SiO_2$_250 increased to 10.6 ± 1.4 nm and 10.8 ± 1.8

nm, respectively. The increasing average particles size together with the LSPR peak shift in the UV-VIS spectra indicates a successful Cu_xO overgrowth.

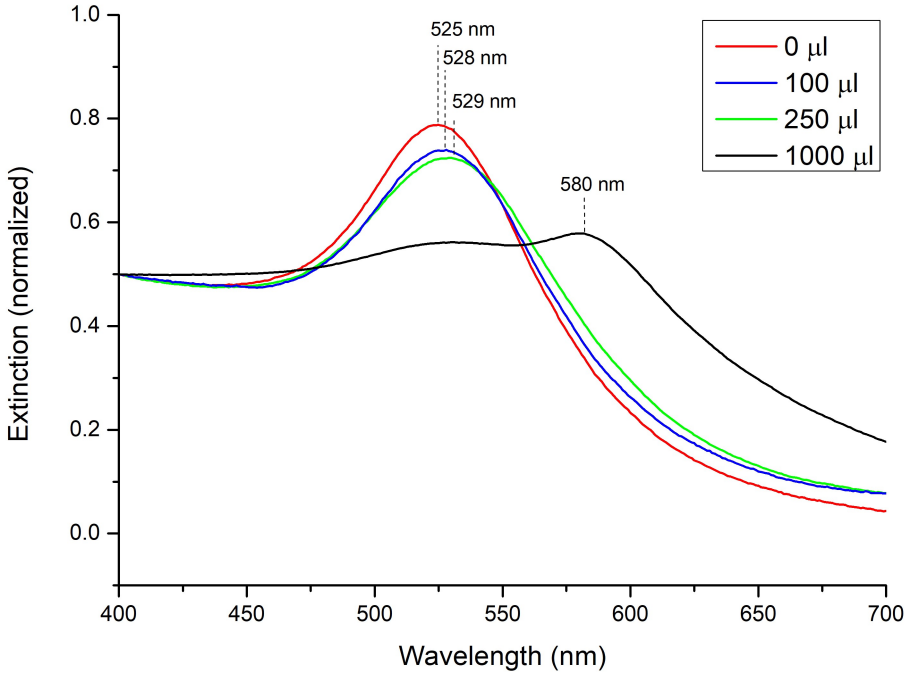

Figure 4.5: UV-VIS spectra of $Au@SiO_2$ after the Cu_xO overgrowth with different amount of Cu precursor. The extinction is normalized at 400 nm.

EDX measurements of sample $AuCu_xO@SiO_2$_250 confirmed that Cu species were accumulated around the Au cores (figure 4.7a). The core-shell structure was difficult to observe due to the small particle size, but became more discernible in EDX maps at a higher magnification (figure 4.7b). The presence of a core-shell structure is supported with a RGB plot in which the pixel intensity is plotted over particle distance. The plot demonstrates that the Cu signal is more extended than the Au signal, indicating a core-shell structure. The atomic Cu fraction, determined with EDX, corresponded to 11.4 ± 1.6%, which corresponds relatively well to the estimated Cu fraction of 14%, based on the particle volume increase from BF-TEM images. Remarkably, more Cu signal was observed on regions of the Au core where the silica shell was thinner in figure 4.7a. This suggests that the silica shell may restrict the metal overgrowth.

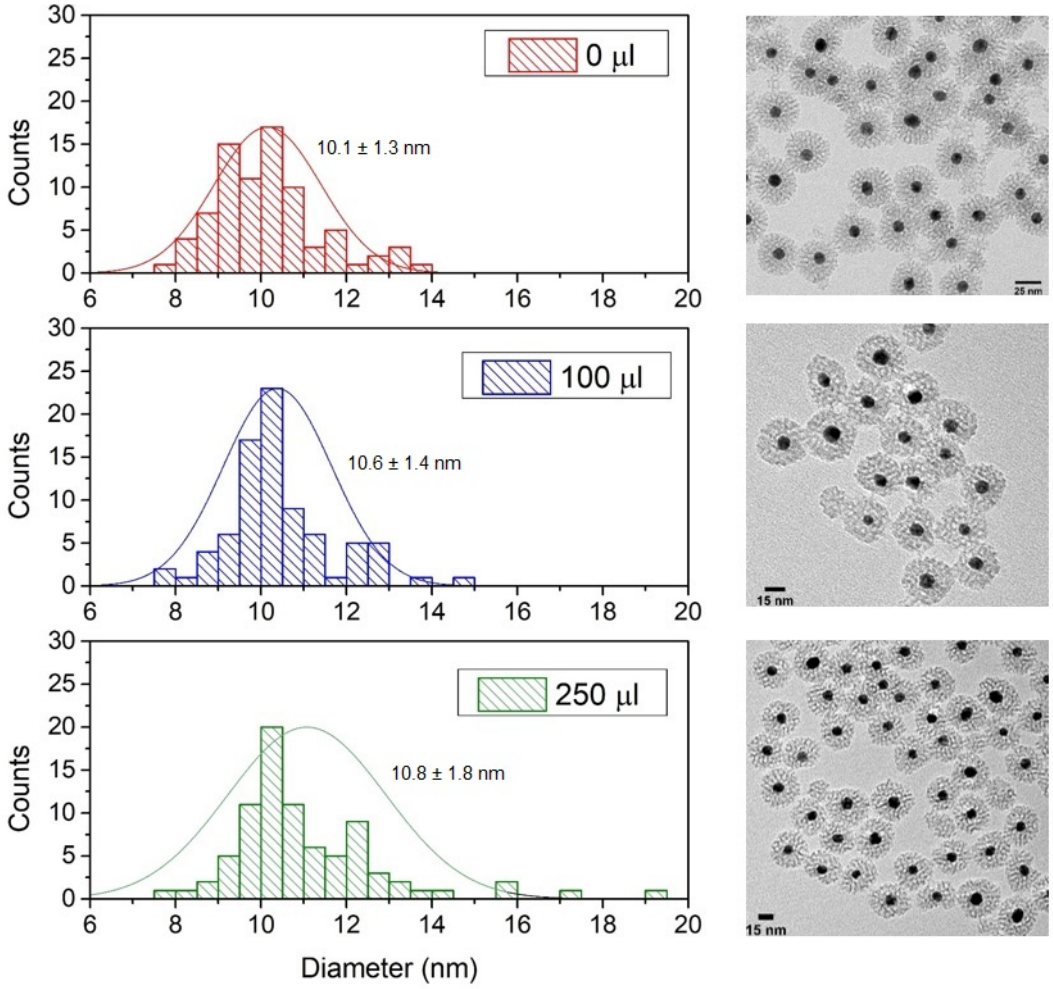

Figure 4.6: Histograms of $Au@SiO_2$, $AuCu_xO@SiO_2$_100 and $AuCu_xO@SiO_2$_250 with their mean particle size and corresponding BF-TEM images.

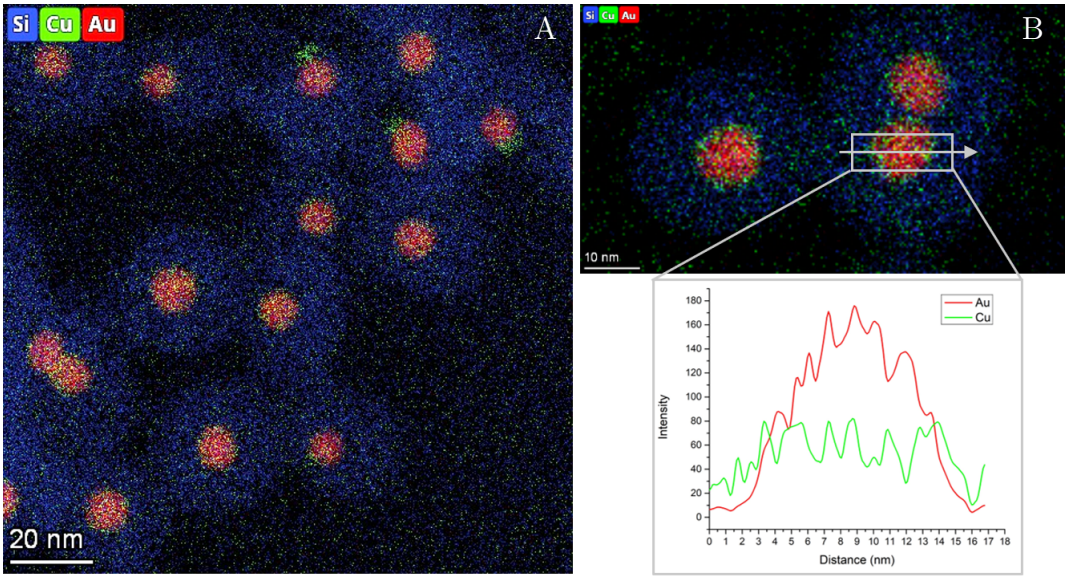

Figure 4.7: a) An EDX map of $AuCu_xO@SiO_2$_250 with an average atomic fraction of 11.4 ± 1.59% Cu. b) A RGB profile plot of a particle from an EDX map of $AuCu_xO@SiO_2$_250 over which the intensity of the red (Au) and green (Cu) pixels is plotted as a function of distance.

The LSPR peak corresponding to sample $AuCu_xO@SiO_2$_1000 shifted to much longer wavelengths, as shown in figure 4.5. The shoulder at 529 nm suggests that the NPs were overgrown with a similar Cu fraction as sample $AuCu_xO@SiO_2$_250. However, the presence of a second peak at 580 nm indicates the formation of individual Cu-based particles. This is in agreement with BF-TEM images, which show many polydisperse particles around the NPs (figure 4.8). EDX measurements confirmed that the polydisperse particles were composed of Cu species. This result shows that an excess of Cu precursor did not increase the Cu fraction on the Au core, but resulted in the formation of monometallic Cu species.

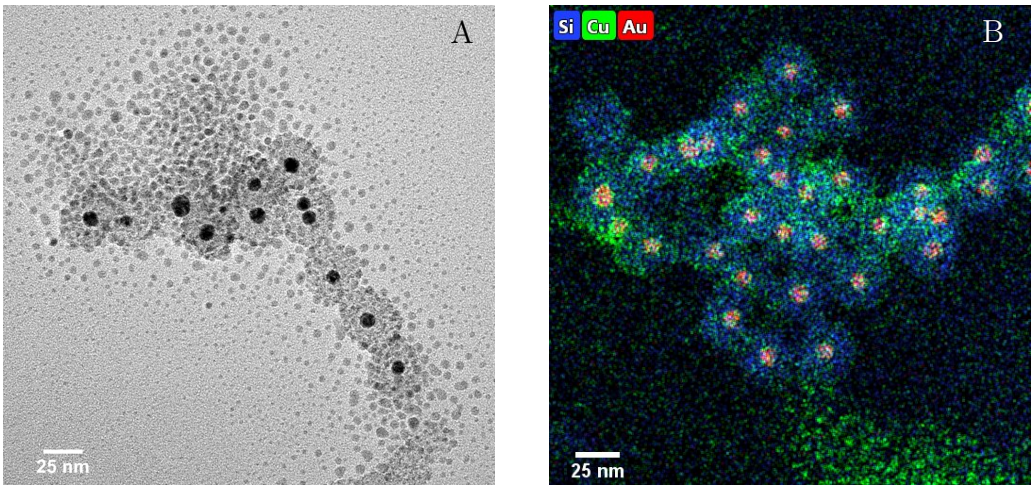

Figure 4.8: a) A BF-TEM image and b) EDX map of sample $AuCu_xO@SiO_2$_1000, confirming the formation of monometallic Cu-based particles.

The time-evolution of the Cu_xO overgrowth

The Cu_xO overgrowth was studied over time by taking aliquots during the reaction of $AuCu_xO@SiO_2$_250. The aliquots were measured with UV-VIS spectroscopy and are shown in figure 4.9a. 5 minutes after the addition of ascorbic acid (t = 5 min), the LSPR peak shifted from 525 nm to 569 nm. This shift was observed by the reaction mixture turning from clear pink to turbid red-brown. EDX was performed to determine if this peak shift to 569 nm occurred due to overgrowth of Cu_xO. Although an atomic Cu fraction of $26.7 \pm 1.74\%$ was detected on the Au core, the EDX map in figure 4.9b shows that a substantial Cu signal originated from the silica shell. Additionally, individual Cu-based particles were observed with BF-TEM (figure B.3). At t = 40 min, a second peak was measured at 524 nm, confirming the presence of monometallic Cu species, similar

to $AuCu_xO@SiO_2$_1000. At t = 60 min, the reaction mixture returned to a clear pink color, slightly darker than initially. This corresponded to a single LSPR peak at 529 nm, as demonstrated in figure 4.9. This peak was previously shown in figure 4.5 for sample $AuCu_xO@SiO_2$_250. Since the individual Cu-based particles were not observed at t = 60 min, it appears that the particles were not stable without ligands over time. No significant changes were observed after 24 hours, although the minor blue-shift of the LSPR peak indicated small amounts of Cu_xO dissolution from the Au core (figure B.2).

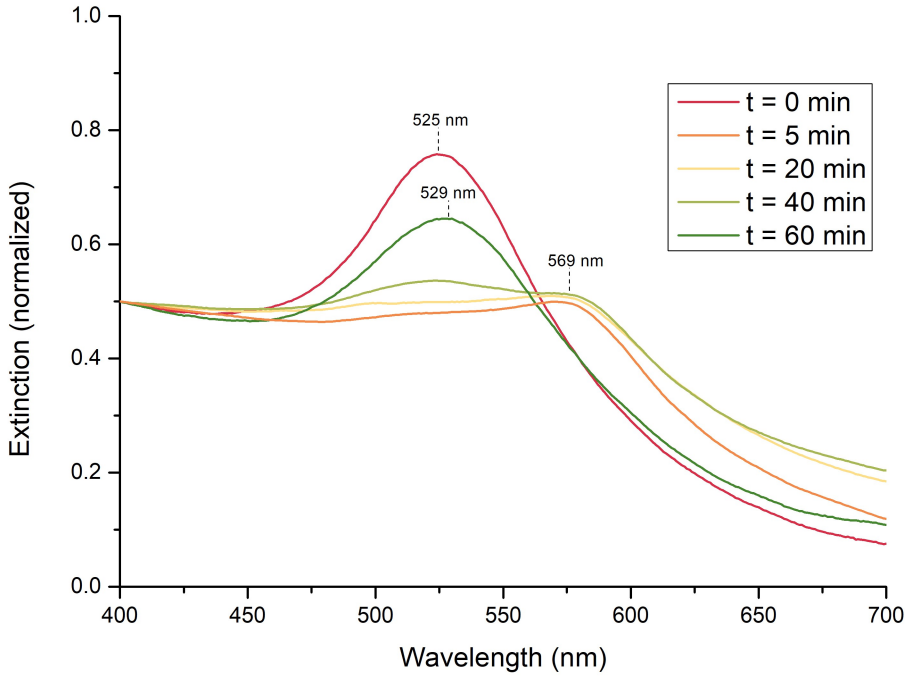

(a)

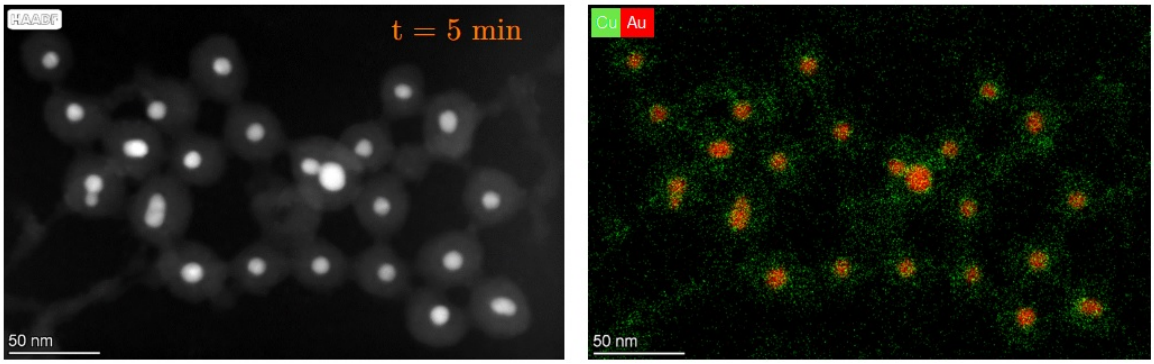

(b)

Figure 4.9: a) The time-evolution of the Cu_xO overgrowth during the reaction of $AuCu_xO@SiO_2$_250, studied with UV-VIS spectroscopy. The extinction spectra are normalized at 400 nm. b) A HAADF-STEM image with corresponding EDX map of $AuCu_xO@SiO_2$_250 at t = 5 min.

The extinction spectra, demonstrating the evolution of the metal overgrowth over time, show that Cu_xO did not gradually grow on the Au surface, but also grew in the silica shell and even outside the $Au@SiO_2$ NPs. Since this already occurred 5 minutes after the addition of reducing agent, it appears that the chemical reduction proceeded too rapidly.

Slowing down the Cu_xO overgrowth

In general, heterogeneous nucleation dominates homogeneous nucleation, because less energy is required for nucleation on a pre-existing surface. Therefore, the formation of monometallic Cu species suggests that the chemical reduction is taking place at an accelerated rate, where excess Cu can nucleate outside the Au surface. A strategy to regulate the reaction rate is adjusting the rate of reactant addition. It was hypothesized that a slower addition of the reducing agent could result in a more gradual reduction of the Cu precursor, thereby slowing down the metal overgrowth. Hence, the Cu_xO overgrowth was repeated with the addition of ascorbic acid at a rate of 4.167 μl/min with a total volume of 250 μl, using a syringe pump. However, extinction spectra, recorded during the reaction, in figure 4.10a illustrate that the results are similar as sample $AuCu_xO@SiO_2$_250. Although, the reaction proceeded slower, the presence of two peaks in the extinction spectrum at t = 60 min indicates the formation of individual Cu-based particles. Moreover, the LSPR peak at t = 120 min was less red-shifted, suggesting that a lower amount of Cu_xO had grown over the Au cores.

An alternative method to reduce the reaction rate is to lower the reaction temperature. Therefore, the synthesis of sample $AuCu_xO@SiO_2$_250 was repeated at 60°C instead of 80°C, and characterized with UV-VIS spectroscopy. The extinction spectra in figure 4.10b exhibit one single peak, indicating the absence of monometallic Cu species during the overgrowth. Unfortunately, the LSPR peaks were again less shifted compared to the reaction at 80°C in figure 4.9a.

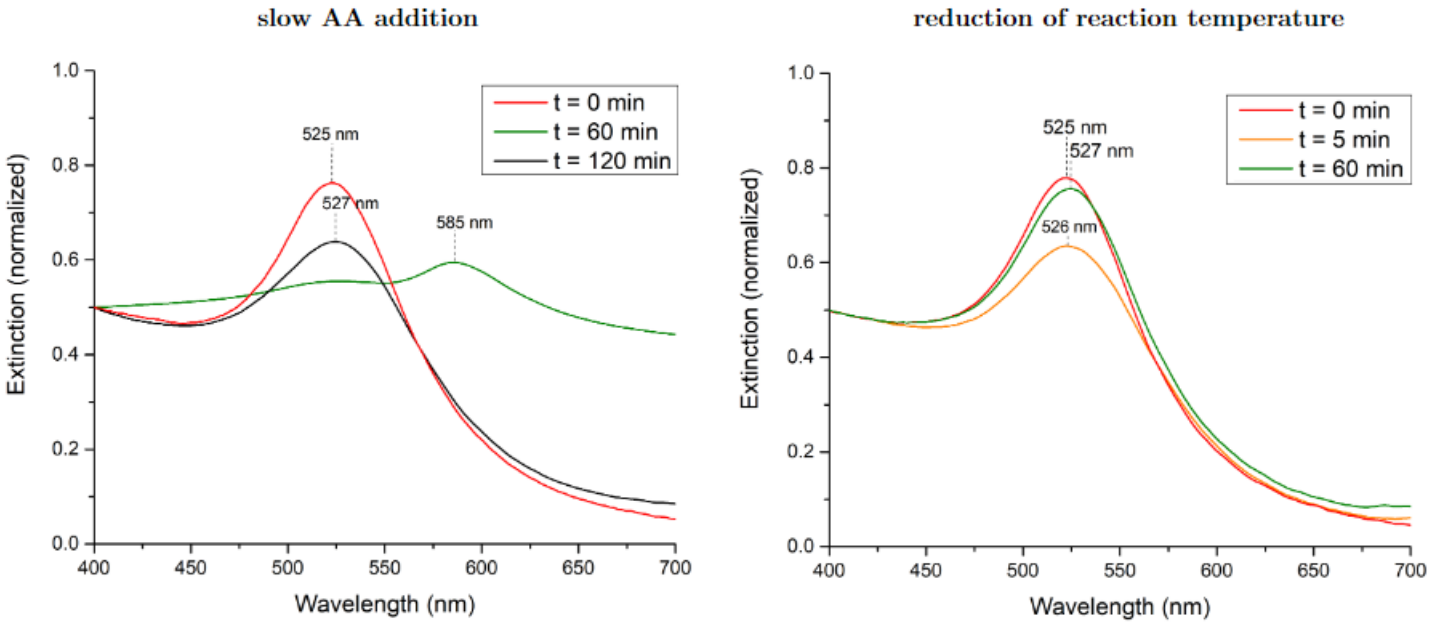

Figure 4.10: Extinction spectra of the Cu_xO overgrowth after decreasing the addition rate of ascorbic acid to 4.167 μl/min and decreasing the reaction temperature from 80°C to 60°C

These results demonstrate that adjusting the reaction temperature and the rate of ascorbic acid addition affected the rate of the chemical reduction. Furthermore, a lower reaction temperature appears to inhibit the formation of monometallic Cu species. However, the reduction in the red-shift of the LSPR peaks relative to $AuCu_xO@SiO_2$_250 indicates a decreased deposition of Cu_xO onto the $Au@SiO_2$ NPs.

Oxidative etching on the Cu_xO overgrowth

Section 4.2.2 demonstrated that the atomic fraction of Cu could not exceed approximately 11% by increasing the quantity of Cu precursor without the formation of individual Cu-based particles. The EDX map in figure 4.7 showed that the silica shell could have limited the Cu_xO overgrowth. Hence, the Au core was etched to determine if more Cu_xO could be deposited on $Au@SiO_2$ NPs by creating more space between the silica shell and Au core [30].

The oxidative etching of $Au@SiO_2$ NPs was performed according to the protocol in section 3.3.3. During an etching time of eight minutes, aliquots were taken every two minutes. Extinction spectra were recorded of each aliquot after quenching. The extinction drop

in figure 4.11a indicates the decrease in particle volume with etching time. This trend is verified by the decrease in mean particle size, determined with BF-TEM (figure 4.11b). Figure 4.11b also shows that the standard deviation increases with etching time, indicating that the Au@SiO_2 NPs became more polydisperse after etching. This is also evident by the broadening of the LSPR peaks after etching in the extinction spectra. The BF-TEM images in figure 4.12 provide a visual representation of the etched Au@SiO_2 NPs and demonstrate the growing polydispersity in the particles. In particular, BF-TEM images of the NPs after 6 or 8 minutes of etching show that some Au cores were subjected to significant etching while others remained relatively unchanged.

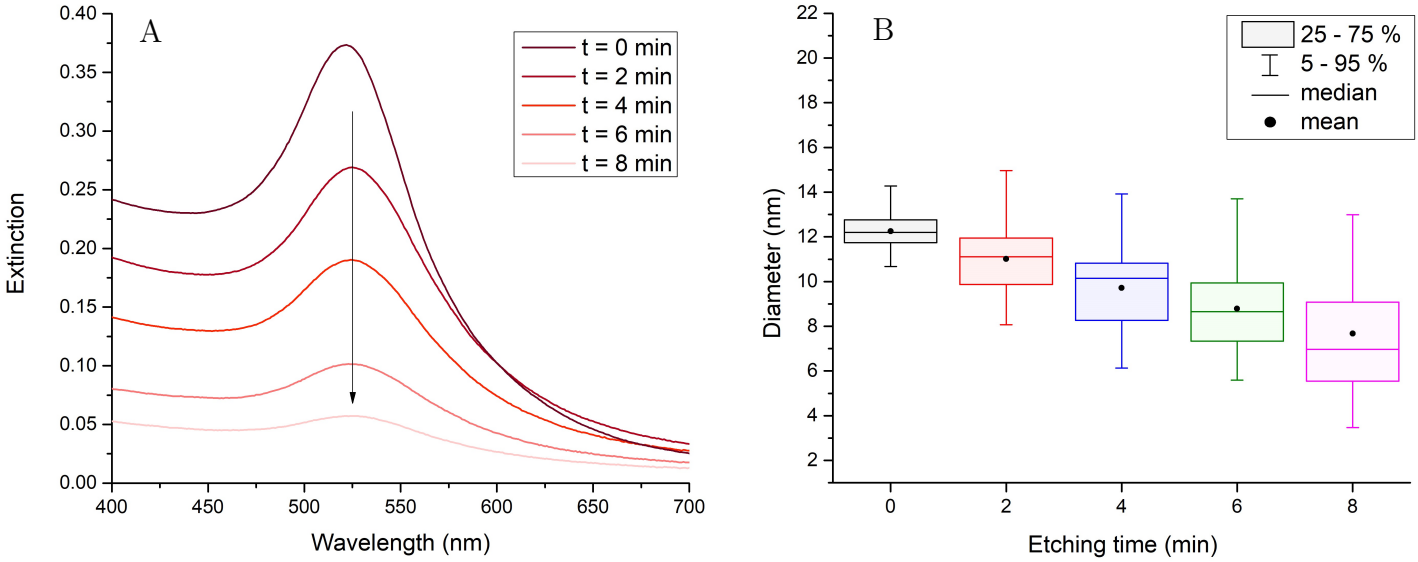

Figure 4.11: a) The extinction spectra of Au@SiO_2 after various etching times. b) A box plot showing the development of particle size over etching time. The boxes represent the particle sizes with a probability between 25% and 75%, with whiskers for 5% and 95% of the data set. The median size is presented by a line inside the box. The mean diameter is indicated with a bullet. The range of particle size was determined through BF-TEM images.

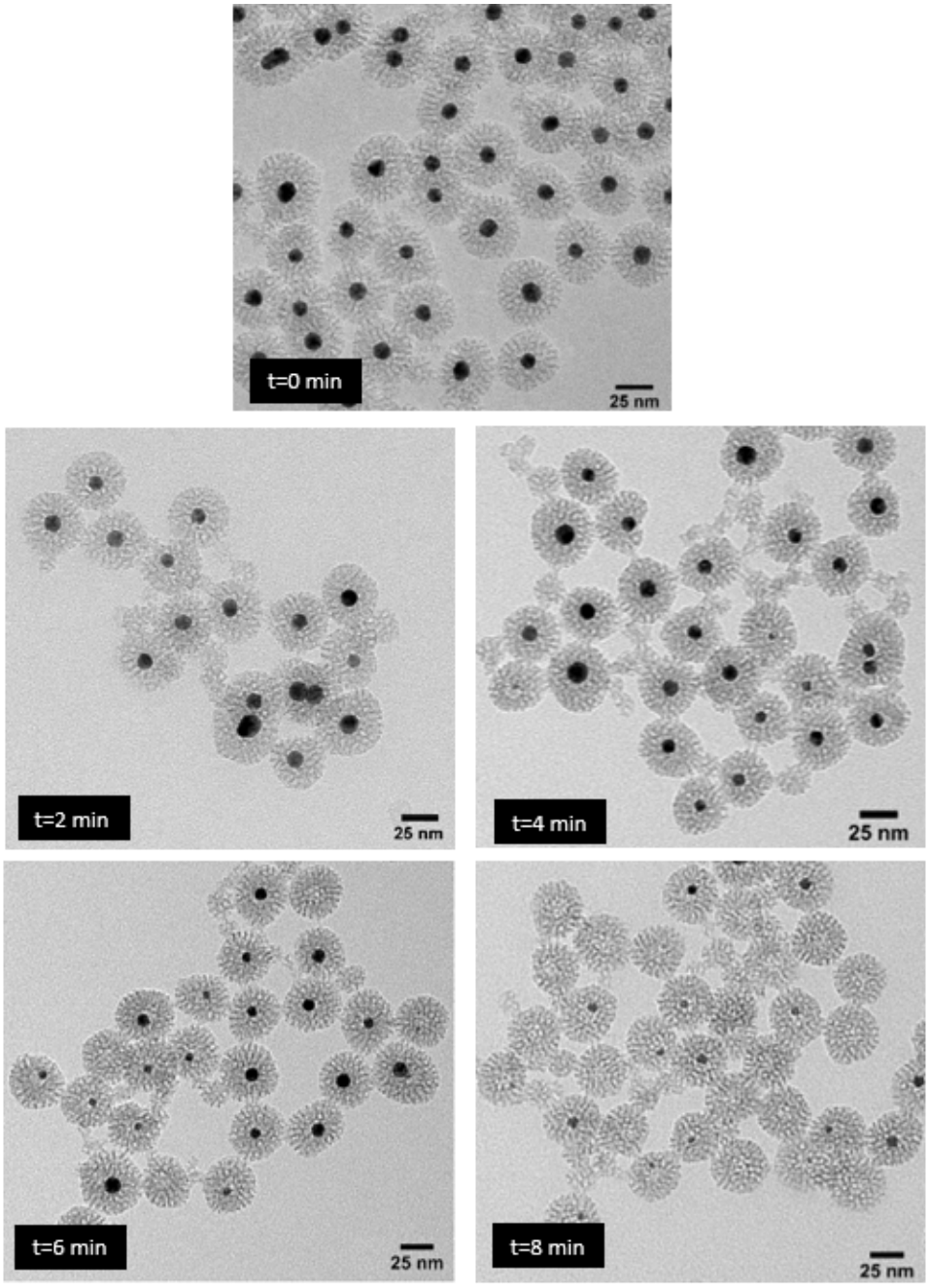

Figure 4.12: BF-TEM images of Au@SiO_2 after etching for 0, 2, 4, 6 and 8 minutes.

The Cu_xO overgrowth was performed on $Au@SiO_2$ after etching for 4 minutes (sample $AuCu_xO@SiO_2$_E4), because these NPs were significantly etched and relatively monodisperse. The overgrowth was performed through a chemical reduction with 250 μl Cu precursor, as described in section 3.3.4. The reaction was monitored with UV-VIS spectroscopy over time (figure 4.13), which showed a similar trend as the non-etched equivalent (sample $AuCu_xO@SiO_2$_250) in figure 4.10. The LSPR peak shifted from 525 nm to 587 nm within the first 60 minutes. This significant red-shift indicates the formation of large monometallic Cu-based particles. The formation of these aggregates was confirmed with BF-TEM and EDX measurements (figure 4.14). The aggregates were observed in all aliquots except for those at t = 0 min and t = 75 min, which explains the peak shift to 528 nm after 75 minutes. A similar observation was made for non-etched NPs in which the LSPR peak also blue-shifted.

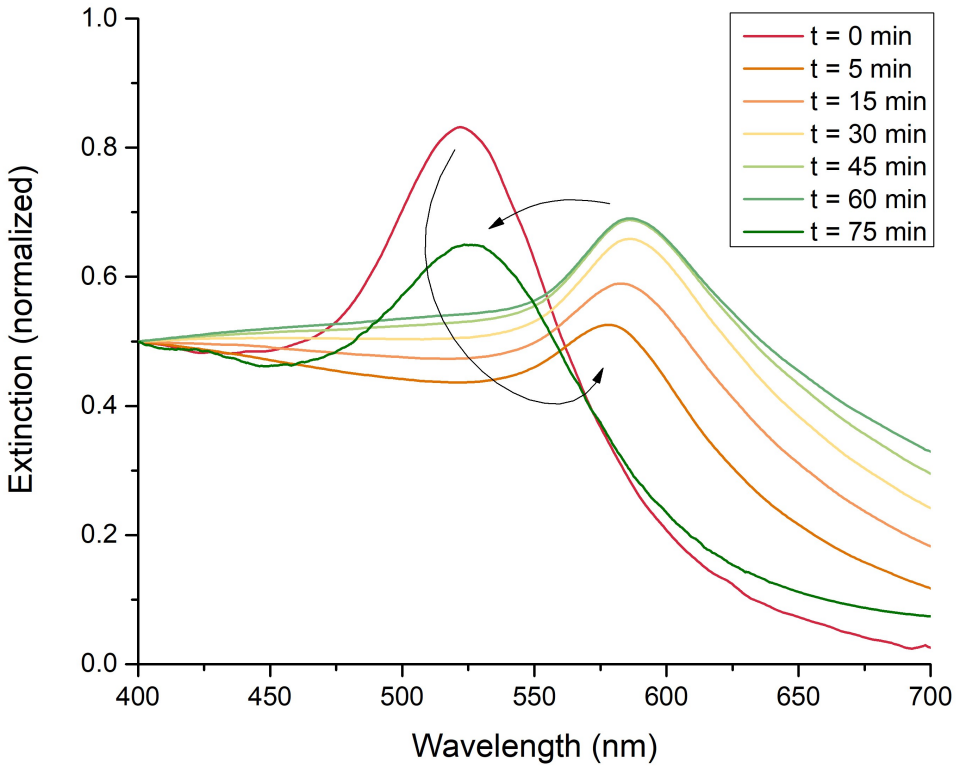

Figure 4.13: Extinction spectra of the Cu_xO overgrowth of sample $AuCu_xO@SiO_2$_E4 over reaction time, normalized at 400 nm.

The $AuCu_xO@SiO_2$_E4 sample at t = 75 min was also characterized with EDX. An average atomic Cu fraction of $10.7 \pm 1.3\%$ was determined, which is similar to the Cu content of $AuCu_xO@SiO_2$_250. These findings indicate that the increasing space between the Au

core and silica shell due to oxidative etching, did not promote the deposition of higher amounts of Cu_xO on the Au core.

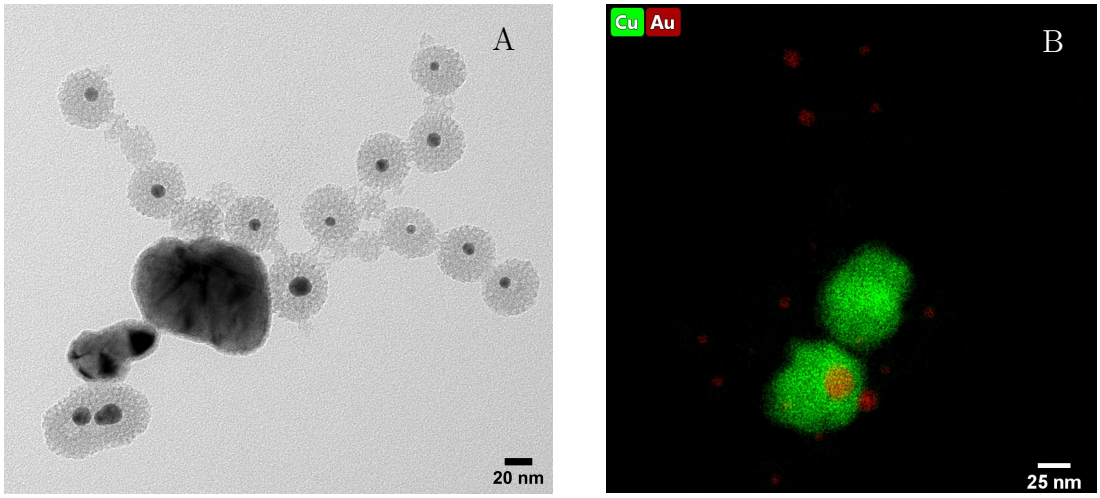

Figure 4.14: a) A BF-TEM image and b) an EDX map of $AuCu_xO@SiO_2$_E4 at t = 60 min. The black aggregates were formed during the Cu_xO overgrowth, and are composed of Cu species.

The results presented in this section demonstrated the challenge of controlling the Cu_xO overgrowth on $Au@SiO_2$ NPs. The Cu content could not be increased after increasing the amount of Cu precursor, slowing down the reaction and creating more space between the Au core and silica shell through etching. Given that higher amounts of Cu_2O overgrowth on Au NPs have been reported in the literature [39], it can be inferred that the silica shell may have limited the overgrowth. Consequently, we decided to pursue a different route for synthesizing AuCu NPs in which the metal overgrowth is performed on Au NPs without a silica shell. The results are discussed in the following section (4.3).

4.3 Synthesis route 2: Cu_2O overgrowth on ligand-stabilized Au NPs

The second route for synthesizing AuCu NPs involves the overgrowth of Cu_2O on Au NPs stabilized by PVP ligands, as reported by Liu et al. [39]. The resulting core-shell Au@Cu_2O NPs were immobilized on a silica support. This route was designed and used to achieve higher Cu fractions compared to the first synthesis route.

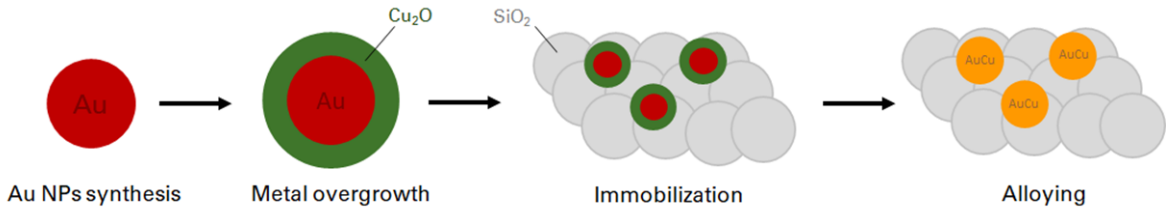

Figure 4.15: A schematic illustration of the second synthesis method for AuCu NPs. The procedure involves the sequential steps of (1) overgrowth of Cu_2O on presynthesized Au NPs, (2) immobilization of the resulting Au@Cu_2O NPs onto a silica support, and (3) thermal treatment under reducing conditions to promote alloying.

4.3.1 Characterization of Au@Cu_2O NPs

Synthesis route 2 involves the Cu_2O overgrowth on Au NPs stabilized by PVP ligands. The overgrowth was performed as outlined in section 3.4.1. A BF-TEM image of the NPs, obtained after the Cu_2O overgrowth, is presented in figure 4.16a. This image reveals the presence of a substantial shell around the Au core, indicating a high Cu content. Additionally, the NPs were characterized with selected area electron diffraction (SAED) to determine the composition of the shell structure (figure 4.16b). The lattice spacings of the ring patterns were determined from SAED and compared to literature [71, 72]. This analysis resulted in the identification of crystalline Cu_2O and Au. Thus, it can be confirmed that Au@Cu_2O NPs were synthesized. The lattice spacings with their corresponding crystal planes of Cu_2O and Au are displayed in table 4.3.

The Cu_2O overgrowth was controlled by varying the concentration of Au@PVP NPs, as previously reported by Liu et al. [39]. The concentration Au@PVP used for the overgrowth is specified for each sample, denoted with a sample ID, in table 4.4. The BF-TEM

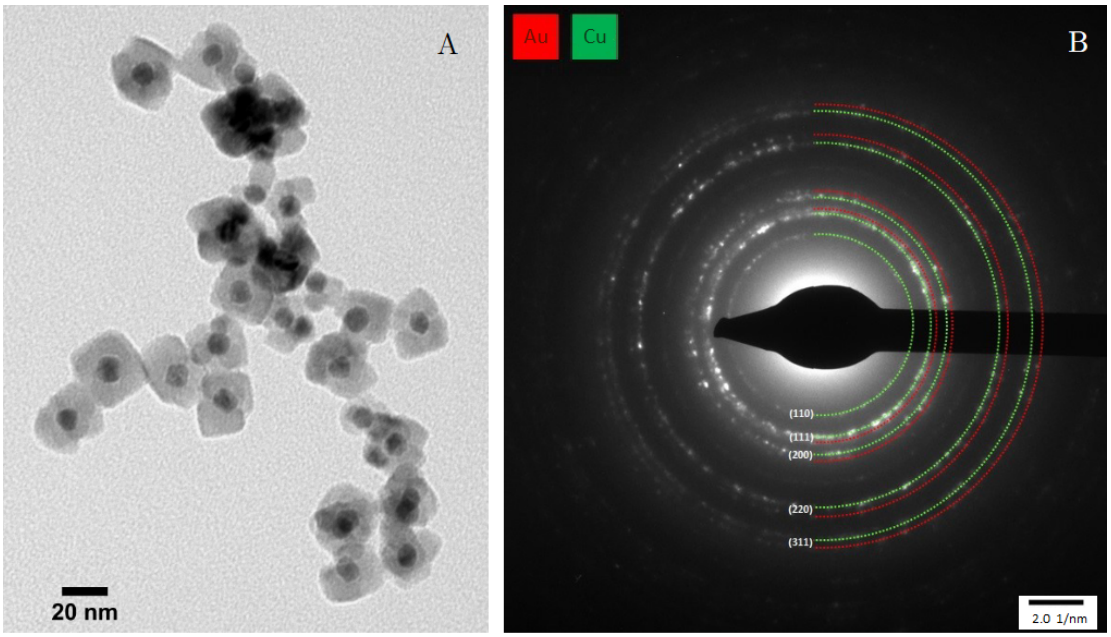

Figure 4.16: a) A BF-TEM image and b) corresponding SAED pattern of Au@Cu_2O NPs. The ring patterns are labeled with the miller indices of the corresponding lattices of Au (red) or Cu (green).

Table 4.3: The interplanar latice spacing determined from SAED with corresponding crystal planes specified by Miller indices

	calculated interplanar spacing (A)				
lattice	(110)	(111)	(200)	(220)	(311)
Au	-	2.35	2.02	1.44	1.21
Cu_2O	3.02	2.47	2.12	1.50	1.28

images presented in figure 4.17 demonstrate the decrease of the Cu_2O shell thickness with increasing Au@PVP concentration. EDX was used to verify this decline in Cu content. Noticeably, the standard deviation of metal composition increased significantly with decreasing Cu content, indicating an increased level of inhomogeneity in the overgrowth. This inhomogeneity with decreasing Cu content is also observable in the BF-TEM images in figure 4.17. For instance, it can be noticed that the shell thickness in sample Au@Cu_2O_59 significant varied between particles and within the particles itself. Additionally, the HAADF-STEM image with corresponding EDX map of Au@Cu_2O_53 in figure 4.18 shows that the thickness of the Cu_2O shell is highly polydisperse, resulting in a mixture of Au@Cu_2O NPs ranging from 35% to 75% Cu. Therefore, this Cu_2O overgrowth protocol is more suitable for obtaining Au@Cu_2O NPs a with high Cu content ($\geq$ 75%).

Table 4.4: The concentration of Au@PVP NPs used for the Cu_2O overgrowth leading to various Cu content, determined with EDX.

sample ID	concentration of Au@PVP (mmol/l)	average atomic Cu content in Au@Cu_2O NPs (%)*	LSPR peak position
Au@Cu_2O_87	0.08	87 ± 4.6	611
Au@Cu_2O_75	0.16	75 ± 12	598
Au@Cu_2O_59	0.33	59 ± 16	592
Au@Cu_2O_53	0.41	53 ± 19	578

**determined with EDX*

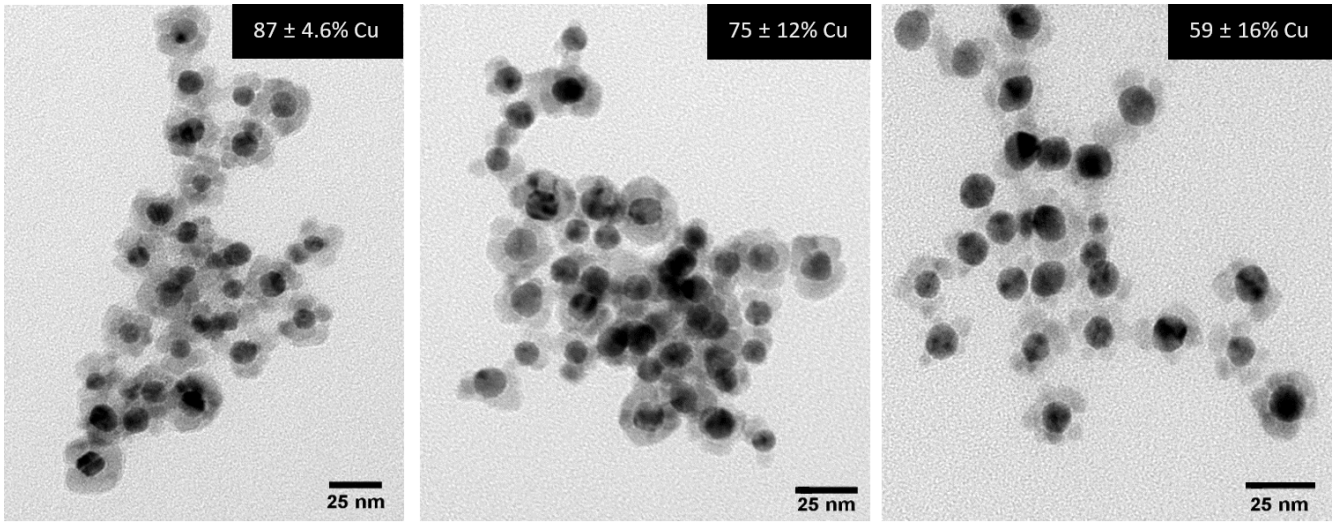

Figure 4.17: BF-TEM images of samples Au@Cu_2O_87, Au@Cu_2O_75 and Au@Cu_2O_59 in order from left to right. The atomic Cu percentages were determined with EDX.

Figure 4.19 presents the extinction spectra of the Au@Cu_2O NPs with various Cu fractions. It is evident that the LSPR peak shifted to longer wavelengths with increasing atomic Cu fraction. This red-shift was also observable during the metal overgrowth, as the color of the reaction mixture changed from red to magenta, blue and green according to different shell thicknesses. The interband transition of Cu_2O around 450 nm also became more significant with increasing Cu content [48]. The broadening of the LSPR peaks after the Cu_2O overgrowth can be attributed to an increase in polydispersity. This peak broadening is particularly pronounced for the NPs with lower Cu contents, which have been determined to exhibit a broader range in particle size and composition.

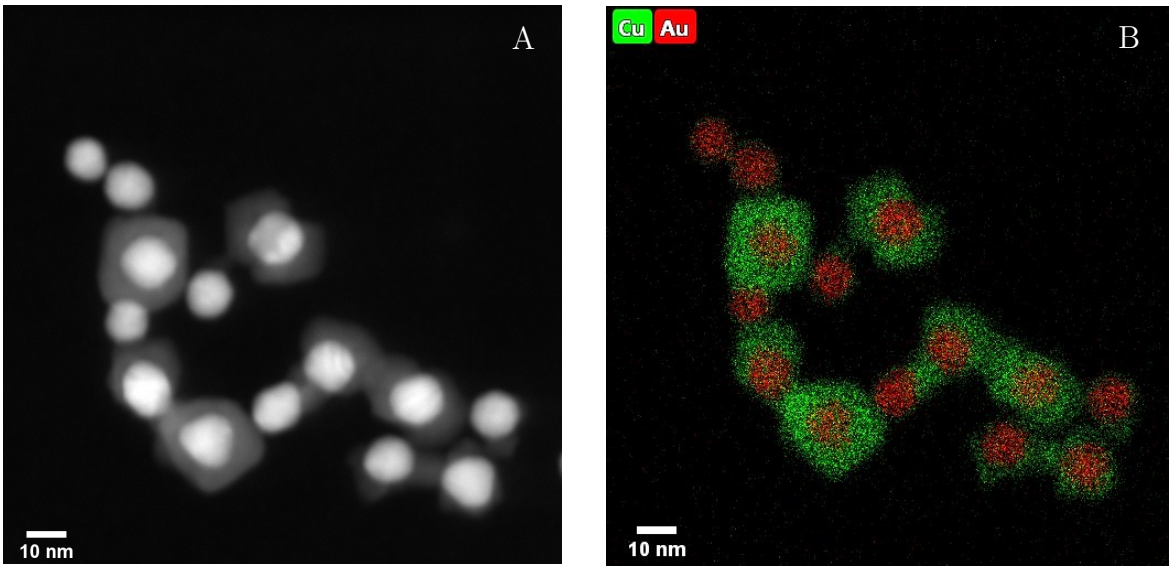

Figure 4.18: a) A HAADF-image with b) corresponding EDX map of $Au@Cu_2O$ NPs with an average Cu content of 53 ± 19 %, determined with EDX.

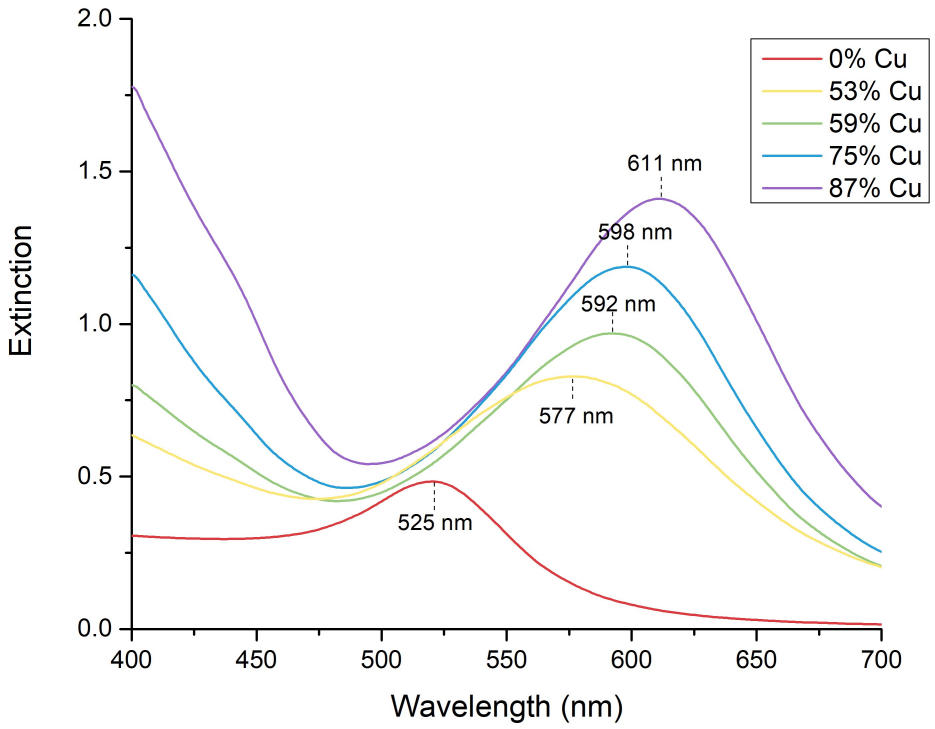

Figure 4.19: The extinction spectra of $Au@Cu_2O$ NPs with increasing atomic Cu fraction, determined with EDX.

4.3.2 Cu_2O overgrowth on $Au@SiO_2$ NPs

Section 4.2.2 demonstrated that we were not able to increase the Cu content more than approximately 11% in silica-coated NPs. Since this Cu_2O overgrowth procedure that was discussed in this section differs, we were interested to investigate if this procedure could be applied on $Au@SiO_2$. This would enable higher Cu contents, while having the advantages of the silica coating. Hence, the protocol for Cu_2O overgrowth, as described in section 3.4.1, was repeated on $Au@SiO_2$ NPs instead of Au@PVP NPs.

Two experiments were performed: one with the addition of PVP ligands, according to the protocol, and one without the addition of PVP, as the $Au@SiO_2$ NPs were already stabilized with the silica shell. An extinction spectrum and BF-TEM image of the NPs after the overgrowth are displayed in figure 4.20. The LSPR peak did not shift in the experiment without the addition of PVP, indicating that Cu_2O did not grow on the $Au@SiO_2$ NPs. However, the presence of the interband transition around 450 nm indicates that Cu_2O is present. Notable, there was no peak detected near 600 nm, as the Cu was oxidized [73]. The results from UV-VIS spectroscopy are supported with corresponding TEM images, showing that individual Cu_2O particles had formed. The extinction spectrum of the experiment with PVP addition shows a shift in the LSPR peak position to 547 nm, suggesting that Cu_2O has been deposited on the Au cores. However, its corresponding TEM image shows that Cu_2O is rather attached to $Au@SiO_2$ NPs. This could be attributed to the ability of PVP to form complexes with Cu^{2+}-ions, thereby attaching Cu_2O to the NPs [66, 74]. Altogether, these results confirm that the mesoporous silica shell around the Au NPs restricts the Cu_2O overgrowth.

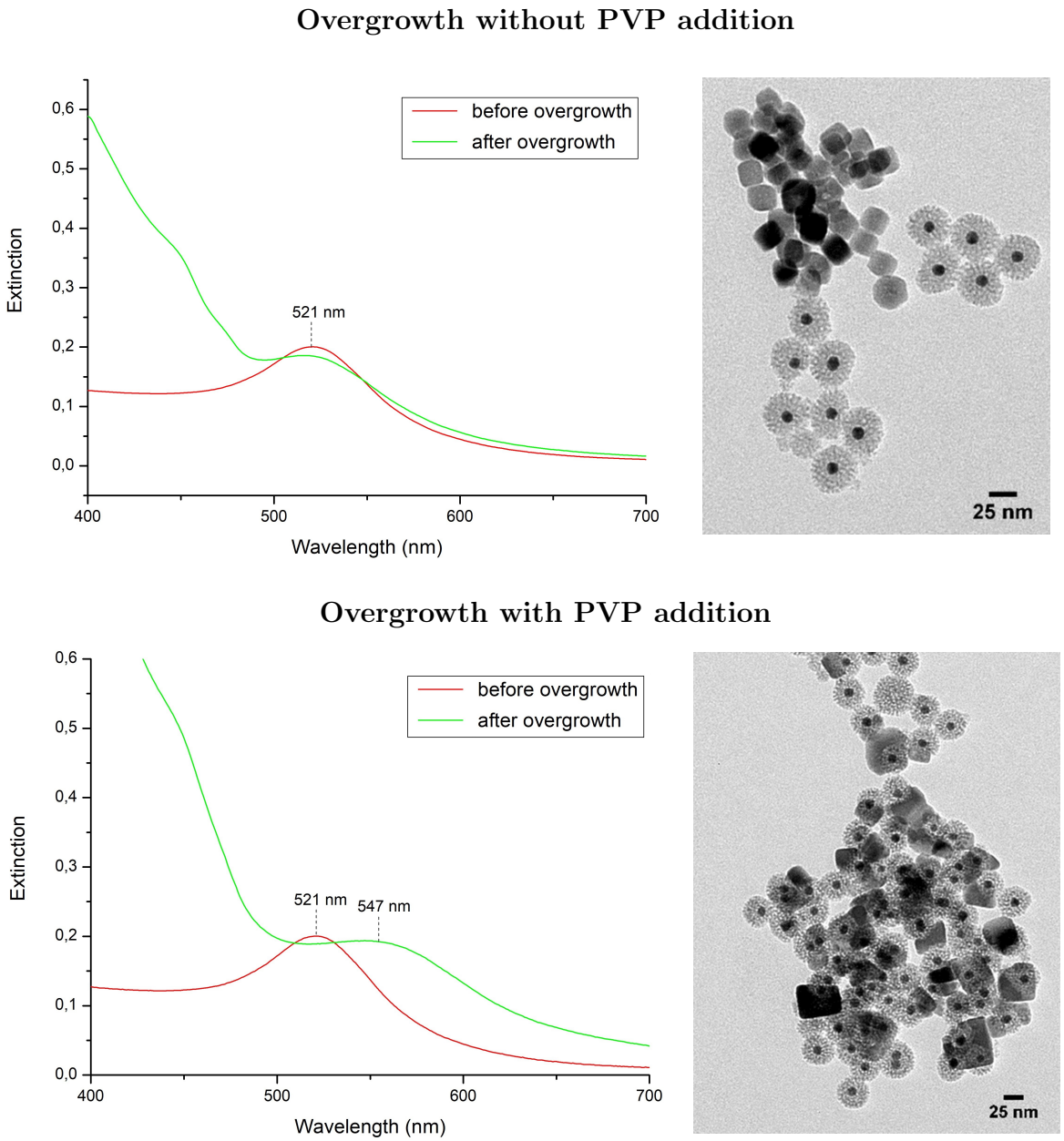

Figure 4.20: An extinction spectrum and BF-TEM image of the Au@SiO_2 NPs after the Cu_2O overgrowth without and with the addition of PVP ligands.

Since we could not achieve high Cu contents on silica-coated NPs, it was investigated if growing a mesoporous silica shell on the NPs after the Cu_2O overgrowth was possible. This would provide stability, and the resulting NPs could be compared with the NPs synthesized through route 1. Although the Au@Cu_2O NPs were stable after the ligand exchange with CTAB (figure B.4), the NPs were found to be unstable in water at 30°C for multiple hours, as the Cu_2O layer dissolved from the Au cores. Given that water is essential for CTAB to form micelles, it was concluded that growing a mesoporous silica shell on Au@Cu_2O nanoparticles was not feasible. As a result, the Au@Cu_2O NPs were directly deposited on a silica support for stabilization.

4.3.3 Immobilization of Au@Cu_2O NPs

The colloidal deposition was carried out as described in section 3.5.1, and briefly consisted on the addition of an antisolvent to a solution consisting of presynthesized Au@Cu_2O NPs and a silica support. The apolar solvent, toluene, was used as an antisolvent to lower the solubility of the NPs in solution, thereby promoting deposition on the support. The Au@Cu_2O NPs were deposited onto Aerosil 300, which is a hydrophilic fumed silica support with a specific surface area between 270 - 330 m^2/g, as specified by the manufacturer.

The colloidal deposition was performed with sample Au@Cu_2O_87 due to the homogeneous core-shell structure that was well-observable with electron microscopy. BF-TEM images of the green powder in figure 4.21 show the successful immobilization of Au@Cu_2O NPs on the silica support, but revealed clustering of NPs. This is disadvantageous, as clustering of NPs can lead to sintering upon thermal treatment. Moreover, a catalyst is generally more active when the active sites are dispersed over the surface rather than concentrated in hot spots [75].

Several parameters were adjusted to examine their impact on the clustering of the Au@Cu_2O NPs on the silica support. For instance, the deposition was repeated with Au@Cu_2O_87 stabilized with different ligands, such as citrate and CTAB, based on the hypothesis that charged ligands could exhibit a stronger interaction with the hydrophilic support. The stirring and sonication duration was also evaluated. Additionally, the impact of the addi-

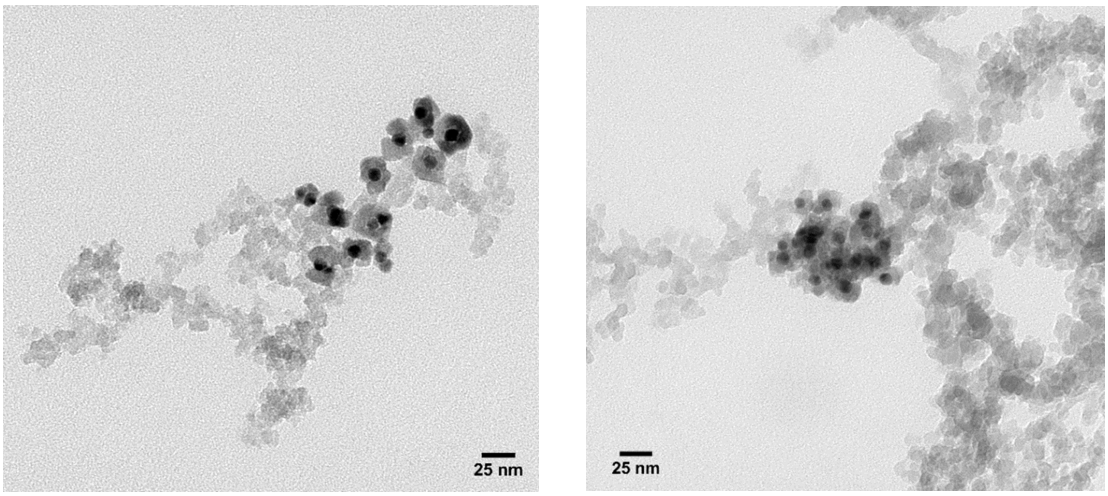

Figure 4.21: BF-TEM images of the colloidal deposition of Au@Cu_2O_87 NPs on Aerosil300, revealing clustering.

tion method (step-wise or instantaneous) and the added amount of toluene on the colloidal deposition was studied. Despite these efforts, none of the adjusted parameters resulted in a more homogeneously deposition over the silica support.

Furthermore, the effect of the solvent hydrophilicity was studied by performing the colloidal deposition in water instead of ethanol. After centrifugation, the silica support retained its white color and was separated from the colored supernatant, indicating that the NPs did not attach to the support. The effect of solvent hydrophilicity was futher investigated by including methanol as a solvent, which has a lower hydrophilicity compared to ethanol and water. This resulted in deposition of the NPs on the support, but they were still clustered.

Another adjusted parameter was the surface area of the support material. In order to study its effect on the clustering of the Au@Cu_2O NPs, the colloidal deposition was performed on Aerosil OX50. This support has larger silica particles, and therefore a lower specific surface area (35 - 65 m^2/g) compared to Aerosil300. The results in figure 4.22 show that while the NPs remained clustered, Aerosil OX50 did provide more space for them to distribute.

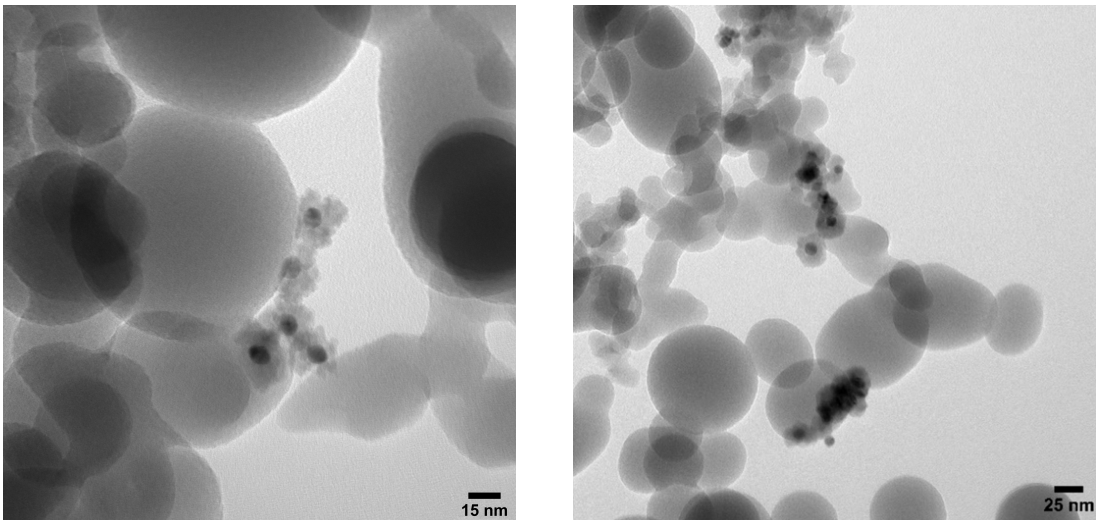

Figure 4.22: BF-TEM images of the colloidal deposition of Au@Cu_2O_87 NPs on Aerosil OX50.

Overall, the clustering of the Au@Cu_2O NPs on a silica support was not significantly affected by any of the presented modifications to the procedure. This led to the hypothesis that the Au@Cu_2O NPs were already clustered prior to their immobilization. To verify this hypothesis, the colloidal deposition was performed with monometallic Au NPs. Figure 4.23 shows a BF-TEM image of PVP-stabilized Au NPs on Aerosil OX50. The uniform deposition of the Au NPs supports that clustering of the Au@Cu_2O NPs was caused by the grown Cu_2O shell around the Au cores. As a result, a different approach was required to obtain well-dispersed supported Au@Cu_2O NPs, which is presented in section 4.4 .

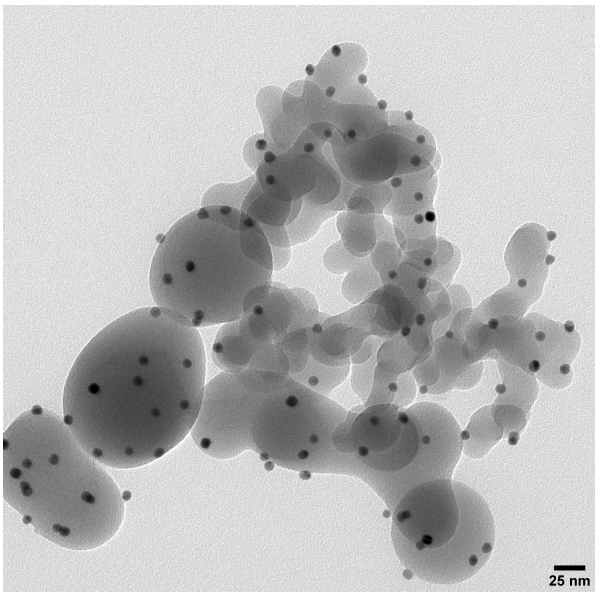

Figure 4.23: A BF-TEM image of PVP-stabilized Au NPs immobilized on Aerosil OX50.

4.4 Synthesis route 3: Cu_2O overgrowth on supported Au NPs

As the Cu_2O overgrowth on unsupported Au NPs resulted in clustering, a third synthesis method for synthesizing AuCu NPs was designed in which the overgrowth of Cu_2O was performed on supported Au NPs (figure 4.24). This route was used to achieve well-dispersed Au@Cu_2O NPs on a silica support.

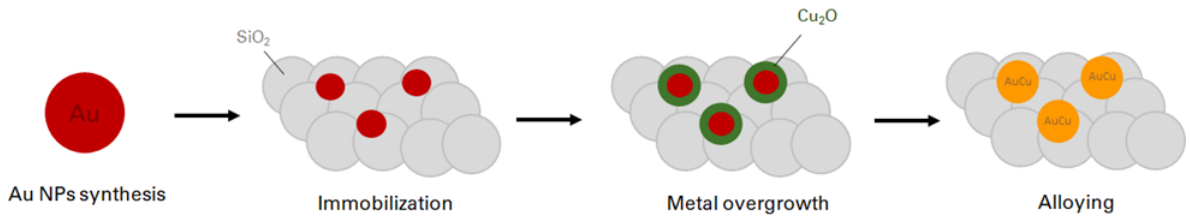

Figure 4.24: A schematic illustration of the third synthesis method for AuCu NPs. The procedure involves the sequential steps of (1) colloidal deposition of Au NPs on a silica support, (2) the overgrowth of Cu_2O on immobilized Au NPs, (3) thermal treatment under reducing conditions to promote alloying.

Since the results of the colloidal deposition of PVP-stabilized Au NPs had already been discussed in section 4.3.3, only the results of the metal overgrowth are discussed in the following section. The removal of ligands prior to catalysis will be discussed in section 4.4.2.

4.4.1 Characterization of supported Au@Cu_2O NPs

The Cu_2O overgrowth on supported Au NPs was performed as described in section 3.5.2. The result in figure 4.25a shows NPs with a core-shell structure spread out over the silica surface, indicating the formation of well-dispersed Au@Cu_2O NPs. However, the silica support also promoted heterogeneous nucleation, leading to the formation of individual Cu species (figure 4.25b). This appears to be locally, as parts of the support did not contain Cu_2O particles and some contained many, characterized with TEM.

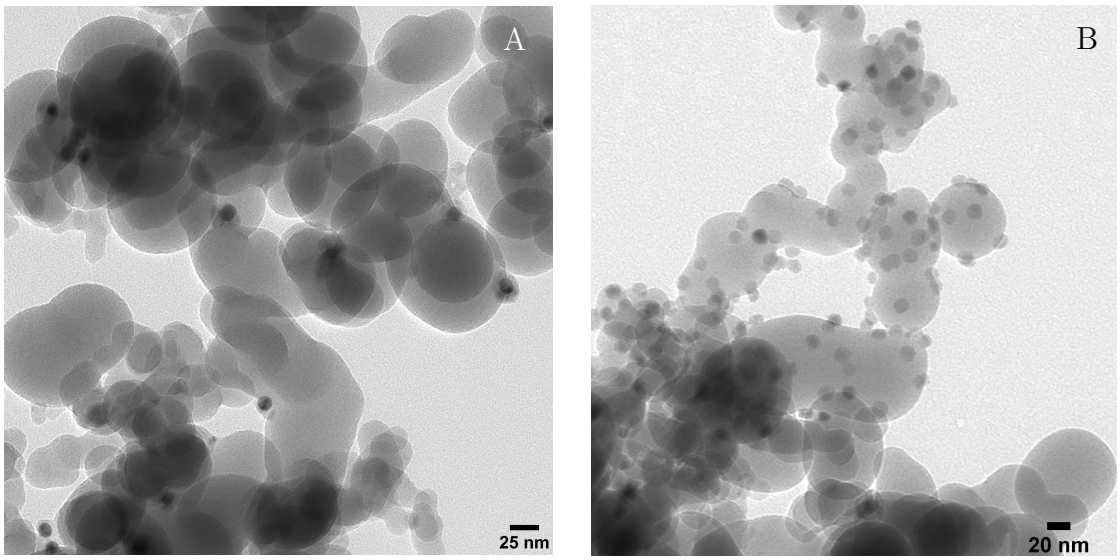

Figure 4.25: BF-TEM images showing a) Au@Cu_2O NPs on Aerosil OX50, synthesized following route 3 and b) the presence of monometallic Cu_2O NPs.

The thickness of the Cu_2O shell was varied with the amount of Cu precursor added to the reaction mixture. The resulting Au@Cu_2O NPs on Aerosil OX50, referred to as Au@Cu_2O_1 and Au@Cu_2O_2 , were synthesized with 1.0 ml and 3.0 ml 20mM $CuSO_4$, respectively. Their BF-TEM images in figure 4.26 show that the thickness of the Cu_2O shell increased with increasing amount of Cu precursor.

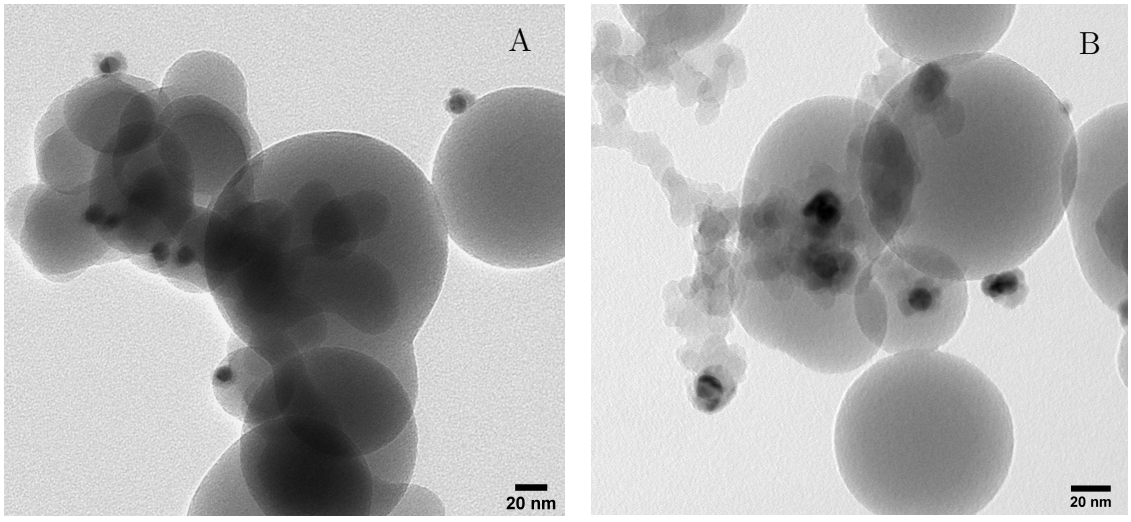

Figure 4.26: A BF-TEM image of samples a) Au@Cu_2O_1 and b) Au@Cu_2O_2

Sample Au@Cu_2O_2 was also characterized with EDX, which confirmed the formation of well-dispersed core-shell Au@Cu_2O NPs (figure 4.27). EDX also detected the presence of monometallic Cu species, demonstrated in figure 4.27a. Futhermore, figure 4.27b shows that certain NPs exhibited a thin Cu_2O shell, whereas other NPs exhibited a thicker shell.

The atomic Cu fraction of the NPs was 53±26%, where the high standard deviation points out the polydispersity. An EDX image of two core-shell NPs of sample Au@Cu_2O_1 with both approximately 38% Cu is shown in figure B.5.

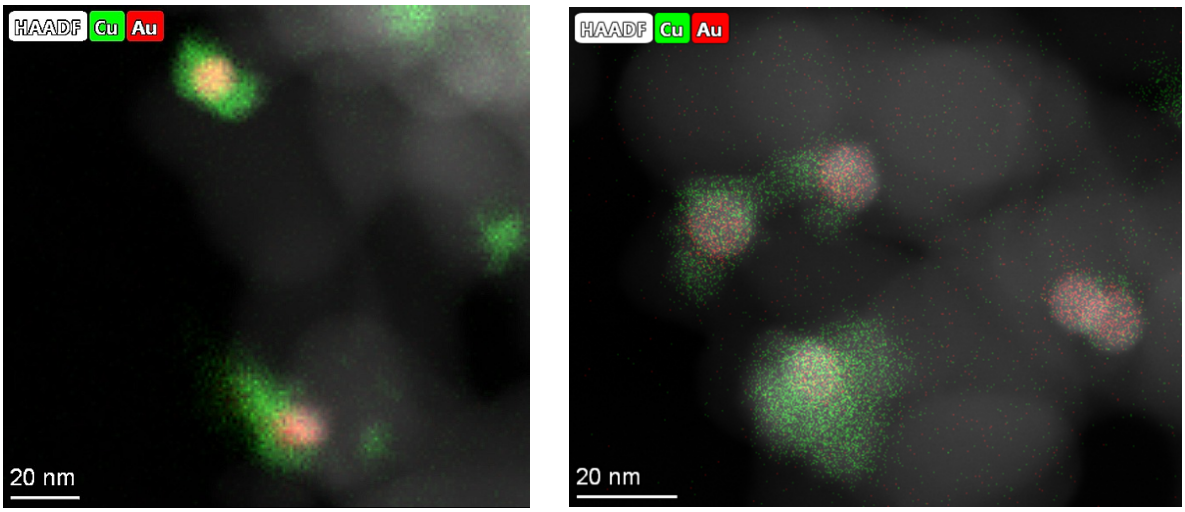

Figure 4.27: EDX maps on HAADF-STEM images of sample Au@Cu_2O_2, indicating the presence of monometallic Cu species and polydisperse Au@Cu_2O NPs.

The metal composition of Au@Cu_2O_1 and Au@Cu_2O_2 was also quantified with Inductively Coupled Plasma Atomic Emission Spectroscopy (ICP-AES). The results in table 4.5 confirm that sample Au@Cu_2O_2 has a higher Cu weight percentage compared to Au@Cu_2O_1. Remarkably, the Au content in Au@Cu_2O_1 and Au@Cu_2O_2 decreased compared to Au@aerosil. This suggests that NPs were removed from the samples during the synthesis of Au@Cu_2O_1 and Au@Cu_2O_2. The atomic Cu percentages of Au@Cu_2O_1 and Au@Cu_2O_2 were calculated from the weight percentages, which are 86% and 89%, respectively. These values significantly differ with the Cu fraction determined with EDX. It is important to note that ICP-AES is a bulk technique, and therefore does not distinguish the Cu content in the Au@Cu_2O NPs from the monometallic Cu_2O NPs in the sample. Thus, the actual atomic Cu content in the NPs themselves is lower than indicated by the ICP-AES results.

Table 4.5: The metal composition of Au@Cu_2O_1 and Au@Cu_2O_2, determined with ICP-AES.

sample ID	Au wt.%	Cu wt.%	Au : Cu ratio
Au@aerosil	0.38	n.a.	1.0 : 0.0
Au@Cu_2O_1	0.24	0.47	1.0 : 6.3
Au@Cu_2O_2	0.34	0.87	1.0 : 7.9

The x-ray powder diffraction (XRD) patterns of samples Au@aerosil, Au@Cu_2O_1 and Au@Cu_2O_2 are presented in figure 4.28. The XRD pattern of Au@aerosil exhibits diffraction peaks at 2θ angles of 44°, 52°, and 77°, corresponding to the crystal planes Au(111), Au(200) and Au(220), respectively. The diffraction peak at approximately 25° is attributed to the silica support. After the Cu_2O overgrowth, the diffraction peaks shifted to 43°, 50°, 73° and 88°, which correspond to Cu_2O(111), Cu_2O(200), Cu_2O(220) and Cu_2O(311), respectively. This result confirms that the shell on the Au cores consist of crystalline Cu_2O, as determined with SAED. The diffraction peaks of Cu_2O were more pronounced in the diffractogram of Au@Cu_2O_2 than in that of Au@Cu_2O_1, owing to its higher Cu content. Additionally, the diffraction peaks assigned to Au were shifted to higher angles, as indicated by the dashed line in figure 4.28. This shift is a result of the interaction between Au and Cu_2O, leading to a variation in lattice spacing.

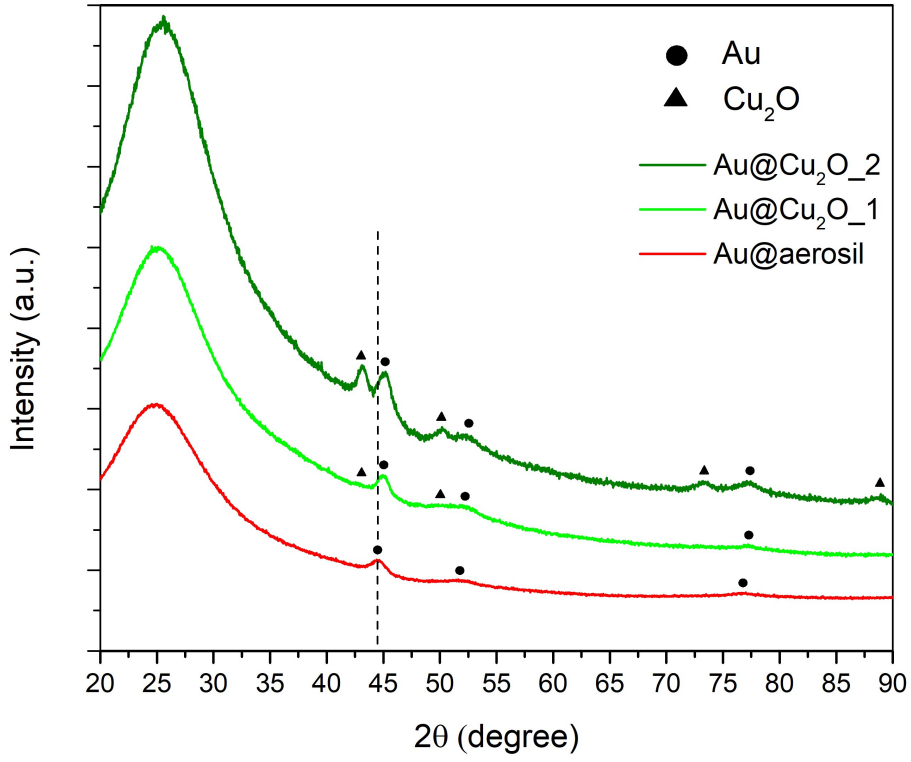

Figure 4.28: X-ray diffractogram of sample Au@aerosil (red), Au@Cu_2O_1 (light green) and Au@Cu_2O_2 (dark green). The dashed line through the Au(111) diffraction peak shows indicates its shift upon the Cu_2O overgrowth.

4.4.2 Ligand removal

The synthesis of Au@Cu_2O NPs required stablizing agents to inhibit aggregation. As a result, the supported Au@Cu_2O NPs were surrounded with PVP ligands after the metal overgrowth. However, these ligands can block the access of reactants to the active metal surface. The PVP ligands adsorbed on the metal surface are, therefore, detrimental when the NPs are used as catalysts. Consequently, it is important to remove the ligands from the metal surface prior to catalysis. It has been demonstrated that PVP ligands can be removed via thermal degradation or calcination. Typically, these treatments require high temperatures ($> 300°C$), although the removal of PVP via calcination can be achieved at lower temperatures than treatment in an inert atmosphere [76]. However, it would be efficient to combine the removal of PVP ligands with alloying of the NPs, which would require a thermal treatment under reducing atmosphere. An alternative treatment to remove PVP ligands from the Au surface has been reported in literature in which Au/TiO_2 was washed with sodium borohydride in methanol [77]. The supported metal NPs were characterized with TGA-MS and FT-IR spectroscopy to determine the most suitable treatment for the removal of PVP ligands.

TGA-MS analysis

Thermogravimetric analysis combined with mass spectroscopy (TGA-MS) was used on supported Au NPs to determine the conditions at which the PVP ligands are removed. To examine if the treatment with sodium borohydride (BH) can be employed for Au NPs on a SiO_2 support, TGA was performed with and without the treatment, respectively referred to as Au@aerosil_BH and Au@aerosil. The treatment with BH was performed according to the protocol by Donoeva et al. [77]. The TGA results in an atmosphere of 20% O_2/Ar and 5% H_2/Ar are shown in figure 4.29.

The TGA plot shows that the weight of both samples are relatively unstable between 30°C - 50°C due to the removal of volatile compounds. Analysis of MS data at $m/z = 18$ shows that water was removed in this temperature range under 20% O_2/Ar, resulting in a relatively small weight loss (figure B.6). On the contrary, the MS signal for water

significantly increased under a 5% H_2/Ar flow, indicating the formation of water during the thermal treatment. Water could have been formed during the reduction of Cu_2O and decomposition of PVP.

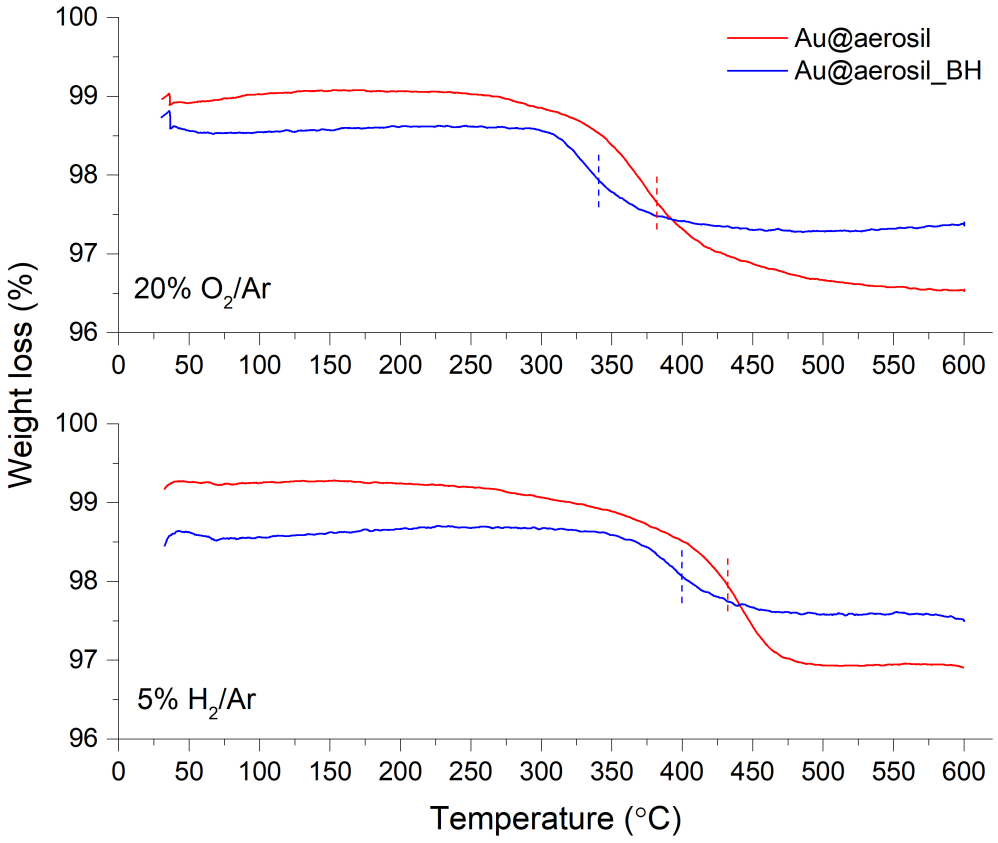

Figure 4.29: TGA plot of sample Au@aerosil before and after treatment with sodium borohydride (BH) in 20% O_2/Ar and 5% H_2/Ar. The dashed lines represent the temperature at which half of the weight loss due to PVP removal is detected.

Above 50°C, the weight is relative stable until PVP is removed, resulting in a significant weight loss. Figure 4.29 shows that this weight loss due to the removal of PVP started at lower temperatures under 20% O_2/Ar in comparison with 5% H_2/Ar. This was expected, as oxygen facilitates the oxidation, and thereby decomposition of PVP [78]. The temperature range in which PVP was removed is determined with the derivative of the TGA plot, and detailed in table 4.6. The results obtained in an oxidative atmosphere is in accordance with the MS signal for CO_2 (figure 4.30). As CO_2 is formed when PVP is decomposed, its MS signal can be used to determine when PVP is removed. Figure 4.30 also shows that less CO_2 is detected for Au@aerosil_BH than Au@aerosil, suggesting that

less PVP ligands where present to be removed after the treatment. This result is also evident in the TGA plots in figure 4.29, as the relative weight loss for Au@aerosil_BH was significantly less compared to untreated Au@aerosil. Thus, the treatment with BH on silica-supported Au NPs had removed part of the PVP ligands. This is in accordance with previous research, which showed that a substantial amount of PVP was still present in titania-supported Au NPs, but resided exclusively on the support [77].

Table 4.6: The estimated temperature range in which PVP is removed based on the derivative of the TGA plot.

	atmosphere	
sample ID	20% O_2/Ar	5% H_2/Ar
Au@aerosil	270°C - 500°C	300°C - 480°C
Au@aerosil_BH	300°C - 400°C	370°C - 450°C

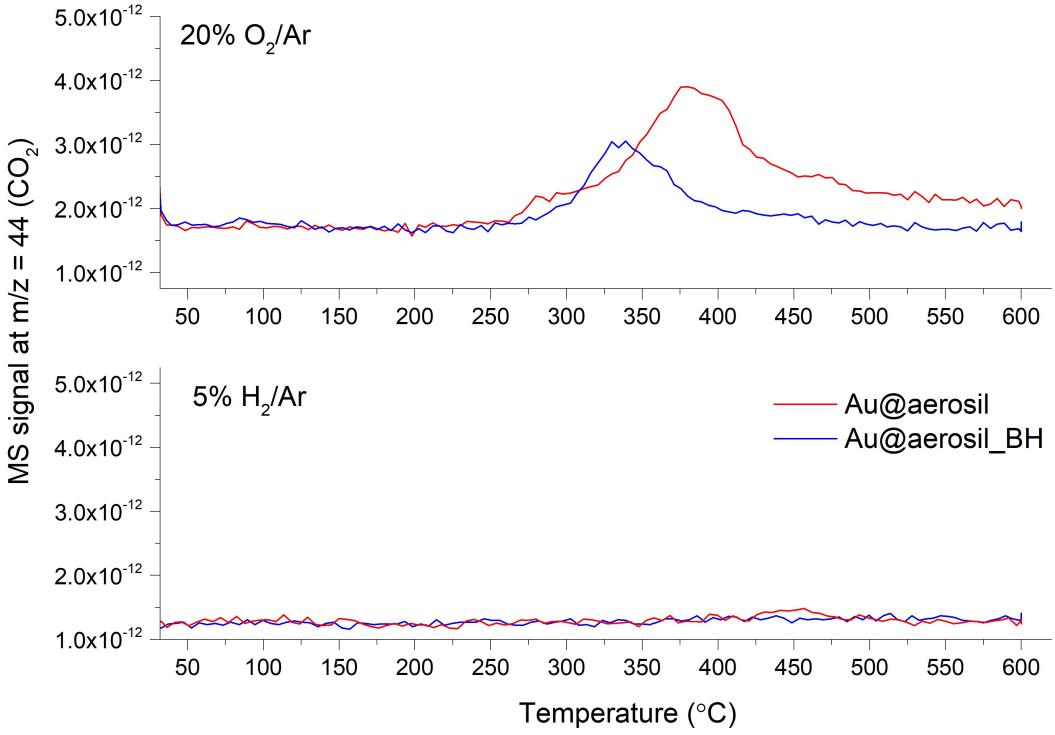

Figure 4.30: Mass spectrometry (MS) data showing the intensity for CO_2 ($m/z = 44$) of sample Au@aerosil before and after treatment with sodium borohydride (BH) in 5% H_2/Ar and 20% O_2/Ar. The CO_2 signal under 5% H_2/Ar is relatively zero, since no O_2 is present to oxidize PVP to form CO_2.

FT-IR spectroscopy analysis

Next to TGA-MS, Fourier transform-infrared (FT-IR) spectroscopy can also be used to determine the removal of PVP. Due to its organic structure, PVP exhibits characteristic peaks in the infrared region, which can be measured with FT-IR spectroscopy. The FT-IR spectra of Au@aerosil and Au@aerosil_BH are shown in figure 4.31. The peaks at 2157 cm^{-1}, 1072 cm^{-1}, 806 cm^{-1} and 457 cm^{-1} correspond to the silica support (figure B.8). Both samples exhibited peaks at 2956 cm^{-1}, 1663 cm^{-1} and 1462 cm^{-1} corresponding to C−H stretching, C=O stretching and C−H bending vibrations, respectively [79]. These peaks, which can be assigned to PVP, were less present in Au@aerosil_BH than in Au@aerosil. Additionally, the band around 3437 cm^{-1} of Au@aerosil can be assigned to water, but also to a O−H stretching vibration in PVP (figure B.8). As a result, FT-IR spectroscopy confirms that the treatment on Au/SiO_2 with BH leads to partial PVP removal.

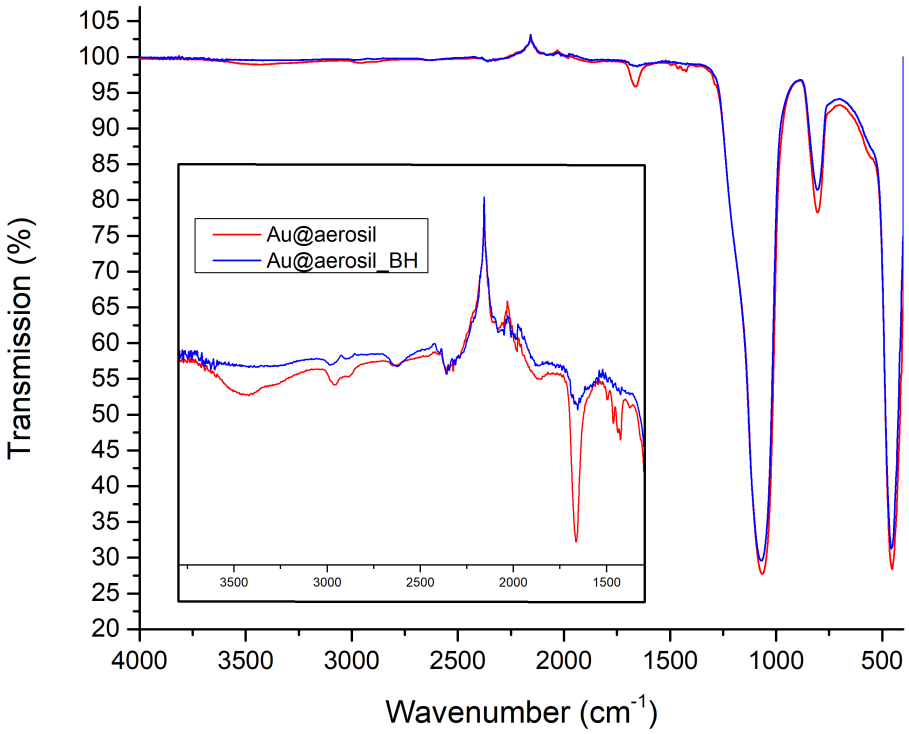

Figure 4.31: FT-IR spectra of sample Au@aerosil before and after treatment with sodium borohydride (BH).

Table 4.6 and figure 4.29 show that treating supported Au NPs with BH reduced the

temperature required to remove the PVP ligands. Therefore, this treatment was also performed on supported Au@Cu_2O NPs. Unfortunately, the color of the reaction mixture changed from blue to purple during the treatment, suggesting that Cu_2O was partially removed from the Au cores. As the Au@Cu_2O NPs did not appear stable upon the treatment with BH, a temperature up to 500°C was required to remove PVP, according to the TGA results.

Figure 4.31 demonstrated that FT-IR spectroscopy can be employed to determine the removal of PVP ligands. Therefore, sample Au@Cu_2O_2 was characterized with FT-IR before and after a thermal treatment at 500°C. The Au@Cu_2O NPs were heated under both 10% H_2/N_2 and 10% O_2/N_2. The results in figure 4.32 show that the C=O stretching vibration at 1663 cm^{-1} was less significant after the thermal treatments, indicating that PVP had been removed. This is supported by a TGA measurement of Au@Cu_2O_2 after thermal treatment at 500°C in 10% H_2/N_2, showing no significant weight loss (figure B.7).

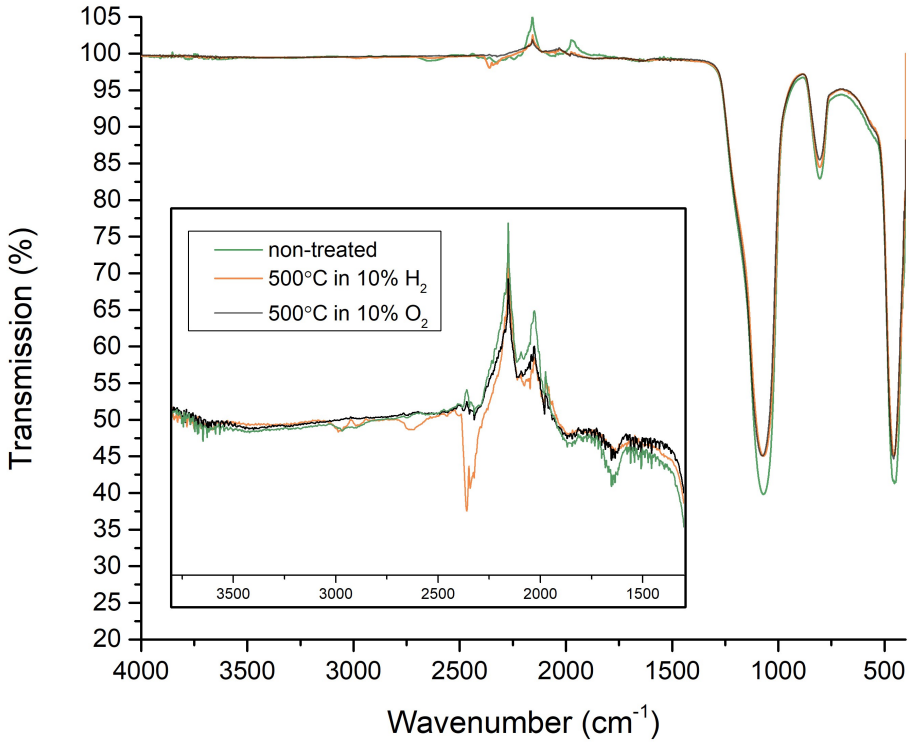

Figure 4.32: FT-IR spectra of sample Au@Cu_2O_2 before and after heat-treatment at 500°C under 10% H_2/N_2 and 10% O_2/N_2.

Noticeably, the peak at 1663 cm^{-1} in sample Au@Cu_2O_2 was already less pronounced in

comparison with Au@aerosil. This suggests that some PVP was already removed after the Cu_2O overgrowth, which can be attributed to the extra washing step. The peak at 2375 cm^{-1} in figure 4.32 after heating in 10% H_2 could correspond to the reduction of Cu_2O to metallic Cu [80]

Calcination of sample Au@Cu_2O_2

A BF-TEM and HAADF-STEM image of sample Au@Cu_2O_2 after its calcination at 500°C in 10% O_2/N_2 is presented in figure 4.33, showing that the core-shell structure retained after the treatment. In this case, the Cu_2O shell cannot be reduced to metallic Cu under oxidative conditions, and the oxidized Cu does not mix with Au. This result shows that the PVP ligands can be removed, while maintaining the core-shell structure through calcination.

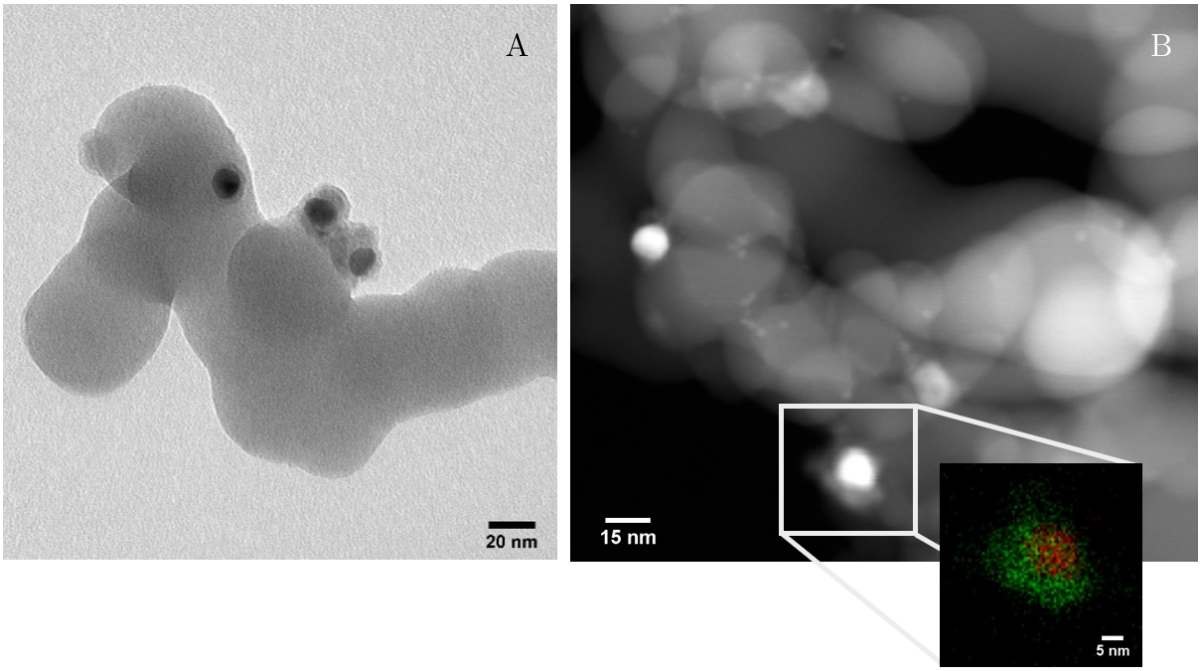

Figure 4.33: a) A BF-TEM image and b) HAADF-STEM image with EDX map of Au@Cu_2O_2 after a thermal treatment at 500°C in 10% O_2/N_2. The green and red pixels represent Au and Cu, respectively. The small dots on the silica support in the HAADF-STEM image correspond to oxidized Cu particles.

Further characterization of sample Au@Cu_2O_2 after its thermal reduction at 500°C in 10% H_2/N_2 (referred to as sample Au@Cu_2) is discussed in section 4.5.3.

4.5 Alloying

The final step of the three synthesis routes involves the thermal treatment of the core-shell Au@Cu_xO NPs in a reducing atmosphere to obtain alloyed AuCu NPs. The results are discussed in the following section, which are divided for each synthesis route.

4.5.1 Synthesis route 1: Au@Cu_xO@SiO_2

The results discussed in section 3.3.4 demonstrated that core-shell Au@Cu_xO NPs, stabilized with a mesoporous silica shell, can be obtained via synthesis route 1. In order to determine the temperature required for mixing the Au and Cu atoms, the Au@Cu_xO NPs were heated at 100°C, 200°C and 300°C in 10% H_2/Ar. Figure 4.34 presents the EDX maps of sample $AuCu_xO@SiO_2$_250 after the thermal reduction at 200°C and 300°C. The metal redistribution from a core-shell structure to a mixed phase was difficult to observe due to the small particle size. Hence, the intensity of the Au and Cu signal within the NPs were mapped in RGB plots to gain a better understanding of the metal distribution. The RGB plot of a NP heated at 200°C shows that the Cu signal was more extended compared to the Au signal, indicating a core-shell structure. In contrast, the RGB plot of a NP heated at 300°C shows an equivalent extension of the Cu and Au signals, indicating an alloyed structure. Thus, these results demonstrate that the Au and Cu atoms were mixed between temperatures of 200°C and 300°C under a 10% H_2/Ar atmosphere.

The atomic Cu fraction of $AuCu_xO@SiO_2$_250 was determined before and after the thermal treatment in 10% H_2/Ar from EDX maps. The results, displayed in table 4.7, show that the Cu content remained similar after a thermal reduction at 100°C, compared to its untreated counterpart. However, the Cu content significantly increased upon thermal reduction at 200°C and 300°C. This suggests that Cu_xO was present outside of the NPs and had been able to migrate to the Au core. It is possible that some Cu_xO had been stuck in the silica shell after the metal overgrowth and was therefore not removed during the washing steps. The migration of Cu could have been initiated by the reduction of oxidized Cu to metallic Cu between 100°C and 200°C, thereby enhancing the interaction with the Au core. Mixing of the metals, Au and Cu, between 200°C and 300°C might

have further driven this migration. Temperature-programmed reduction (TPR) analysis of $AuCu_xO@SiO_2$_250 are necessary to determine the reduction temperature of Cu_xO, which would provide greater insight into the migration of Cu under these conditions.

Table 4.7: The average Cu content of sample $AuCu_xO@SiO_2$_250 after various thermal treatments under a 10% H_2/Ar flow, determined from EDX.

thermal treatment	average atomic Cu percentage (%)
non-treated	11.4 ± 1.6
100°C	12.5 ± 2.4
200°C	17.0 ± 2.6
300°C	21.3 ± 4.4

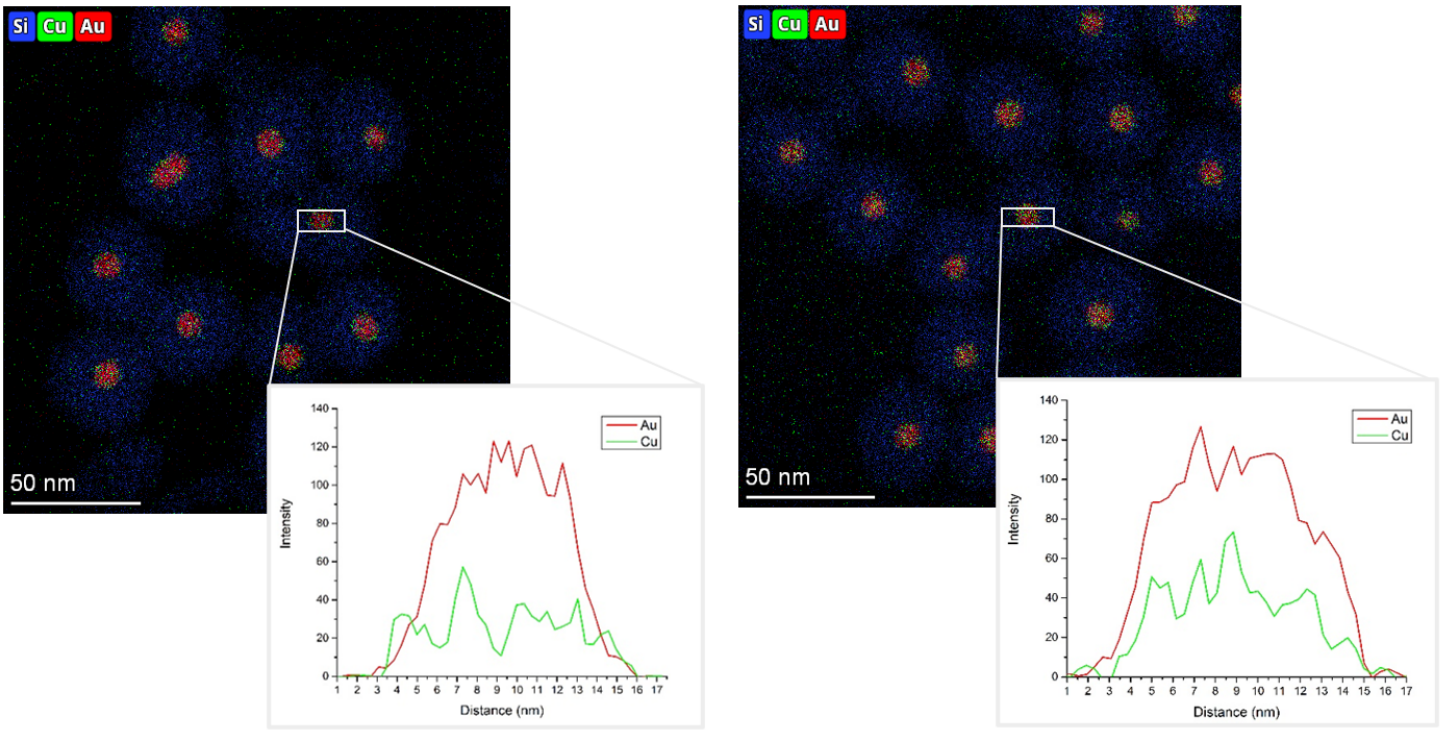

Figure 4.34: EDX maps with corresponding RGB plot of $AuCu_xO@SiO_2$_250 after thermal reduction in 10% H_2/Ar at a) 200°C and b) 300°C.

Furthermore, the effect of thermal treatment on etched $Au@Cu_xO$ NPs was studied by reducing sample $AuCu_xO@SiO_2$_E4 at 300°C. The average Cu content was found to be $28.3 \pm 2.3\%$ using EDX, which is significantly higher compared to the non-etched equivalent, which contained $21.3 \pm 4.4\%$ Cu. This is noteworthy, as the untreated etched and non-etched $AuCu_xO@SiO_2$ NPs contained a similar Cu content (as described in section 4.2.2). Altogheter, these results indicate that the atomic Cu fraction of $AuCu_xO@SiO_2$ NPs can be adjusted via oxidative etching after thermal reduction.

4.5.2 Synthesis route 2: Au@Cu_2O

The results in section 4.3 demonstrated that core-shell Au@Cu_2O NPs with an average Cu content ranging from $53\% - 87\%$ could be obtained via synthesis route 2. In order to investigate the impact of the shell thickness on the temperature required for alloying, a similar experiment was performed in which Au@Cu_2O NPs were reduced at various temperatures. Since the colloidal deposition of Au@Cu_2O NPs on a silica support resulted in clustering (as discussed in section 4.3.3), the NPs were heated with and without support.

BF-TEM images of sample Au@Cu_2O_87 after thermal treatment at 200°C and 300°C in 10% H_2/Ar are presented in figure 4.35. The transition from a core-shell to an alloyed structure between 200°C and 300°C is evident for both supported and unsupported Au@Cu_2O NPs. The unsupported NPs exhibited aggregation during the alloying process, indicated by the presence of significantly large particles. On the other hand, the supported NPs appeared to be less aggregated, and therefore more monodisperse. This results shows that the NPs were more stable on a support during the thermal treatment. In contrast with unsupported NPs, individual particles of several nm were observed after the treatment of supported NPs, indicating the presence of monometallic Cu particles. The structural reformations of core-shell Au@Cu_2O NPs is further studied in the following in-situ experiment.

To gain more insight in the metal distribution of the Au@Cu_2O NPs, an in-situ TEM heating experiment was performed, using unsupported sample Au@Cu_2O_87. The NPs were heated from 150°C to 400°C in increments of 50°C under a 10% H_2/Ar flow. The results are presented in figure 4.36 through HAADF-STEM images of the NPs, taken with a 10 minute time interval at each temperature. Figure 4.36 shows that the core-shell structure of the NPs disappeared around 300°C, marking the temperature necessary to form AuCu NPs. This is in accordance with previous findings that suggested an alloying temperature between 200°C-300°C. The reformation and sintering appeared to occur at earlier stages, resulting in aggregation as the temperature increased. It can be noticed that part of the shell structure split from the NPs at 200°C, which became more pronounced at higher temperatures. This could explain the observation of individual Cu NPs in the supported

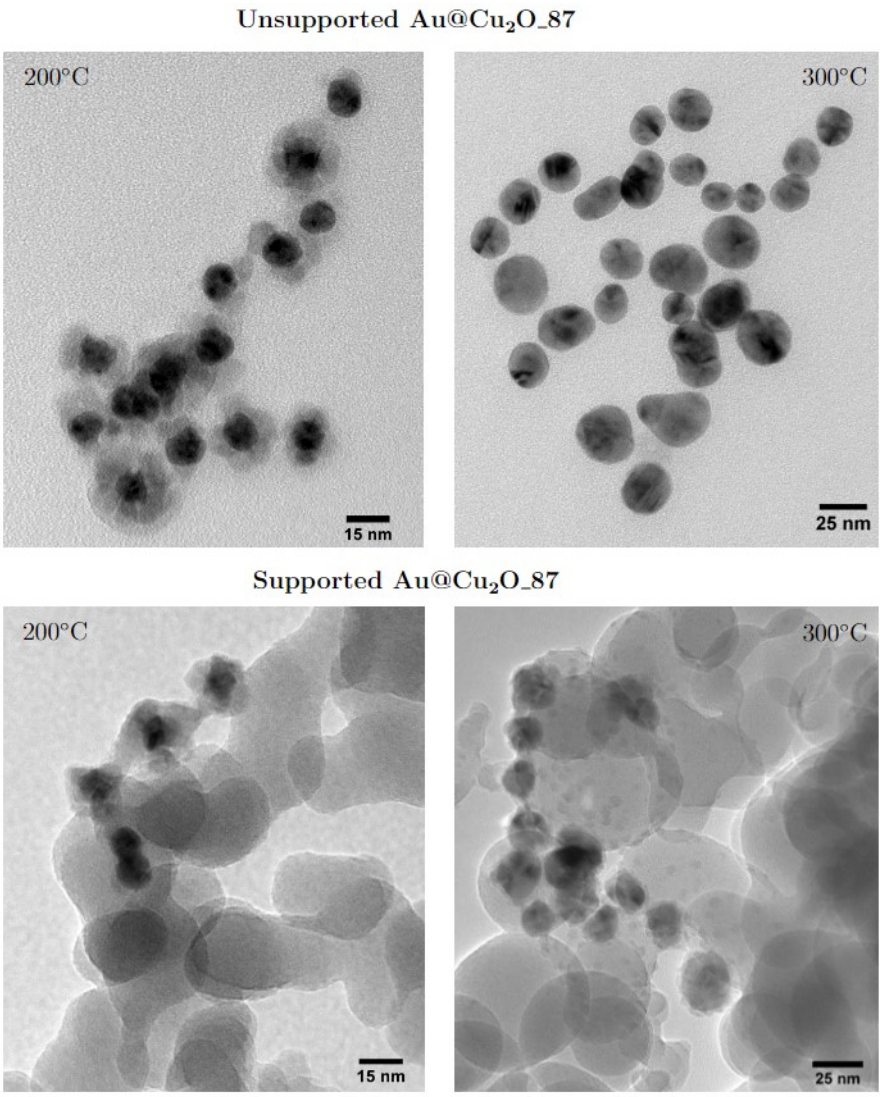

Figure 4.35: BF-TEM images of sample Au@Cu_2O_87 after thermal treatment at 200°C or 300°C under a 10% H_2/Ar flow. Note that the images correspond to the same sample, but not to exactly the same NPs.

NPs after thermal reduction in figure 4.35. In contrast to the unsupported sample, the Cu NPs that were formed during the thermal reduction, were able to attach to the silica support, which could explain that the Cu NPs were observed for supported AuCu NPs, but not in unsupported ones.

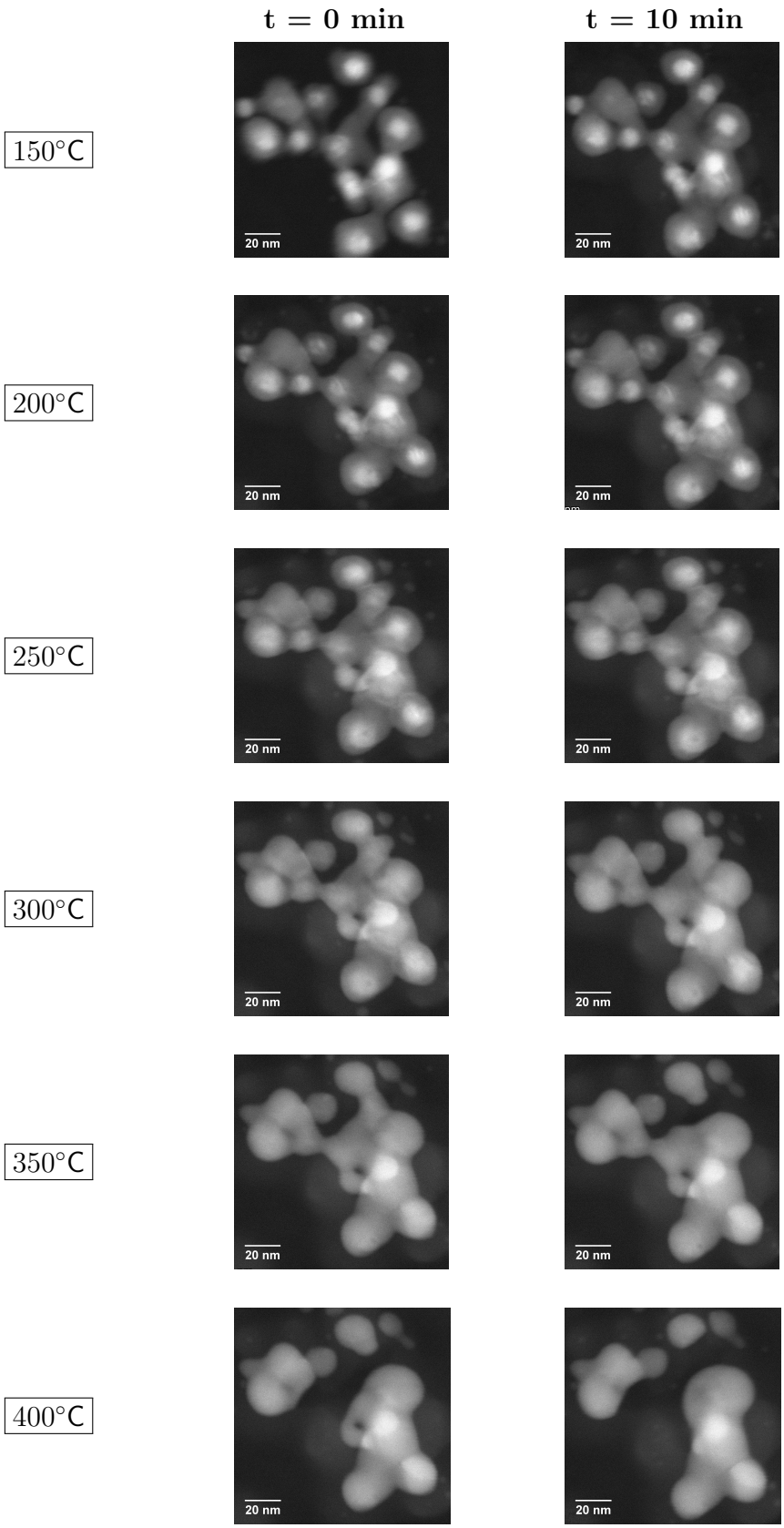

Figure 4.36: HAADF-STEM images of $Au@Cu_2O\_87$ recorded during in-situ heating under a 10% H_2/Ar flow.

4.5.3 Synthesis route 3: supported Au@Cu_2O

It has been demonstrated in section 4.4 that the Cu_2O overgrowth via route 3 resulted in well-dispered Au@Cu_2O NPs over a silica surface. This homogeneous distribution should make the NPs less prone to sintering, leading to more stable NPs. As a result, the NPs could be interesting for catalytic purposes.

As the treatment with BH could not be carried out without altering the Au@Cu_2O NPs, as discussed in section 4.4.2, a thermal treatment was required to remove the PVP ligands. Although, a temperature of 300°C would have been sufficient to form AuCu NPs (section 4.5.2), TGA-MS analysis revealed that a temperature of 500°C was required to fully remove the PVP ligands. As ligand removal is a crucial step prior to catalytic testing, the Au@Cu_2O NPs, synthesized via route 3, were heated to 500°C instead of 300°C. This was performed under reducing conditions to alloy the Au@Cu_2O NPs together with the ligand removal.

A BF-TEM image of sample Au@Cu_2O_2 after treatment at 500°C in 10% H_2/N_2 (referred to as sample Au@Cu_2) in figure 4.37a shows that the NPs remained distributed over the silica surface after the ligands were removed. A thin layer with low Z-contrast was observed around many of the AuCu NPs, suggesting that a shell of oxidized Cu might have formed, as a result of exposure to air after the treatment (figure 4.37b). This was also observed in figure 4.35, showing supported NPs of sample Au@Cu_2O_87 after the thermal treatment at 300°C in 10% H_2/Ar. This is consistent with previous studies reporting phase segregation in AuCu particles under oxidative conditions [14].

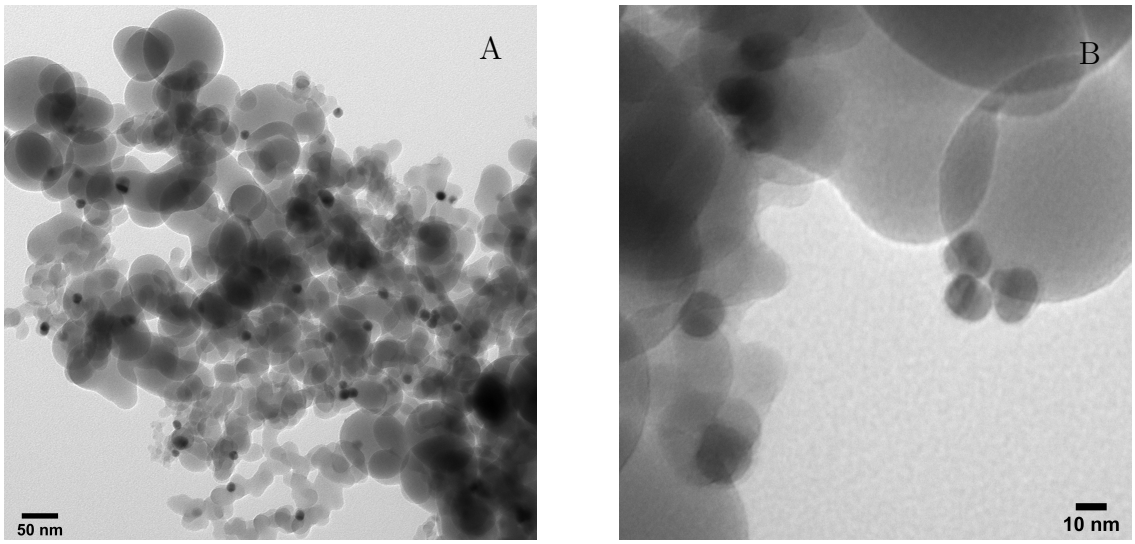

Figure 4.37: BF-TEM images of sample Au@Cu_2O_2 heated at 500°C under 10% H_2/N_2 (sample Au@Cu_2) with an average particle size of 15.8 ± 2.36 nm.

The metal composition of samples Au@Cu_1 and Au@Cu_2

XRD Powder XRD was used to study sample Au@Cu_2. Figure 4.38 shows that the diffraction peaks shifted compared to the untreated sample (Au@Cu_2O_2 in figure 4.28) due to the reduction of Cu_2O and mixing of the Au and Cu atoms. The diffraction peaks at 49° and 59° could correspond to references $Au_{0.32}Cu_{0.68}$ and $Au_{0.25}Cu_{0.75}$, as depicted in figure 4.38. The diffraction peak at 46° could represent CuO, which can be formed due to air exposure, but then a peak around 42° would also be expected [81]. However, it could be possible that this peak is hidden in the background of the silica peak at 26°. Monometallic Cu-based peaks should be in the diffractogram, as it was observed in BF-TEM images. However, the weight percentage could be too low, resulting in a peak too weak to be apparent. The oxidized Cu layer around the NPs could also be amorphous. Alternatively, the peak at 46° could correspond to AuCu NPs with a lower Cu content, such as reference $Au_{0.25}Cu_{0.75}$. This would indicate an inhomogeneous Cu_2O overgrowth, leading to AuCu NPs with different compositions.

The peaks in the XRD pattern for sample Au@Cu_1 (Au@Cu_2O_1 after thermal treatment at 300°C in 10% H_2/N_2) were less significantly shifted, indicating a lower Cu content in the AuCu NPs (figure 4.38). The peaks around 46° and 53° could correspond to reference $Au_{0.25}Cu_{0.75}$. Overall, the resuls obtained with XRD indicate that the AuCu NPs in sample Au@Cu_1 have a lower average Cu content than the AuCu NPs in Au@Cu_2.

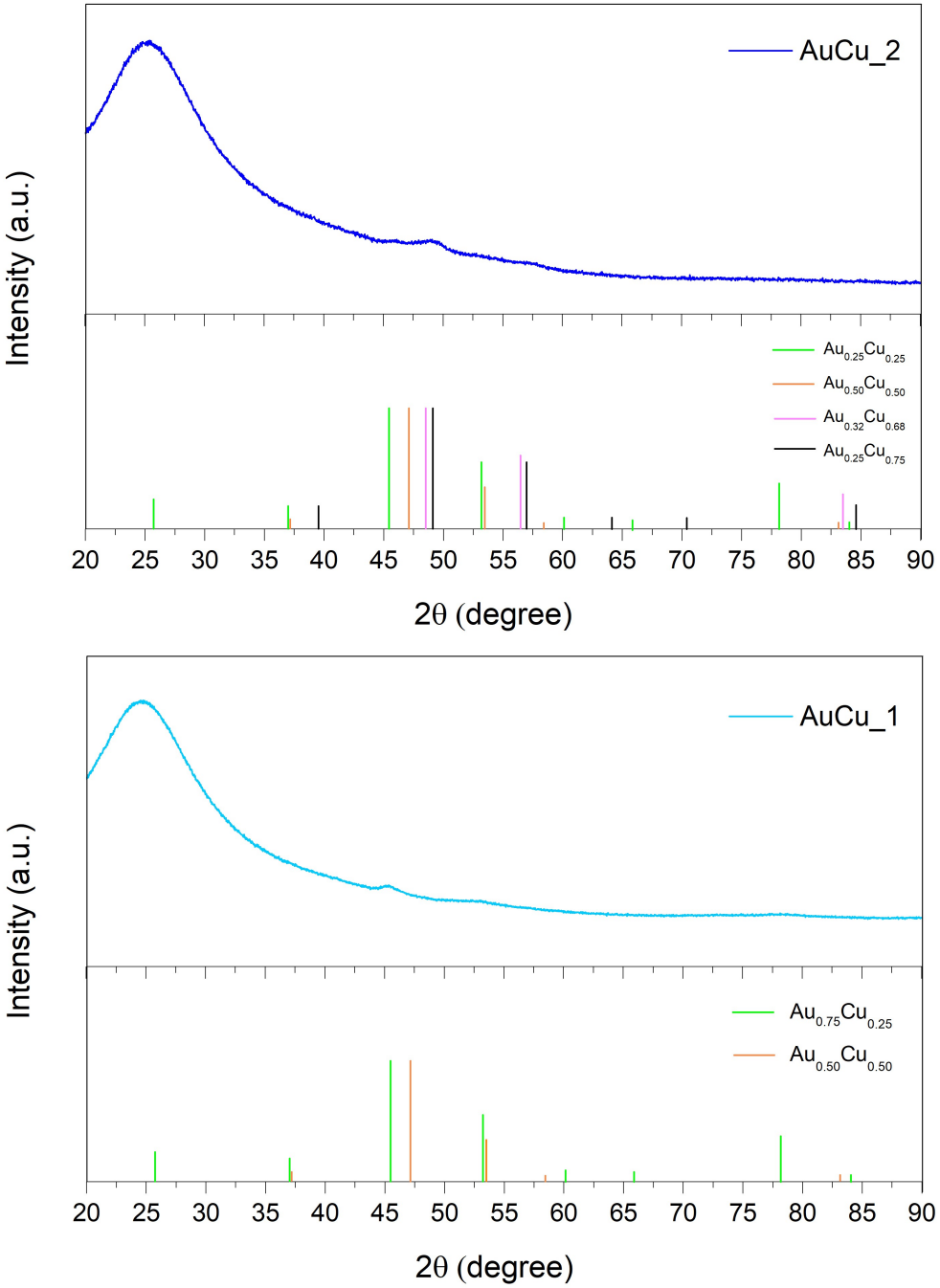

Figure 4.38: XRD profiles of Au@Cu_2 and Au@Cu_1 with references of $Au_{0.75}Cu_{0.25}$ (No. 01-071-5023), $Au_{0.50}Cu_{0.50}$ (No. 00-025-1220), $Au_{0.32}Cu_{0.68}$ (No. 04-006-2799) and $Au_{0.25}Cu_{0.75}$ (No. 00-035-1357) from The International Centre for Diffraction Data [81, 82, 83].

BF-TEM The metal composition of samples Au@Cu_1 and Au@Cu_2 was calculated based on the average particle size, determined with BF-TEM (table 4.8). The average particle size of Au@Cu_1 was determined to be 14.7 ± 1.4 nm, while that of Au@Cu_2 was found to be 15.8 ± 2.4 nm. These particle sizes corresponded to a Cu content of $47 \pm 16\%$ and $59 \pm 25\%$, respectively.

EDX The metal composition was also determined with EDX (table 4.8). The atomic Cu fraction of the AuCu NPs in Au@Cu_1 and Au@Cu_2 was $34 \pm 10\%$ and $53 \pm 31\%$, respectively. Notably, the average Cu content of $Au@Cu_2O$_2 and Au@Cu_2 were both determined to be approximately 53%, which suggests that the metal composition of the NPs remains similar after thermal reduction. However, the metal composition of Au@Cu_1 and Au@Cu_2 was based on EDX measurements of six particles each, which makes the accuracy of the values uncertain. The determined Cu content of $53 \pm 31\%$ with EDX is inconsistent with the XRD profile of Au@Cu_2, but it has to be noted that this is an average value. On the other hand, a Cu content of $34 \pm 9.5\%$ of sample Au@Cu_1 would fit its XRD profile (figure 4.38).

Table 4.8: The atomic Cu percentages of AuCu NPs in Au@Cu_1 and Au@Cu_2, determined with the average particles size according to BF-TEM and with EDX.

	atomic fraction of Cu (%)	
	BF-TEM	EDX
Au@Cu_1	47 ± 16	34 ± 10
Au@Cu_2	59 ± 25	53 ± 31

Overall, the exact metal composition of Au@Cu_1 and Au@Cu_2 is unclear due to the presence of monometallic Cu species and the inhomogeneous Cu_2O overgrowth. However, the results of BF-TEM, EDX, ICP-AES and XRD show that the Cu content of the AuCu NPs in sample Au@Cu_2 is higher than in sample Au@Cu_1.

4.6 Catalytic tests

The catalytic properties of AuCu NPs with various metal compositions, as synthesized in synthesis route 3, were tested for the oxidation of CO to CO_2 in the presence of excess O_2. Samples Au@Cu_1 and Au@Cu_2, which contained supported, alloyed AuCu NPs and their monometallic counterpart, sample Au@aerosil, were tested. It is important to note that Au@Cu_2 had a higher Cu content than Au@Cu_1 (section 4.5.3). As the particle size differed for each sample, the metal surface area was corrected with the amount of sample loaded in the reactor (detailed in section 3.7). The catalytic activity was determined from the decline of CO concentration, using gas chromatography (GC).

The catalytic tests briefly consisted of a pretreatment at 300°C under a 10% H_2/Ar flow to reduce the re-oxidized Cu after air exposure. Subsequently, the samples were tested in 1% CO and 10% O_2, while step-wise heating from 50°C to 300°C in increments of 50°C. The temperature was kept constant for an hour. The cooling down proceeded with the same, reversed temperature profile as heating up.

4.6.1 Metal composition

Figure 4.39 shows the CO conversion against the reaction temperature for samples Au@Cu_1, Au@Cu_2 and Au@aerosil. The figure demonstrates that the catalytic activity was dependent on the temperature. The AuCu NPs showed little CO conversion until the temperature approached 200°C. The activity increased further upon heating to 300°C, where Au@Cu_2 even reached full conversion. This result is in accordance to literature, as it has been reported that AuCu NPs show little activity for CO oxidation, until a phase segregation is caused by the oxidation of Cu between 150°C and 240°C [14, 84].

This increase in catalytic activity for the supported AuCu NPs is in contrast with the supported Au NPs, which showed little CO conversion throughout the entire test. As a result, the catalytic activity of AuCu NPs significantly exceeded the Au NPs between 200°C and 300°C. The turnover frequency (TOF) values at 200°C and 250°C were also significantly larger for bimetallic AuCu NPs than monometallic Au NPs (table 4.9). However, it can

not be concluded that the activity of AuCu NPs was enhanced due to synergistic effects, since monometallic Cu NPs were not tested.

The calculated TOF values of the NPs could unfortunately not be compared to literature, as the metal loading, metal composition and particle size significantly differed [85]. However, a similar conclusion that bimetallic AuCu NPs were more active for CO oxidation than monometallic Au NPs has been drawn in literature [85].

Figure 4.39 shows that the CO conversion of sample Au@Cu_2 was generally higher than for sample Au@Cu_1. A similar trend can be observed for the TOF values in table 4.9. These results suggest that the catalytic activity of AuCu NPs increases with Cu content for CO oxidation.

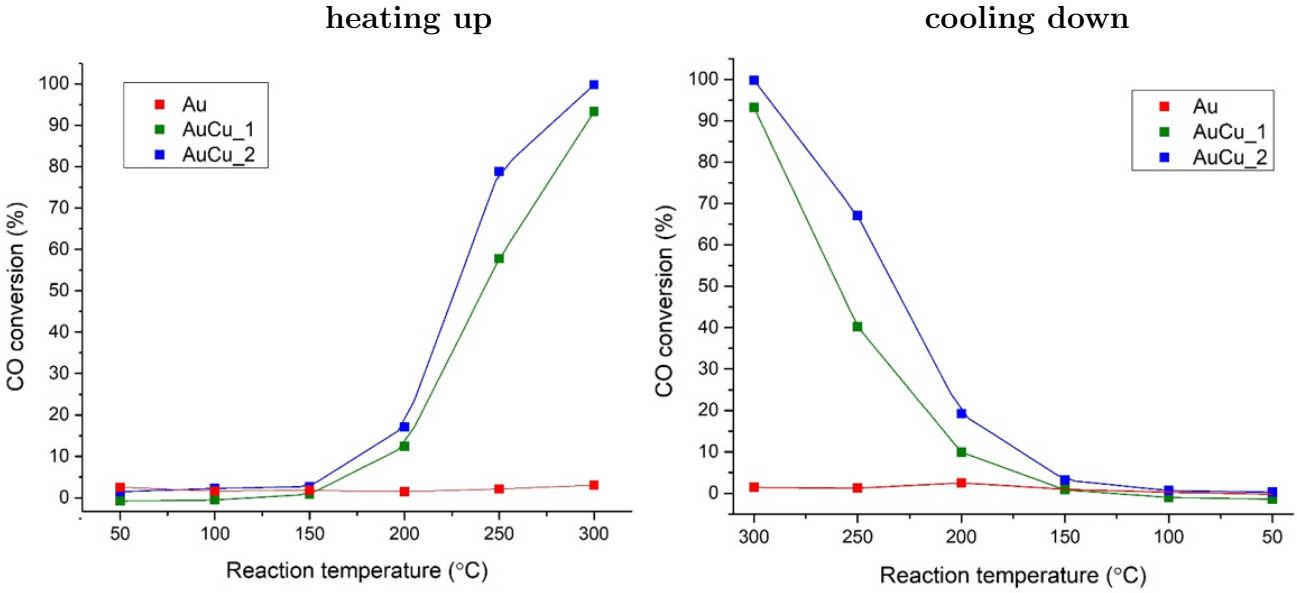

Figure 4.39: The CO conversion plotted against the reaction temperature for samples Au@aerosil (Au), Au@Cu_1 and Au@Cu_2

Table 4.9: The turn-over frequency (TOF) of the catalysts at 200°C and 250°C during heating up and cooling down. TOF is defined as turnover frequency in terms of converted CO molecules per metal surface atom per second.

	heating up		**cooling down**	
sample ID	TOF @200°C (s^{-1})	TOF @250°C (s^{-1})	TOF @250°C (s^{-1})	TOF @200°C (s^{-1})
Au@aerosil	0.00	0.01	0.01	0.02
Au@Cu_1	0.11	0.47	0.34	0.09
Au@Cu_2	0.13	0.56	0.47	0.14
Au@Cu_2_O_2	0.00	0.01	0.02	0.01

The CO conversion over reaction time for the different samples is presented in figure 4.40. This figure shows that the activity-vs-temperature curves for the AuCu NPs are not superimposable for heating and cooling, indicating deactivation of the catalysts. In particular, the CO conversion at 250°C was significantly higher upon heating up than cooling down. This trend is also evident in the TOF values, presented in table 4.9. Additionally, the activity of sample Au@Cu_1 appeared to be unstable at 300°C. The structural changes in the NPs due to oxidation of Cu during the reaction could have resulted in the deactivation of the catalysts. A BF-TEM image of Au@Cu_2 after the catalytic test shows that the structure had been rearranged in a core-shell structure, indicating the segregation of AuCu NPs to $AuCu_xO$ heterostructures (figure 4.41). Further investigation into the rearrangement of the metals during the catalytic reaction can be conducted through in-situ TEM heating experiments under a 1% CO/10% O_2 gas flow.

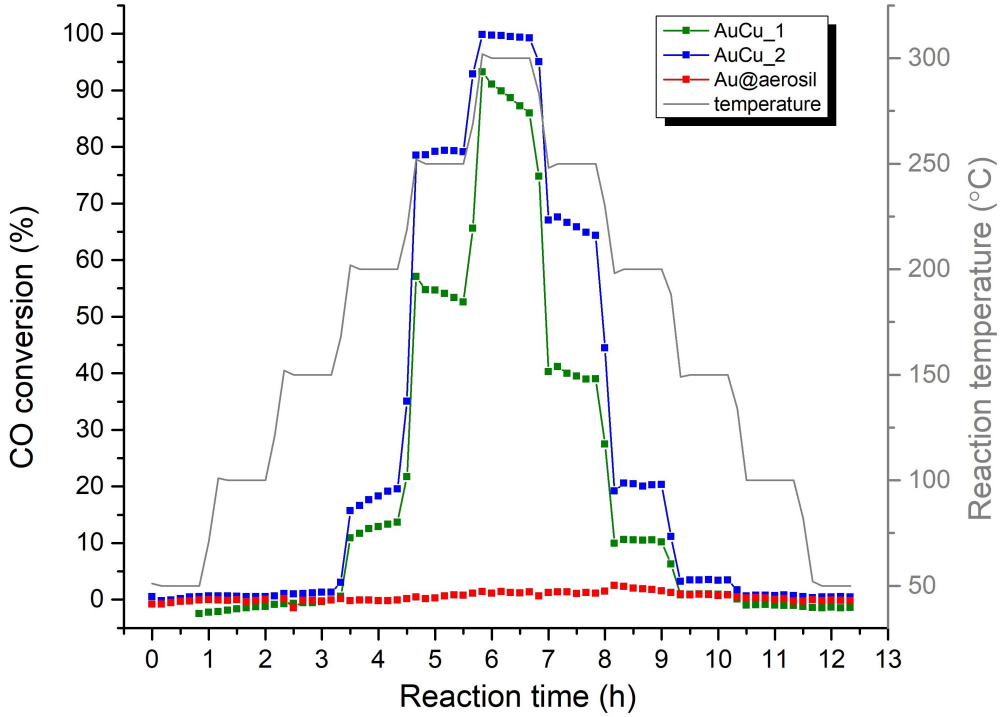

Figure 4.40: The temperature-dependent CO conversion as a function of reaction time for samples Au@Cu_1, Au@Cu_2 and Au@aerosil. The temperature profile is plotted as a gray line (right-axis), The CO conversion reached value below 0% and above 100% due to small errors in the catalytic test and data collection (e.g. small variations in gas flow, error in GC peak area integration).

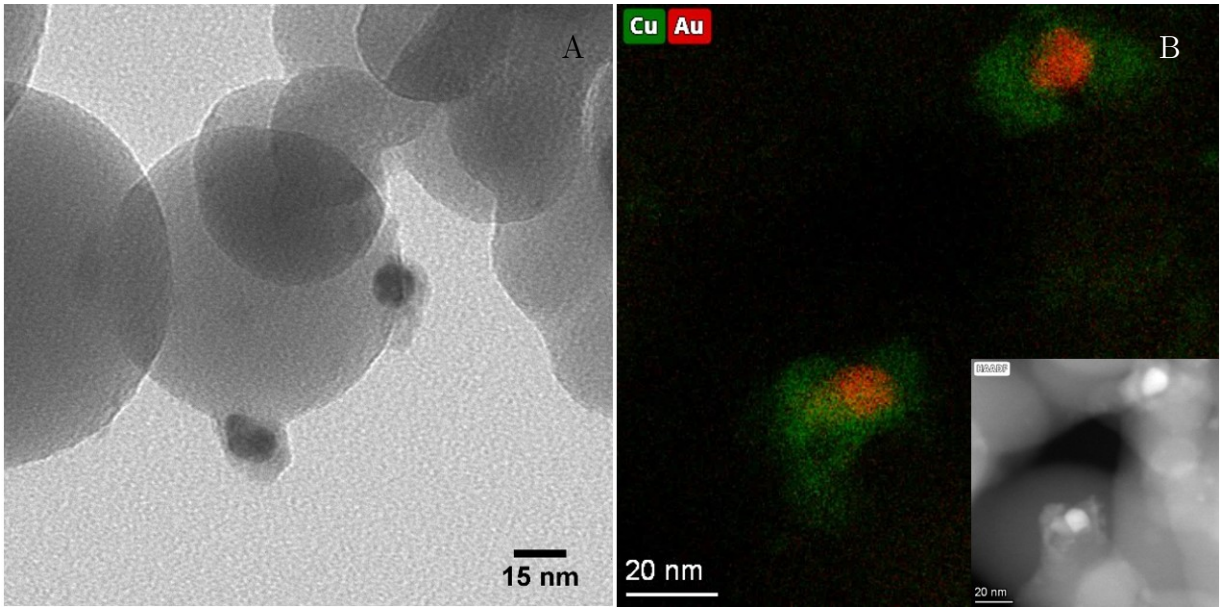

Figure 4.41: a) A BF-TEM image and b) EDX map with corresponding HAADF-STEM image of Au@Cu_2 after the catalytic test in CO oxidation.

4.6.2 Metal distribution

In general, synergistic effects are heavily dependent on the metal distribution in bimetallic NPs [6]. It would, therefore, be interesting to test different structures of AuCu NPs to gain more insight in the influence of the metal distribution on the catalytic activity in CO oxidation. It has been demonstrated in section 4.4.2 that the removal of PVP ligands could be carried out at 500°C in a reducing and oxidative atmosphere, resulting in different distribution of the metals. The treatment in 10% H_2 resulted in alloyed AuCu NPs, whereas the treatment in 10% O_2 retained the core-shell structure (figure 4.33). The effect of these different metal distributions on the catalytic activity were studied by comparing sample Au@Cu_2O_2 after its ligand removal in 10% H_2/N_2 (previously referred to as Au@Cu_2) and 10% O_2/N_2. It is important to note that the oxidized Cu shell acts as the active side in the core-shell NPs, as Au is not exposed to the surface.

The results in figure 4.42 show that sample Au@Cu_2O_2 was more active for CO oxidation when treated under reducing atmosphere than under oxidizing atmosphere. The TOF values of Au@Cu_2O_2 treated in 10% O_2 (referred to as Au@Cu_2_O_2 in table 4.9) were significantly lower than the TOF values of Au@Cu_2O_2 treated in 10% H_2. This indicates that a mixed phase of Au and Cu atoms was catalytic more active than only a oxidized

Cu phase on the surface. Furthermore, this result gives more insight in the deactivation of AuCu NPs, as figure 4.41 shows that the NPs had been redistributed in a core-shell structure during the reaction. However, it should be noticed that the oxidation state of Cu after the catalytic reaction is unknown, and could differ with the tested core-shell NPs. Further characterization of the NPs with XRD, SAED or electron energy loss spectroscopy (EELS) can provide more information of the oxidation state of the oxidized copper after the catalytic test.

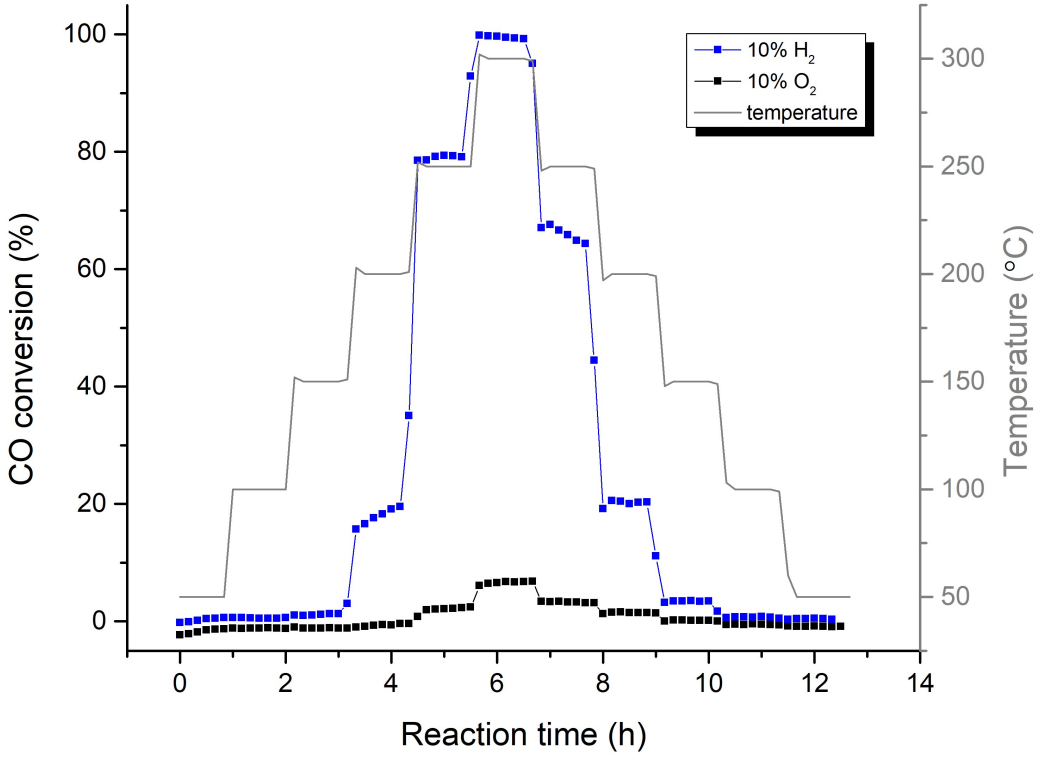

Figure 4.42: The temperature-dependent CO conversion as a function of reaction time for sample Au@Cu_2O_2 after thermal treatment at 500°C under different atmospheres for ligand removal. The blue and black lines correspond to sample Au@Cu_2O_2 heated under a 10% H_2/N2 (sample Au@Cu_2) and 10% O_2/N_2 atmosphere, respectively. The temperature profile is plotted as a gray line (right-axis)

5 Conclusion

In this thesis, three synthesis routes were presented to study how AuCu NPs can be synthesized via aqueous colloidal synthesis. These synthesis routes involved the overgrowth of oxidized Cu on Au NPs in an aqueous medium, followed by a thermal treatment under reducing atmosphere. Through this novel approach, AuCu NPs were obtained in a more sustainable manner compared to literature, without the use of toxic chemicals. However, limitations were encountered regarding the control over the metal composition and stability of the AuCu NPs.

In the first route, the metal overgrowth was performed on Au NPs coated with a mesoporous silica shell, hereby obtaining AuCu NPs with approximately 21% Cu after thermal reduction. This Cu content could be increased to approximately 28% by etching the Au core prior to the overgrowth. While the silica shell provided stability to the NPs, it limited the synthesis of AuCu NPs with higher Cu contents. This drawback was tackled in the second synthesis route by performing Cu_2O overgrowth on Au NPs, stabilized with PVP ligands. This resulted in Au@Cu_2O NPs with a Cu content up to 87%. The metal composition was adjusted by varying the Au concentration. Unfortunately, synthesizing NPs with a lower Cu percentage resulted in polydisperse particle sizes and compositions. The deposition of the NPs on a silica support was also challenging, as clustering occurred, leading to aggregation upon thermal treatment. The third synthesis route avoided clustering by growing a Cu_2O shell on supported Au NPs, resulting in well-dispersed NPs. However, control over metal composition was limited due to the formation of monometallic Cu_2O particles. In conclusion, AuCu NPs can be synthesized via aqueous colloidal methods, but further optimization is necessary to obtain monodisperse AuCu NPs with various metal compositions, without the formation of individual Cu species.

It was determined with electron microscopy techniques and XRD that the metal distribution of core-shell Au@Cu_xO NPs changed to alloyed AuCu NPs upon thermal treatment ($\geq$ 300°C) under a reducing atmosphere. It was also demonstrated that the core-shell structure could be retained under oxidizing conditions, while removing the ligands prior to catalysis.

This thesis also shed a light on the potential of AuCu NPs as a catalysts for CO oxidation. Bimetallic AuCu NPs, obtained using synthesis route 3, were found to be significantly more active compared to monometallic Au NPs. Additionally, the catalytic activity of the supported AuCu NPs enhanced with higher Cu content. To exclude the influence of the monometallic Cu particles in the samples, the catalytic performance of Cu NPs should also be examined. Results have showed that alloyed AuCu NPs were significantly more active than core-shell Au@Cu_2O NPs, illustrating the importance of a mixed phase of Au and Cu for the oxidation of CO. Further research is required to obtain a more in-depth understanding of the catalytic performance of AuCu NPs in CO oxidation (as discussed in chapter 6).

6 Outlook

6.1 The aqueous synthesis of AuCu NPs

This thesis demonstrated three synthesis routes for obtaining AuCu NPs in an aqueous solution. The third method presented a promising pathway for obtaining well-dispersed AuCu NPs on a silica support. However, several issues were encountered upon upscaling from 25 mg to 500 mg. First, the Cu_2O overgrowth occurred not only on the Au core, but also resulted in the formation of monometallic Cu_2O particles on the silica support. This affected the reproducibility of the synthesis protocol and the catalytic performance of the samples. Interestingly, individual Cu species were not observed with electron microscopy in small-scale syntheses, using relatively low amounts of Cu precursor. Additional washing steps prior to drying the support could remove the Cu_2O particles. Secondly, the overgrowth of Cu_2O became more inhomogeneous upon upscaling. Further investigation into the optimal amount of reactants is required to address this issue. However, this problem likely stems from the accelerated rate of the Cu_2O overgrowth, as observed by the rapid color change of the reaction mixture. Slowing down the chemical reduction of the Cu^{2+}-ions could result in more homogeneous particles and even prevent the formation of individual Cu_2O particles. Adjusting the addition rate of reactants by using a syringe pump or lowering the reaction temperature could mitigate the issue.

The first synthesis method also provided stable AuCu NPs due to the mesoporous silica shell around the NPs. However, the silica shell restricted the metal overgrowth, thereby limiting the range of metal compositions that could be obtained. An alternative approach to etching the Au core, could be to selectively etch the silica shell with etching agents, such as NaOH or $NaBH_4$ [82]. If the silica shell can be etched in a controlled manner, the Cu_xO overgrowth coud be regulated through the etching of the silica shell.

6.2 The catalytic performance of AuCu NPs

This thesis merely touched upon possible catalytic tests that can be conducted. The catalytic activity of bimetallic AuCu NPs have been compared to monometallic Au NPs in CO oxidation. In order to draw conclusions on the synergistic effects of AuCu NPs, it is also important to investigate the catalytic performance of monometallic Cu NPs. Additionally, it would be interesting to test a broader range of metal compositions in order to determine the most effective AuCu catalysts for the oxidation of CO. In particular, composition with 25%, 50% and 75% Cu would be valuable due to the potential formation of ordered intermetallic phases, which provide well-defined metal compositions and relatively uniform surface geometry.

This thesis also compared the activity of core-shell Au@Cu_2O NPs in CO oxidation with alloyed AuCu NPs. In addition, it would be interesting to compare these NPs to core-shell Au@Cu NPs to further study the role of the metal distribution on the catalytic activity in CO oxidation. Temperature-programmed reduction (TPR) analysis could be used to determine at which the temperature Cu_2O is reduced. If this temperature is below the minimum temperature required to mix Au and Cu, core-shell Au@Cu NPs could be obtained and studied.

A better understanding on the structural changes of the AuCu NPs during the oxidation of CO could give more insight into their catalytic performance. The metal rearrangement could be observed with in-situ TEM heating experiments combined with EDX under similar conditions as the reaction. Electron energy loss spectroscopy (EELS), electron diffraction and XRD can be employed to gain more information on the oxidation state of Cu after the reaction.

In addition to studying the metal distribution and composition, the effect of particle size on catalyzing CO oxidation could be studied. The syntheses methods presented in this thesis rely on colloidal strategies, providing precise control over the morphology of NPs. In particular, AuCu nanoparticles between 1-10 nm could be of interest, as it has been

reported that Au NPs with a diameter smaller than 2 nm exhibit enhanced catalytic activity [2]. Furthermore, varying the support material by replacing silica with more active metal oxides, such as titania, may enhance dissociation of oxygen, and thereby the catalyst performance [62].

In addition to investigating the catalytic activity of the supported NPs, their stability should also be examined in order to draw conclusions on the catalytic performance. Catalytic tests could be conducted where the CO conversion is monitored under a constant temperature for several hours. This allows for detection of potential deactivation of the catalyst material over a longer time period, indicated by a significant decrease in CO conversion. Additionally, deactivation could be avoided by performing catalytic tests at lower temperatures than 300°C.

Furthermore, the versatility of the AuCu NPs as a catalyst can be examined by investigating other chemical reactions beyond the oxidation of CO. For instance, studying their potential as a catalysts for electrochemical reduction of CO_2 or selective hydrogenation of unsaturated compounds could be a promising area of research. Beside their catalytic applications, AuCu NPs have also found interest in optical and biomedical applications [86, 36, 87], which could be further investigated.

LAYMAN'S ABSTRACT

Catalysts are compounds that accelerate chemical reactions. They play a vital role in many industrial processes and chemical reactions. Many catalysts are composed of tiny particles, called nanoparticles. Due to their small size, many atoms in the nanoparticles are exposed to the surface, making them active in chemical reactions. Nanoparticles consisting on two metals are known as bimetallic nanoparticles. Their catalytic activity can be enhanced due to the interaction between these two metals. This thesis focused on bimetallic gold-copper nanoparticles. Gold-copper nanoparticles are promising catalysts for the conversion of carbon monoxide (CO), as gold and copper atoms can work together to facilitate the interaction of CO with oxygen.

Traditionally, gold-copper nanoparticles have been synthesized in organic solutions. However, synthesizing the nanoparticles in aqueous (water-based) solutions would be more sustainable, less harmful and less expensive. This thesis has demonstrated synthesis strategies to obtain gold-copper nanoparticles in aqueous solutions. The strategies showed promise, but each had their limitations. Optimization is required to synthesize stable gold-copper nanoparticles with different gold and copper contents in aqueous solution.

We found that gold-copper nanoparticles exhibited enhanced activity in converting CO compared to monometallic gold nanoparticles. This shows the potential of gold-copper nanoparticles as a catalyst for CO oxidation. Additionally, the catalytic activity increased with increasing copper fraction in gold-copper nanoparticles. Further research is needed to get a better understanding on the catalytic performance of gold-copper nanoparticles.

ACKNOWLEDGEMENTS

The research presented in this thesis could not have been possible without the invaluable help and support of many people.

First, I would like to express my sincere gratitude to my thesis supervisors Jessi van der Hoeven and Marta Perxés i Perich. My master's project under your supervision has been a great pleasure and has taught me countless things. Your insightful discussions and feedback made a tremendous difference. Our pleasant conversations have made this journey even more enjoyable. Jessi, thank you for giving me the opportunity to work on this project. Your expertise in this field along with your enthousiasm were essential to the project and greatly appreciated. Marta, thank you for your help and support in the lab and your guidance throughout the project. I always felt welcome to approach you with any question I had. Additionally, I appreciate the time and effort you dedicated to collecting EDX data from numerous samples.

Secondly, I would like to acknowledge professor Petra de Jongh for being my second examinor and making this project possible.

I thank Just Pé Jonasse for his time and suggestions. Your experience with catalysis and knowledge about gold-copper nanoparticles were extremely helpful.

I would also like to thank Hans Meeldijk and Chris Schneijdenberg for teaching me how to work with an electron microscope and their help in resolving some technical EM problems. Special thanks Dennie Wezendonk, Remco Dalebout and Jan Willem de Rijk for the technical assistance.

Finally, I would like to thank all people in the MCC group, including the students, for creating such a warm and fun work environment.

REFERENCES

[1] G. Rothenberg, *Catalysis. Concepts and Green Applications.* Wiley-VCH, 2008.

[2] M. Haruta, N. Yamada, T. Kobayashi, and S. Iijima, "Gold catalysts prepared by coprecipitation for low-temperature oxidation of hydrogen and of carbon monoxide," *Journal of Catalysis*, vol. 115, no. 2, pp. 301–309, Feb. 1989. [Online]. Available: https://www.sciencedirect.com/science/article/pii/0021951789900341

[3] C. A. H. Price, L. Pastor-Pérez, S. Ivanova, T. R. Reina, and J. Liu, "The Success Story of Gold-Based Catalysts for Gas- and Liquid-Phase Reactions: A Brief Perspective and Beyond," *Frontiers in Chemistry*, vol. 7, 2019. [Online]. Available: https://www.frontiersin.org/articles/10.3389/fchem.2019.00691

[4] A. S. Alshammari, "Heterogeneous Gold Catalysis: From Discovery to Applications," *Catalysts*, vol. 9, no. 5, p. 402, May 2019, number: 5 Publisher: Multidisciplinary Digital Publishing Institute. [Online]. Available: https://www.mdpi.com/2073-4344/9/5/402

[5] A. K. Singh and Q. Xu, "Synergistic Catalysis over Bimetallic Alloy Nanoparticles," *ChemCatChem*, vol. 5, no. 3, pp. 652–676, 2013, _eprint: https://onlinelibrary.wiley.com/doi/pdf/10.1002/cctc.201200591. [Online]. Available: https://onlinelibrary.wiley.com/doi/abs/10.1002/cctc.201200591

[6] P. Destro, T. M. Kokumai, A. Scarpellini, L. Pasquale, L. Manna, M. Colombo, and D. Zanchet, "The Crucial Role of the Support in the Transformations of Bimetallic Nanoparticles and Catalytic Performance," *ACS Catalysis*, vol. 8, no. 2, pp. 1031–1037, Feb. 2018. [Online]. Available: https://pubs.acs.org/doi/10.1021/acscatal.7b03685

[7] N. K. Ojha, G. V. Zyryanov, A. Majee, V. N. Charushin, O. N. Chupakhin, and S. Santra, "Copper nanoparticles as inexpensive and efficient catalyst: A valuable contribution in organic synthesis," *Coordination Chemistry Reviews*, vol. 353, pp. 1–57, Dec. 2017. [Online]. Available: https://www.sciencedirect.com/science/article/pii/S0010854517303296

[8] C. L. Bracey, P. R. Ellis, and G. J. Hutchings, "Application of copper–gold alloys in catalysis: current status and future perspectives," *Chemical Society Reviews*, vol. 38, no. 8, p. 2231, 2009.

[9] L. Delannoy, G. Thrimurthulu, P. S. Reddy, C. Méthivier, J. Nelayah, B. M. Reddy, C. Ricolleau, and C. Louis, "Selective hydrogenation of butadiene

over TiO2 supported copper, gold and gold–copper catalysts prepared by deposition–precipitation," *Physical Chemistry Chemical Physics*, vol. 16, no. 48, pp. 26 514–26 527, Nov. 2014, publisher: The Royal Society of Chemistry. [Online]. Available: https://pubs.rsc.org/en/content/articlelanding/2014/cp/c4cp02141j

[10] J. W. Lee, X. Liu, and C.-Y. Mou, "Selective Hydrogenation of Acetylene over SBA-15 Supported Au—Cu Bimetallic Catalysts," *Journal of the Chinese Chemical Society*, vol. 60, no. 7, pp. 907–914, 2013, _eprint: https://onlinelibrary.wiley.com/doi/pdf/10.1002/jccs.201300160. [Online]. Available: https://onlinelibrary.wiley.com/doi/abs/10.1002/jccs.201300160

[11] D. Kim, J. Resasco, Y. Yu, A. M. Asiri, and P. Yang, "Synergistic geometric and electronic effects for electrochemical reduction of carbon dioxide using gold–copper bimetallic nanoparticles," *Nature Communications*, vol. 5, no. 1, p. 4948, Sep. 2014, number: 1 Publisher: Nature Publishing Group. [Online]. Available: https://www.nature.com/articles/ncomms5948

[12] C.-J. Jia and F. Schüth, "Colloidal metal nanoparticles as a component of designed catalyst," *Physical Chemistry Chemical Physics*, vol. 13, no. 7, pp. 2457–2487, 2011, publisher: Royal Society of Chemistry. [Online]. Available: https://pubs.rsc.org/en/content/articlelanding/2011/cp/c0cp02680h

[13] P. Destro, M. Colombo, M. Prato, R. Brescia, L. Manna, and D. Zanchet, "Au(1-x)Cu(x) colloidal nanoparticles synthesized via a one-pot approach: understanding the temperature effect on the Au : Cu ratio," *RSC Advances*, vol. 6, no. 27, pp. 22 213–22 221, 2016.

[14] W. Zhan, J. Wang, H. Wang, J. Zhang, X. Liu, P. Zhang, M. Chi, Y. Guo, Y. Guo, G. Lu, S. Sun, S. Dai, and H. Zhu, "Crystal Structural Effect of AuCu Alloy Nanoparticles on Catalytic CO Oxidation," *Journal of the American Chemical Society*, vol. 139, no. 26, pp. 8846–8854, Jul. 2017. [Online]. Available: https://pubs.acs.org/doi/10.1021/jacs.7b01784

[15] S. K. Sinha, C. Srivastava, S. Sampath, and K. Chattopadhyay, "Tunability of monodispersed intermetallic AuCu nanoparticles through understanding of reaction pathways," *RSC Advances*, vol. 5, no. 6, pp. 4389–4395, Dec. 2014, publisher: The Royal Society of Chemistry. [Online]. Available: https://pubs.rsc.org/en/content/articlelanding/2015/ra/c4ra12059k

[16] D. H. Everett, "Basic principles of colloid science: London, 1988. paperback," *Journal of Chemical Technology & Biotechnology*, vol. 45, no. 4, pp. 328–329, 1989. [Online]. Available: https://onlinelibrary.wiley.com/doi/abs/10.1002/jctb.280450412

[17] R. Brown, "XXVII. A brief account of microscopical observations made in the months of June, July and August 1827, on the particles contained in the pollen of plants; and on the general existence of active molecules in organic and inorganic

bodies," *The Philosophical Magazine*, vol. 4, no. 21, pp. 161–173, Sep. 1828, publisher: Taylor & Francis _eprint: https://doi.org/10.1080/14786442808674769. [Online]. Available: https://doi.org/10.1080/14786442808674769

[18] V. M. B.V. Derjaguin, N.V. Churaev, "The derjaguin—landau—verwey—overbeek (dlvo) theory of stability of lyophobic colloids," *Surface forces, Springer US*, pp. 293–320, 1987.

[19] J. H. Adair, E. Suvaci, and J. Sindel, *Surface and Colloid Chemistry*, K. H. J. Buschow, R. W. Cahn, M. C. Flemings, B. Ilschner, E. J. Kramer, S. Mahajan, and P. Veyssière, Eds. Oxford: Elsevier, 2001. [Online]. Available: https://www.sciencedirect.com/science/article/pii/B0080431526016223

[20] R. B. Grubbs, "Roles of Polymer Ligands in Nanoparticle Stabilization," *Polymer Reviews*, vol. 47, no. 2, pp. 197–215, Apr. 2007, publisher: Taylor & Francis _eprint: https://doi.org/10.1080/15583720701271245. [Online]. Available: https://doi.org/10.1080/15583720701271245

[21] A. Heuer-Jungemann, N. Feliu, I. Bakaimi, M. Hamaly, A. Alkilany, I. Chakraborty, A. Masood, M. F. Casula, A. Kostopoulou, E. Oh, K. Susumu, M. H. Stewart, I. L. Medintz, E. Stratakis, W. J. Parak, and A. G. Kanaras, "The Role of Ligands in the Chemical Synthesis and Applications of Inorganic Nanoparticles," *Chemical Reviews*, vol. 119, no. 8, pp. 4819–4880, Apr. 2019, publisher: American Chemical Society. [Online]. Available: https://doi.org/10.1021/acs.chemrev.8b00733

[22] F. Matter, A. L. Luna, and M. Niederberger, "From colloidal dispersions to aerogels: How to master nanoparticle gelation," *Nano Today*, vol. 30, p. 100827, Feb. 2020. [Online]. Available: https://www.sciencedirect.com/science/article/pii/S1748013219303524

[23] J. Turkevich, P. C. Stevenson, and J. Hillier, "A study of the nucleation and growth processes in the synthesis of colloidal gold," *Discussions of the Faraday Society*, vol. 11, no. 0, pp. 55–75, Jan. 1951, publisher: The Royal Society of Chemistry. [Online]. Available: https://pubs.rsc.org/en/content/articlelanding/1951/df/df9511100055

[24] G. Frens, "Controlled Nucleation for the Regulation of the Particle Size in Monodisperse Gold Suspensions," *Nature Physical Science*, vol. 241, no. 105, pp. 20–22, Jan. 1973, number: 105 Publisher: Nature Publishing Group. [Online]. Available: https://www.nature.com/articles/physci241020a0

[25] C. Donegá, *Nanoparticles: Workhorses of Nanoscience*. Heidelberg: Springer Berlin Heidelberg, 09 2014.

[26] J. Polte, R. Erler, A. F. Thünemann, S. Sokolov, T. T. Ahner, K. Rademann, F. Emmerling, and R. Kraehnert, "Nucleation and Growth of Gold Nanoparticles Studied via in situ Small Angle X-ray Scattering at Millisecond Time Resolution,"

ACS Nano, vol. 4, no. 2, pp. 1076–1082, Feb. 2010, publisher: American Chemical Society. [Online]. Available: https://doi.org/10.1021/nn901499c

[27] V. Polshettiwar, R. Luque, A. Fihri, H. Zhu, M. Bouhrara, and J.-M. Basset, "Magnetically Recoverable Nanocatalysts," *Chemical Reviews*, vol. 111, no. 5, pp. 3036–3075, May 2011. [Online]. Available: https://pubs.acs.org/doi/10.1021/cr100230z

[28] J. Piella, N. G. Bastús, and V. Puntes, "Size-Controlled Synthesis of Sub-10-nanometer Citrate-Stabilized Gold Nanoparticles and Related Optical Properties." *Chemistry of Materials*, vol. 28, no. 4, pp. 1066–1075, Feb. 2016. [Online]. Available: https://pubs.acs.org/doi/10.1021/acs.chemmater.5b04406

[29] J. Schubert and M. Chanana, "Coating Matters: Review on Colloidal Stability of Nanoparticles with Biocompatible Coatings in Biological Media, Living Cells and organisms," *Current Medicinal Chemistry*, vol. 25, no. 35, pp. 4556–4586, Oct. 2019. [Online]. Available: https://www.ncbi.nlm.nih.gov/pmc/articles/PMC7040520/

[30] J. E. S. van der Hoeven, J. Jelic, L. A. Olthof, G. Totarella, R. J. A. van Dijk-Moes, J.-M. Krafft, C. Louis, F. Studt, A. van Blaaderen, and P. E. de Jongh, "Unlocking synergy in bimetallic catalysts by core–shell design," *Nature Materials*, vol. 20, no. 9, pp. 1216–1220, Sep. 2021, number: 9 Publisher: Nature Publishing Group. [Online]. Available: https://www.nature.com/articles/s41563-021-00996-3

[31] J. Chen, R. Zhang, L. Han, B. Tu, and D. Zhao, "One-pot synthesis of thermally stable gold@mesoporous silica core-shell nanospheres with catalytic activity," *Nano Research*, vol. 6, no. 12, pp. 871–879, Dec. 2013. [Online]. Available: http://link.springer.com/10.1007/s12274-013-0363-1

[32] V. Gubala, G. Giovannini, F. Kunc, M. Monopoli, and C. Moore, "Dye-doped silica nanoparticles: Synthesis, surface chemistry and bioapplications," *Cancer Nanotechnology*, vol. 11, Jan. 2020.

[33] I. Gorelikov and N. Matsuura, "Single-Step Coating of Mesoporous Silica on Cetyltrimethyl Ammonium Bromide-Capped Nanoparticles," *Nano Letters*, vol. 8, no. 1, pp. 369–373, Jan. 2008. [Online]. Available: https://pubs.acs.org/doi/10.1021/nl0727415

[34] R. I. Nooney, D. Thirunavukkarasu, Y. Chen, R. Josephs, and A. E. Ostafin, "Self-Assembly of Mesoporous Nanoscale Silica/Gold Composites," *Langmuir*, vol. 19, no. 18, pp. 7628–7637, Sep. 2003. [Online]. Available: https://pubs.acs.org/doi/10.1021/la034522e

[35] P. Yang, S. Gai, and J. Lin, "Functionalized mesoporous silica materials for controlled drug delivery," *Chemical Society Reviews*, vol. 41, no. 9, pp. 3679–3698, Apr. 2012, publisher: The Royal Society of Chemistry. [Online]. Available: https://pubs.rsc.org/en/content/articlelanding/2012/cs/c2cs15308d

[36] C. M. Andolina, A. C. Dewar, A. M. Smith, L. E. Marbella, M. J. Hartmann, and J. E. Millstone, "Photoluminescent Gold–Copper Nanoparticle Alloys with Composition-Tunable Near-Infrared Emission," *Journal of the American Chemical Society*, vol. 135, no. 14, pp. 5266–5269, Apr. 2013, publisher: American Chemical Society. [Online]. Available: https://doi.org/10.1021/ja400569u

[37] S. Kim, Y. Jang, K. Y. Yoon, and J. Park, "Surface engineered gold nanoparticles through highly stable metal–surfactant complexes," *Journal of Colloid and Interface Science*, vol. 464, pp. 110–116, Feb. 2016. [Online]. Available: https://www.sciencedirect.com/science/article/pii/S0021979715302794

[38] R. He, Y.-C. Wang, X. Wang, Z. Wang, G. Liu, W. Zhou, L. Wen, Q. Li, X. Wang, X. Chen, J. Zeng, and J. G. Hou, "Facile synthesis of pentacle gold–copper alloy nanocrystals and their plasmonic and catalytic properties," *Nature Communications*, vol. 5, no. 1, p. 4327, Jul. 2014, number: 1 Publisher: Nature Publishing Group. [Online]. Available: https://www.nature.com/articles/ncomms5327

[39] D.-Y. Liu, S.-Y. Ding, H.-X. Lin, B.-J. Liu, Z.-Z. Ye, F.-R. Fan, B. Ren, and Z.-Q. Tian, "Distinctive Enhanced and Tunable Plasmon Resonant Absorption from Controllable Au@Cu $_2$ O Nanoparticles: Experimental and Theoretical Modeling," *The Journal of Physical Chemistry C*, vol. 116, no. 7, pp. 4477–4483, Feb. 2012. [Online]. Available: https://pubs.acs.org/doi/10.1021/jp211565c

[40] M.-Y. Kuo, C.-F. Hsiao, Y.-H. Chiu, T.-H. Lai, M.-J. Fang, J.-Y. Wu, J.-W. Chen, C.-L. Wu, K.-H. Wei, H.-C. Lin, and Y.-J. Hsu, "Au@Cu2O core@shell nanocrystals as dual-functional catalysts for sustainable environmental applications," *Applied Catalysis B: Environmental*, vol. 242, pp. 499–506, Mar. 2019. [Online]. Available: https://www.sciencedirect.com/science/article/pii/S0926337318309044

[41] S. Wu, "Preparation of fine copper powder using ascorbic acid as reducing agent and its application in MLCC," *Materials Letters*, vol. 61, no. 4-5, pp. 1125–1129, Feb. 2007. [Online]. Available: https://linkinghub.elsevier.com/retrieve/pii/S0167577X06007749

[42] P. Fedorov and S. Volkov, "Au–Cu Phase Diagram," *Russian Journal of Inorganic Chemistry*, vol. 61, pp. 772–775, Jun. 2016.

[43] F. Monji and M. A. Jabbareh, "Revisiting The Phase Diagram of Au – Cu Alloy at Nanoscales," *International Journal of Thermodynamics*, vol. 25, no. 2, pp. 24–31, Jun. 2022, number: 2. [Online]. Available: https://dergipark.org.tr/en/pub/ijot/issue/70015/1000945

[44] I. Freestone, N. Meeks, M. Sax, and C. Higgitt, "The Lycurgus Cup — A Roman nanotechnology," *Gold Bulletin*, vol. 40, no. 4, pp. 270–277, Dec. 2007. [Online]. Available: https://doi.org/10.1007/BF03215599

[45] V. Amendola, R. Pilot, M. Frasconi, O. M. Maragò, and M. A. Iatì, "Surface plasmon resonance in gold nanoparticles: a review," *Journal of Physics: Condensed Matter*, vol. 29, no. 20, p. 203002, Apr. 2017, publisher: IOP Publishing. [Online]. Available: https://dx.doi.org/10.1088/1361-648X/aa60f3

[46] X. Huang and M. A. El-Sayed, "Gold nanoparticles: Optical properties and implementations in cancer diagnosis and photothermal therapy," *Journal of Advanced Research*, vol. 1, no. 1, pp. 13–28, Jan. 2010. [Online]. Available: https://www.sciencedirect.com/science/article/pii/S2090123210000056

[47] P. Hawe, V. Silveira, R. Vadell, E. Lewin, and J. Sa, "Plasmon-Mediated Oxidation Reaction on Au/p-Cu2O: The Origin of Hot Holes," *Physchem*, vol. 1, pp. 163–175, Jul. 2021.

[48] A. R. Carrasco-Hernández, R. I. Ruvalcaba-Ontiveros, E. Martínez-Guerra, J. A. Duarte-Moller, and H. E. Esparza-Ponce, "Evolution of Structural and Optical Properties of Cuprous Oxide Particles for Visible Light Absorption," *Journal of Nanomaterials*, vol. 2022, p. e7964428, Sep. 2022, publisher: Hindawi. [Online]. Available: https://www.hindawi.com/journals/jnm/2022/7964428/

[49] Z. Xu, Y. Li, Y. Lin, and T. Zhu, "A review of the catalysts used in the reduction of NO by CO for gas purification," *Environmental Science and Pollution Research*, vol. 27, no. 7, pp. 6723–6748, Mar. 2020. [Online]. Available: https://doi.org/10.1007/s11356-019-07469-w

[50] C. Feng, X. Liu, T. Zhu, and M. Tian, "Catalytic oxidation of CO on noble metal-based catalysts," *Environmental Science and Pollution Research*, vol. 28, no. 20, pp. 24 847–24 871, May 2021. [Online]. Available: https://doi.org/10.1007/s11356-021-13008-3

[51] Y. Zhou, Z. Wang, and C. Liu, "Perspective on CO oxidation over Pd-based catalysts," *Catalysis Science & Technology*, vol. 5, no. 1, pp. 69–81, Dec. 2014, publisher: The Royal Society of Chemistry. [Online]. Available: https://pubs.rsc.org/en/content/articlelanding/2015/cy/c4cy00983e

[52] T.-J. Huang and D.-H. Tsai, "CO Oxidation Behavior of Copper and Copper Oxides," *Catalysis Letters*, vol. 87, pp. 173–178, Apr. 2003.

[53] G. G. Jernigan and G. A. Somorjai, "Carbon Monoxide Oxidation over Three Different Oxidation States of Copper: Metallic Copper, Copper (I) Oxide, and Copper (II) Oxide - A Surface Science and Kinetic Study," *Journal of Catalysis*, vol. 147, no. 2, pp. 567–577, Jun. 1994. [Online]. Available: https://www.sciencedirect.com/science/article/pii/S0021951784711730

[54] R. V. Gonçalves, R. Wojcieszak, H. Wender, C. Sato B. Dias, L. L. R. Vono, D. Eberhardt, S. R. Teixeira, and L. M. Rossi, "Easy Access to Metallic Copper Nanoparticles with High Activity and Stability for CO Oxidation," *ACS Applied*

Materials & Interfaces, vol. 7, no. 15, pp. 7987–7994, Apr. 2015, publisher: American Chemical Society. [Online]. Available: https://doi.org/10.1021/acsami.5b00129

[55] H. P. Bonzel and R. Ku, "Mechanisms of the catalytic carbon monoxide oxidation on Pt (110)," *Surface Science*, vol. 33, no. 1, pp. 91–106, Oct. 1972. [Online]. Available: https://www.sciencedirect.com/science/article/pii/003960287290101X

[56] G. Xu, R. Wang, F. Yang, D. Ma, Z. Yang, and Z. Lu, "CO oxidation on single Pd atom embedded defect-graphene via a new termolecular Eley-Rideal mechanism," *Carbon*, vol. 118, pp. 35–42, Jul. 2017. [Online]. Available: https://www.sciencedirect.com/science/article/pii/S0008622317302750

[57] G. Ma, L. Wang, X. Wang, L. Li, and H. Ma, "CO Oxidation over Alumina-Supported Copper Catalysts," *Catalysts*, vol. 12, no. 9, p. 1030, Sep. 2022, number: 9 Publisher: Multidisciplinary Digital Publishing Institute. [Online]. Available: https://www.mdpi.com/2073-4344/12/9/1030

[58] M. A. Saqlain, A. Hussain, M. Siddiq, and A. A. Leitão, "A DFT+U study of the Mars Van Krevelen mechanism of CO oxidation on Au/TiO2 catalysts," *Applied Catalysis A: General*, vol. 519, pp. 27–33, Jun. 2016. [Online]. Available: https://www.sciencedirect.com/science/article/pii/S0926860X16301442

[59] Z.-P. Liu, P. Hu, and A. Alavi, "Catalytic Role of Gold in Gold-Based Catalysts: A Density Functional Theory Study on the CO Oxidation on Gold," *Journal of the American Chemical Society*, vol. 124, no. 49, pp. 14 770–14 779, Dec. 2002, publisher: American Chemical Society. [Online]. Available: https://doi.org/10.1021/ja0205885

[60] K. Grzelak, I. Sobczak, C.-M. Yang, and M. Ziolek, "Gold-copper catalysts supported on SBA-15 with long and short channels – Characterization and the use in propene oxidation," *Catalysis Today*, vol. 356, pp. 155–164, Oct. 2020. [Online]. Available: https://www.sciencedirect.com/science/article/pii/S0920586119302305

[61] L. Li, C. Wang, X. Ma, Z. Yang, and X. Lu, "An Au-Cu Bimetal Catalyst Supported on Mesoporous TiO2 with Stable Catalytic Performance in CO Oxidation," *Chinese Journal of Catalysis*, vol. 33, no. 11, pp. 1778–1782, Nov. 2012. [Online]. Available: https://www.sciencedirect.com/science/article/pii/S1872206711604713

[62] K. Qian, L. Luo, H. Bao, Q. Hua, Z. Jiang, and W. Huang, "Catalytically active structures of SiO2-supported Au nanoparticles in low-temperature CO oxidation," *Catalysis Science & Technology*, vol. 3, no. 3, pp. 679–687, Feb. 2013, publisher: The Royal Society of Chemistry. [Online]. Available: https://pubs.rsc.org/en/content/articlelanding/2013/cy/c2cy20481a

[63] C. Graf, D. L. J. Vossen, A. Imhof, and A. van Blaaderen, "A General Method To Coat Colloidal Particles with Silica," *Langmuir*, vol. 19, no. 17, pp. 6693–6700, Aug. 2003, publisher: American Chemical Society. [Online]. Available: https://doi.org/10.1021/la0347859

[64] J. Fokkema, J. Fermie, N. Liv, D. J. van den Heuvel, T. O. M. Konings, G. A. Blab, A. Meijerink, J. Klumperman, and H. C. Gerritsen, "Fluorescently Labelled Silica Coated Gold Nanoparticles as Fiducial Markers for Correlative Light and Electron Microscopy," *Scientific Reports*, vol. 8, no. 1, p. 13625, Sep. 2018, number: 1 Publisher: Nature Publishing Group. [Online]. Available: https://www.nature.com/articles/s41598-018-31836-1

[65] L. S. B. Upadhyay and N. Kumar, "Green synthesis of copper nanoparticle using glucose and polyvinylpyrrolidone (PVP)," *Inorganic and Nano-Metal Chemistry*, vol. 47, no. 10, pp. 1436–1440, Oct. 2017, publisher: Taylor & Francis _eprint: https://doi.org/10.1080/24701556.2017.1357576. [Online]. Available: https://doi.org/10.1080/24701556.2017.1357576

[66] W. Yu, H. Xie, L. Chen, Y. Li, and C. Zhang, "Synthesis and Characterization of Monodispersed Copper Colloids in Polar Solvents," *Nanoscale Research Letters*, vol. 4, no. 5, p. 465, May 2009. [Online]. Available: https://nanoscalereslett.springeropen.com/articles/10.1007/s11671-009-9264-3

[67] S. R. Jena, M. B. Bhavya, S. R. Manippady, P. Bhol, S. Swain, M. Saxena, P. K. Misra, and A. K. Samal, "Catalytic activity of Au@Cu2O core-shell nanostructure for the organic pollutant remediation," *Journal of Physics and Chemistry of Solids*, vol. 152, p. 109935, May 2021. [Online]. Available: https://www.sciencedirect.com/science/article/pii/S0022369721000019

[68] J. E. S. van der Hoeven, T.-S. Deng, W. Albrecht, L. A. Olthof, M. A. van Huis, P. E. de Jongh, and A. van Blaaderen, "Structural Control over Bimetallic Core–Shell Nanorods for Surface-Enhanced Raman Spectroscopy," *ACS Omega*, vol. 6, no. 10, pp. 7034–7046, Mar. 2021. [Online]. Available: https://pubs.acs.org/doi/10.1021/acsomega.0c06321

[69] P. K. Jain and M. A. El-Sayed, "Universal Scaling of Plasmon Coupling in Metal Nanostructures: Extension from Particle Pairs to Nanoshells," *Nano Letters*, vol. 7, no. 9, pp. 2854–2858, Sep. 2007, publisher: American Chemical Society. [Online]. Available: https://doi.org/10.1021/nl071496m

[70] A. Khan, A. Rashid, R. Younas, and R. Chong, "A chemical reduction approach to the synthesis of copper nanoparticles," *International Nano Letters*, vol. 6, no. 1, pp. 21–26, Mar. 2016. [Online]. Available: http://link.springer.com/10.1007/s40089-015-0163-6

[71] L. Xiong, H. Xiao, S. Chen, Z. Chen, X. Yi, S. Wen, and G. Zheng, "A fast and simplified synthesis of cuprous oxide nanoparticles: anneal studies and photocatalytic activity," *RSC Advances*.

[72] X. Glad, J. Profili, M. S. Cha, and A. Hamdan, "Synthesis of copper and copper oxide nanomaterials by electrical discharges in water with various electrical

conductivities," *Journal of Applied Physics*, vol. 127, no. 2, p. 023302, Jan. 2020. [Online]. Available: http://aip.scitation.org/doi/10.1063/1.5129647

[73] L.-I. Hung, C.-K. Tsung, W. Huang, and P. Yang, "Room-Temperature Formation of Hollow Cu2O Nanoparticles," *Advanced Materials*, vol. 22, no. 17, pp. 1910–1914, 2010, _eprint: https://onlinelibrary.wiley.com/doi/pdf/10.1002/adma.200903947. [Online]. Available: https://onlinelibrary.wiley.com/doi/abs/10.1002/adma.200903947

[74] P. H. KV Anasuya, MK Veeraiah, "Synthesis and Characterisation of Poly (Vinylpyrrolidone)-Copper (II) Complexes," *Research Journal of Chemical Sciences*, vol. 5, no. 2, pp. 64–69, 2015. [Online]. Available: http://www.isca.in/rjcs/Archives/v5/i2/11.ISCA-RJCS-2015-015.php

[75] L. Liu and A. Corma, "Metal Catalysts for Heterogeneous Catalysis: From Single Atoms to Nanoclusters and Nanoparticles," *Chemical Reviews*, vol. 118, no. 10, pp. 4981–5079, May 2018, publisher: American Chemical Society. [Online]. Available: https://doi.org/10.1021/acs.chemrev.7b00776

[76] R. M. Rioux, H. Song, M. Grass, S. Habas, K. Niesz, J. D. Hoefelmeyer, P. Yang, and G. A. Somorjai, "Monodisperse platinum nanoparticles of well-defined shape: synthesis, characterization, catalytic properties and future prospects," *Topics in Catalysis*, vol. 39, no. 3, pp. 167–174, Oct. 2006. [Online]. Available: https://doi.org/10.1007/s11244-006-0053-2

[77] B. Donoeva and P. E. deJongh, "Colloidal Au Catalyst Preparation: Selective Removal of Polyvinylpyrrolidone from Active Au Sites," *ChemCatChem*, vol. 10, no. 5, pp. 989–997, Mar. 2018, publisher: John Wiley & Sons, Ltd. [Online]. Available: https://chemistry-europe-onlinelibrary-wiley-com.proxy.library.uu.nl/doi/full/10.1002/cctc.201701760

[78] R.-Y. Zhong, J.-W. Yang, Z. Hu, and B.-Q. Xu, "Removal of Residual Poly(vinylpyrrolidone) from Gold Nanoparticles Immobilized on SiO2 by Ultraviolet–Ozone Treatment," *ACS Applied Nano Materials*, vol. 2, no. 9, pp. 5720–5729, Sep. 2019, publisher: American Chemical Society. [Online]. Available: https://doi.org/10.1021/acsanm.9b01197

[79] V. Dhumale, R. Gangwar, S. Datar, and R. Sharma, "Reversible Aggregation Control of Polyvinylpyrrolidone Capped Gold Nanoparticles as a Function of pH," *Materials Express*, vol. 2, pp. 311–318, Dec. 2012.

[80] R. Betancourt-Galindo, P. Reyes, B. Puente-Urbina, C. Avila-Orta, O. Rodríguez-Fernández, G. cadenas pliego, R. Lira-Saldivar, and L. García-Cerda, "Synthesis of Copper Nanoparticles by Thermal Decomposition and Their Antimicrobial Properties," *Journal of Nanomaterials*, vol. 5, Jan. 2013.

[81] H. Cannon, J., "The superlattice fomation and lattice spacing changes in copper-gold alloys." *Brigham Young Univ., Provo, UT, USA. ICDD Grant-in-Aid*, 1983.

[82] H. L. Yakel, "High-Temperature X-Ray Diffraction Study of the Order-Disorder Transition in a Cu-32.2 Atomic Percent Gold Alloy," *Journal of Applied Physics*, vol. 33, no. 8, pp. 2439–2443, Aug. 1962, publisher: American Institute of Physics. [Online]. Available: https://aip.scitation.org/doi/10.1063/1.1728989

[83] L. C.-K. Lu Hsueh-Shan, "The superlattice fomation and lattice spacing changes in copper-gold alloys." *Wuli Xuebao; Acta Phys.*, vol. 6, no. 22, p. 669, 1966.

[84] J. C. Bauer, D. Mullins, M. Li, Z. Wu, E. A. Payzant, S. H. Overbury, and S. Dai, "Synthesis of silica supported AuCu nanoparticle catalysts and the effects of pretreatment conditions for the CO oxidation reaction," *Physical Chemistry Chemical Physics*, vol. 13, no. 7, pp. 2571–2581, Feb. 2011, publisher: The Royal Society of Chemistry. [Online]. Available: https://pubs.rsc.org/en/content/articlelanding/2011/cp/c0cp01859g

[85] X. Liu, A. Wang, X. Wang, C.-Y. Mou, and T. Zhang, "Au–Cu Alloy nanoparticles confined in SBA-15 as a highly efficient catalyst for CO oxidation," *Chemical Communications*, no. 27, pp. 3187–3189, Jul. 2008, publisher: The Royal Society of Chemistry. [Online]. Available: https://pubs.rsc.org/en/content/articlelanding/2008/cc/b804362k

[86] M. Woźniak-Budych, K. Langer, B. Peplińska, Przysiecka, M. Jarek, M. Jarzebski, and S. Jurga, "Copper-gold nanoparticles: Fabrication, characteristic and application as drug carriers," *Materials Chemistry and Physics*, vol. 179, May 2016.

[87] A. Dahiya, M. Verma, and P. S. Kumar, "Plasmonic Applications of Gold-Copper Bimetallic Alloy Nanoparticles," *Plasmonics*, vol. 17, no. 5, pp. 2173–2186, Oct. 2022. [Online]. Available: https://doi.org/10.1007/s11468-022-01704-w

APPENDIX A
SUPPORTING INFORMATION

In this thesis, samples where referred to by a sample ID. This appendix provides a comprehensive description of the samples with corresponding synthesis route.

Table A.1: A list of the samples denoted with their sample ID, including a description and corresponding synthesis route

sample ID	**description**	**synthesis route**
$AuCu_xO@SiO_2$_100	core-shell Au@Cu_xO NPs coated with a mesoporous silica shell, synthesized with 100 μl Cu precursor	1
$AuCu_xO@SiO_2$_250	core-shell Au@Cu_xO NPs coated with a mesoporous silica shell, synthesized with 250 μl Cu precursor	1
$AuCu_xO@SiO_2$_1000	core-shell Au@Cu_xO NPs coated with a mesoporous silica shell, synthesized with 1000 μl Cu precursor	1
$AuCu_xO@SiO_2$_E4	core-shell Au@Cu_xO NPs coated with a mesoporous silica shell, synthesized with etched Au NPs	1
Au@Cu_2O_87	core-shell Au@Cu_2O NPs with ∼87% Cu	2
Au@Cu_2O_75	core-shell Au@Cu_2O NPs with ∼75% Cu	2
Au@Cu_2O_59	core-shell Au@Cu_2O NPs with ∼59% Cu	2
Au@Cu_2O_53	core-shell Au@Cu_2O NPs with ∼53% Cu	2
Au@aerosil	immobilized Au NPs on Aerosil OX50	3
Au@Cu_2O_1	Au@aerosil after Cu_2O overgrowth, synthesized with 1.0 ml Cu precursor	3
Au@Cu_2O_1	Au@aerosil after Cu_2O overgrowth, synthesized with 3.0 ml Cu precursor	3
Au@aerosil_BH	Au@aerosil treated with sodium borohydride	3
Au@Cu_1	Au@Cu_2O_1 after thermal treatment at 500°C in 10% H_2/N_2	3
Au@Cu_2	Au@Cu_2O_2 after thermal treatment at 500°C in 10% H_2/N_2	3
Au@Cu_2_O_2	Au@Cu_2O_1 after thermal treatment at 500°C in 10% O_2/N_2	3

APPENDIX B
SUPPLEMENTARY FIGURES

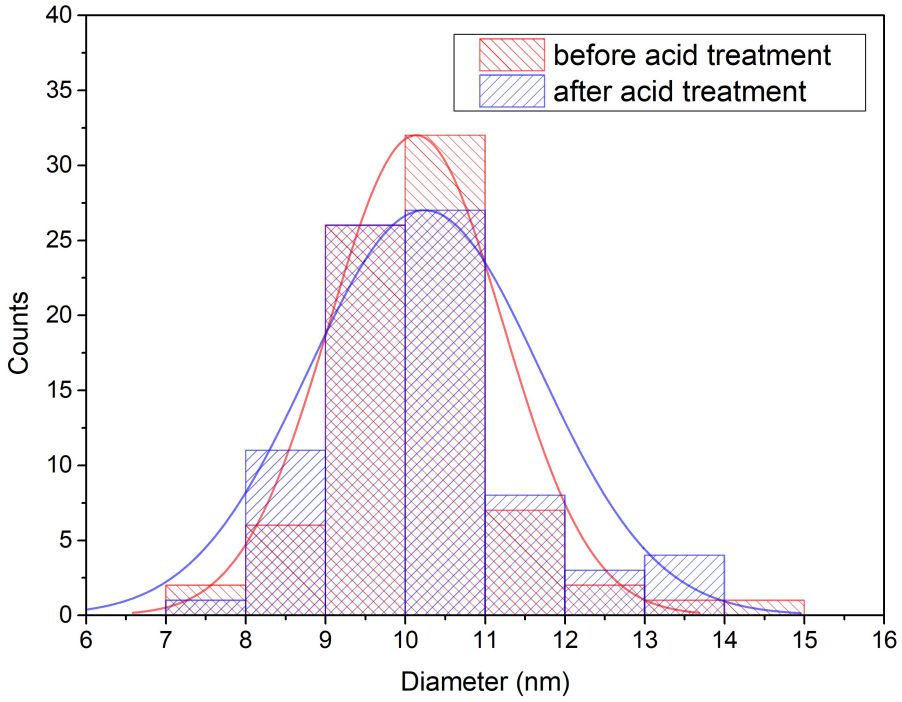

Figure B.1: The size distribution of Au NPs before (red) and after (blue) the acid treatment to remove CTAB ligands. The average particle size before and after the treatment was 10.1 ± 1.1 nm and 10.1 ± 1.3 nm, respectively.

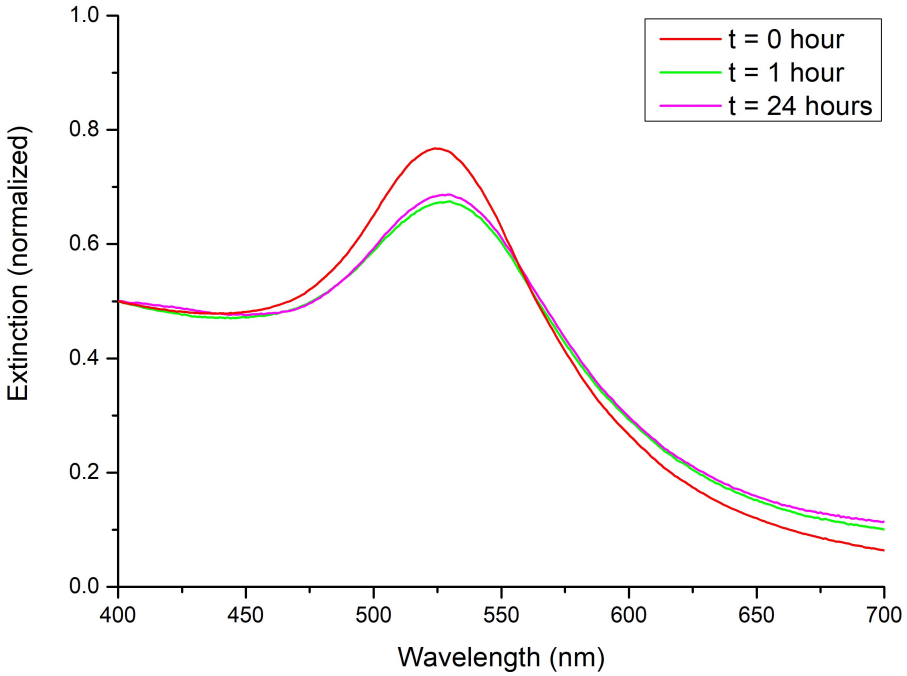

Figure B.2: The extinction spectra of $AuCu_xO@SiO_2$_250 before (t = 0), and 1h and 24h after the Cu_xO overgrowth.

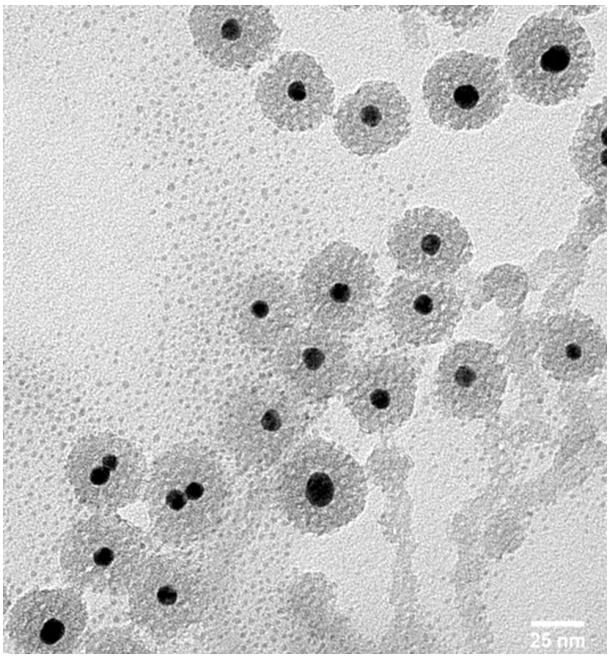

Figure B.3: A BF-TEM image of $AuCu_xO@SiO_2$_250 at t = 5 min, showing individual Cu_xO particles.

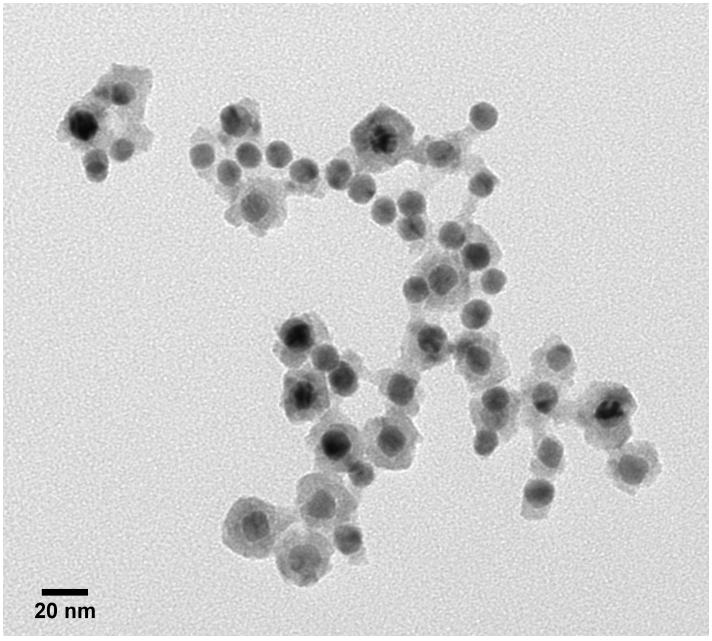

Figure B.4: A representative BF-TEM image of Au@Cu_2O NPs after the ligand exchange of PVP with CTAB.

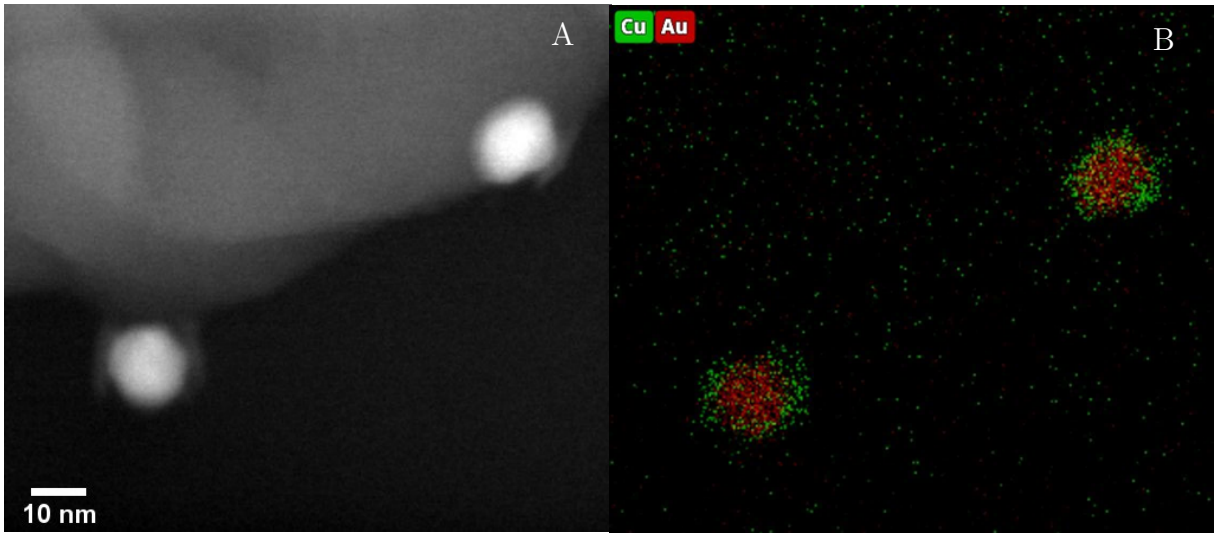

Figure B.5: a) A HAADF-STEM image with b) corresponding EDX map of sample Au@Cu_2O_1. The Cu content of the two Au@Cu_2O NPs was determined to be $38 \pm 0.3\%$ with EDX.

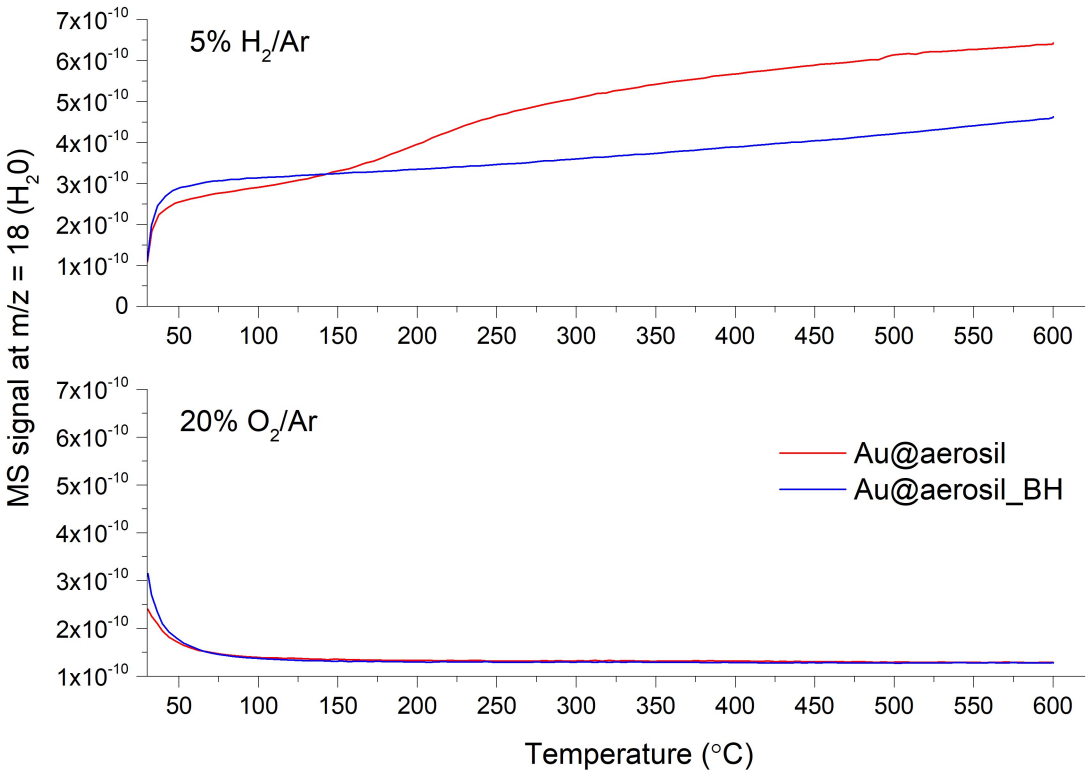

Figure B.6: Mass spectrometry (MS) data showing the intensity for H_2O (m/z = 18) of sample Au@aerosil before and after treatment with sodium borohydride (BH) in 5% H_2/Ar and 20% O_2/Ar.

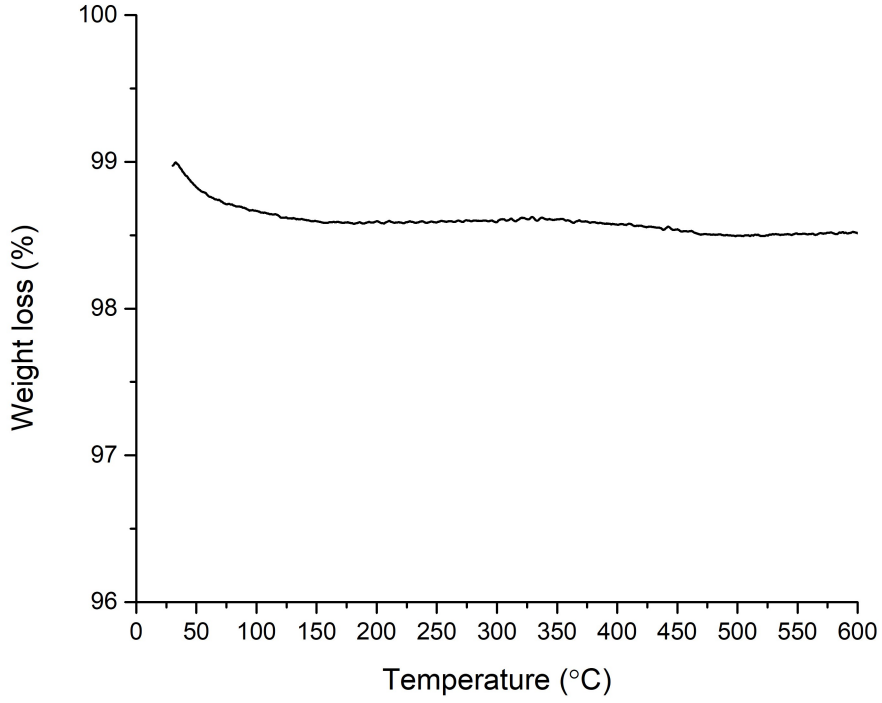

Figure B.7: TGA plot of sample Au@Cu_2O_2 after treatment in 5% H_2/Ar at 500°C (sample AuCu_2), measured in 20% O_2/Ar.

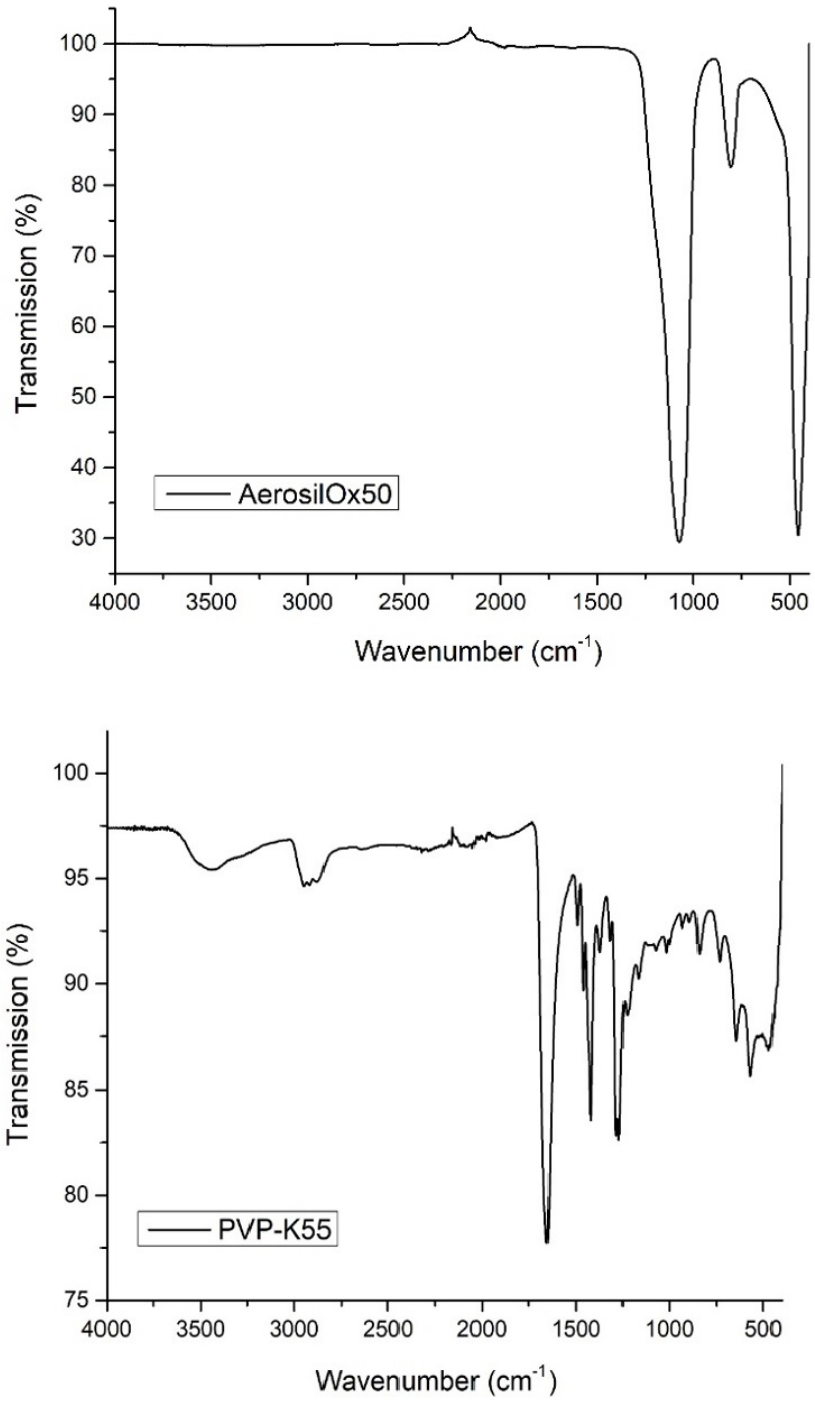

Figure B.8: FT-IR spectra of Aerosil OX50 and PVP-K55